Sivert Ragnhildstveit Erland
Elias Trondsen Dahl

Effects of H$_2$-H$_2$O Mixtures on Reducibility of Bauxite Residue - CaO Sintered Pellets

Effekten av H$_2$-H$_2$O blandinger på reduserbarheten av bauxittrester - CaO sintrede pellets

Bachelor's thesis

NTNU
Norwegian University of
Science and Technology

HARARE

Sivert Ragnhildstveit Erland
Elias Trondsen Dahl

Effects of H$_2$-H$_2$O Mixtures on Reducibility of Bauxite Residue - CaO Sintered Pellets

Effekten av H$_2$-H$_2$O blandinger på reduserbarheten av bauxittrester - CaO sintrede pellets

NTNU
Norwegian University of
Science and Technology

Effects of H$_2$-H$_2$O Mixtures on Reducibility of Bauxite Residue – CaO Sintered Pellets

Effekten av H$_2$-H$_2$O blandinger på reduserbarheten av bauxittrester – CaO sintrede pellets

Authors:

Sivert Ragnhildstveit Erland

Elias Trondsen Dahl

Supervisors:

Prof. Jafar Safarian

Dali Hariswijaya

May 2023

NTNU
Institutt for materialteknologi

HARARE

Summary of bachelor's Thesis

Contact persons: Sivert Ragnhildstveit Erland, 47522258, sivert.re@lyse.net

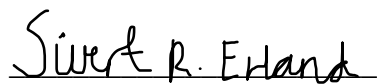Elias Trondsen Dahl, 47298902, eliasdahl142@gmail.com

Preface

This bachelor thesis investigates the effects of H_2-H_2O mixtures on the reducibility of bauxite residue – CaO sintered pellets. The research was motivated by the desire to find sustainable ways to reduce bauxite residue, which is a major environmental issue for the aluminium industry. Our thesis is written as a part of the bachelor's degree in chemical engineering at the Department of Material Sciences and Engineering (IMA) at the Norwegian University of Science and Technology (NTNU). In particular, we would like to thank the individuals and organizations who gave us the problem to solve and helped throughout the research process.

Firstly, we would like to express our gratitude to our supervisors, prof. Jafar Safarian and PhD cand. Dali Hariswijaya, for their invaluable guidance and support throughout this project. Their expertise in designing our experiments, interpreting our results and their proficiency in the field of metallurgy and materials science.

Secondly, we would like to thank SINTEF for letting us use their equipment, and Jonas Einan Gjøvik, for helping us set up and fix all the necessary apparatuses to be able to complete our experimental work. Also, we would like to thank Dmitry Slizovskiy from NTNU for providing us with necessary gas and gas detectors needed to run the experiments. We would also like to thank Ina Merete Stuen for her guidance throughout our entire degree.

Finally, we would like to thank the HARARE EU project for funding our research work, and providing us with a challenging, though exciting project.

We hope this thesis helps to contribute to the ongoing HARARE EU project to reduce bauxite residue and promote sustainability in the aluminium industry. We welcome feedback on our findings, and we hope that our research will inspire further investigation in this field.

Sivert Ragnhildstveit Erland   Elias Trondsen Dahl

Trondheim 19th May 2023

Abstract

Having the ability to develop and minimize the production of red mud from the aluminium industry is desirable, since it represents a huge environmental problem today. High alkalinity and the fine particle size distribution are some of the reasons for its environmental hostility. The industrial waste does also lead to loss of iron- and aluminium units in the bauxite residue.

In this thesis, the bauxite residue (BR) was pelletised and sintered at 1150°C under atmospheric pressure. These pellets were then analysed and characterised through several analytical methods, such as X-Ray diffraction (XRD), X-Ray fluorescence (XRF), scanning electron microscopy (SEM) supported by energy-disperse spectroscopy (EDS), Brauner-Emmet-Teller (BET) and Barett-Joyner-Halende (BJH). This analytical practice was also done later to characterise reduced pellets. To be able to reduce the sintered pellets, hydrogen was introduced in a reduction furnace, a vertical tube furnace at 600°C and 800°C. The reduction experiments used different H_2-H_2O mixtures, where the humidities used was 0%, 5%, 15% and 25%.

The SEM analyses yielded that at higher temperature coupled with reduced humidity levels led to more production of metallic iron. It was possible to see which phases were present through XRD. For example, brownmillerite was present in the sintered pellets, but not after the reduction. Furthermore, gehlenite was present in all the samples. BET and BJH resulted in that by reducing the pellets with pure hydrogen gave the largest surface area and pore size. But, by increasing the temperature, the pores shrunk.

The primary outcome of this thesis is to investigate equilibrium conditions of H_2 reductions of iron oxides in BR. It was found that at higher levels of humidity, the reduction of iron oxides stops because of thermodynamic conditions. This is especially seen at 800°C with 25% humidity, where no metallic iron was formed. At lower temperatures, humidity greatly inhibits reduction, as the reduction degree for 0% humidity was 49,64%, almost twice as high compared to 5% humidity which yielded 25,56%.

Sammendrag

Det er et sterkt ønske å minimere produksjonen av rødslam fra aluminiumindustrien, da det står for et stort miljøproblem i dag. Det høye alkalitetsnivået og fordelingen av fine partikkelstørrelser er hovedårsakene til at rødslam er så destruktivt for naturen. Industriavfallet fører også til tap av jern og aluminium i bauxittresten. Det er derfor av stor betydning å utforske metoder for å redusere mengde rødslam produsert og redusere miljøbelastningen fra aluminiumsindustrien.

I dette studiet ble bauxittrester (BR) pelletert og sintret på 1150°C under atmosfærisk trykk. Disse pelletene ble deretter analysert og karakterisert gjennom flere analytiske metoder, som X-Ray diffraction (XRD), X-Ray fluorescence (XRF), scanning electron microscopy (SEM), energy disperse spectroscopy (EDS), Brauner-Emmet-Teller (BET) and Barett-Joyner-Halende (BJH). Disse analytiske metodene ble etterfølgende anvendt på de reduserte pelletene. For å redusere de sintrede pelletene ble hydrogen introdusert i en vertikal reduksjonsovn, ved temperaturer på henholdsvis 600°C og 800°C. Reduksjonseksperimentene brukte forskjellige H_2-H_2O blandinger, hvor fuktighetene som ble tatt i bruk var på 0%, 5%, 15% og 25%.

Resultatene av SEM analysen ga en indikasjon på at økende temperatur og redusert fuktighetsnivå ga økt produksjon av metallisk jern. Det var mulig å se hvilke faser som var til stede gjennom XRD. Et eksempel på dette er observert i de sintrede prøvene, der brownmillerite var til stede, mens det ble ikke påvist i de reduserte prøvene. I tillegg var gehlenite påvist i alle prøvene. Resultatene fra BET og BJH analysene viste at reduksjon av pelletene med ren hydrogengass førte til størst overflateareal og porestørrelse. Imidlertid førte økning i temperatur til mindre porestørrelse.

Denne oppgaven skal undersøke likevektsbetingelsene for H_2-reduksjoner av jernoksider i BR. Det ble funnet at termodynamiske forhold vil hindre reduksjonen av jernoksider ved høye fuktighetsnivåer. Dette kan spesielt sees ved 800°C med 25% fuktighet, da ingen metallisk jern ble dannet. Ved lavere temperaturer vil fuktigheten i stor grad inhibere reduksjon, da reduksjonsgraden for 0% fuktighet var 49,64%. Dette er nesten dobbelt så høyt sammenlignet med et fuktighetsnivå på 5% som ga en reduksjongrad på 25,56%.

Table of contents

List of Figures

List of Tables

Abbreviations

at% - atom percentage

BEI – Backscattering electron imaging

BET – Brunauer-Emmet-Teller

BJH - Barrett-Joyner-Halenda

BR – Bauxite residue

BSE – Back-scattered electrons

EDS – Energy-dispersive X-Ray spectroscopy

REEs – Rare earth elements

SEI – Secondary electron imaging

SEM – Scanning electron microscope

VDW - Van der Waals

wt% - weight percentage

XRD – X-Ray powder diffraction

XRF – X-Ray fluorescence

1. Introduction

In this chapter, background and the motivation are presented, as well as the main objective for this thesis.

1.1 Background

The generation of bauxite residue (BR) from the Bayer process is a worldwide problem that poses a big threat to the environment. As there are no industrial processes that utilises BR to its full extent, the waste is stored in large pools and, if not treated properly, can cause major problems to its surroundings due to the high alkalinity of the waste. Since BR contains important elements, such as Fe, Al and Ti, and rare earth elements (REEs), such as cerium, the valorisation of BR is highly interesting to achieve, and much research have been done to utilise the BR. By now, no industrial processes take use of BR, mainly because of economic obstacles [1]. This causes valorisation of BR to be challenging even to this day. Since the demand for aluminium products increases around the world, the generation of BR also increases. Typically, depending on the quality of the bauxite ore, the generation of BR is between 55-65% of the bauxite processed [2]. The utilisation of BR today is mainly as additives in cement, around 3 million tons per year, which only accounts for less than 1% of BR which is present worldwide [3]. Because of the high levels of Fe and other elements, the valorisation of BR can create huge amounts of profits. BR can also be an excellent livestock for Fe and other materials if it is valorised properly [3]. During 1927, Harald Pedersen proposed a different method to extract alumina from bauxite ore. This method differs from the Bayer process in the form of no BR generation, and therefore it is a more sustainable method for extracting alumina from bauxite ore. This method was applied in Høyanger, Norway from 1927 to 1969, before being discontinued because of economic reasons [4].

1.2 Motivation

In New Innovation Action EU project, HARARE, hydrogen-use to valorise BR is studied. In a Ca-route of the HARARE project, BR is agglomerated with lime and then reduced by hydrogen. The produced Fe in the reduced agglomerate is then separated by magnetic separation, while the nonmagnetic portion is treated to extract alumina and REEs. This bachelor's thesis in HARARE focuses on the effects of adding H_2O-gas to the H_2-gas during reduction, and how the presence of

H_2O-gas will affect the reduction rate. Initially, presence of specific levels of H_2O-gas is believed to inhibit the reduction of the BR pellets. This is based on how different compositions of water vapour affects the reduction rate, as opposed to pure H_2-gas. Even at a gas composition with small amounts of water vapour can greatly affect reduction rate [5]. While in an industrial setting, reduction with gas consisting of water vapour is favourable, because of safety concerns.

1.3 Objectives

In this thesis the main objectives are:

- To test on laboratory scale how small to great amounts of water vapour in H_2 gas will affect the reducibility of BR-pellets.
- To compare the reducibility of complex Fe-containing oxides in the BR agglomerate with literature data and outline the proper H_2-H_2O mixtures for different temperatures.
- To see whether this yields enough metal to be applied to industrial levels of metal recovery.
- To study the effect of gas composition and temperature in hydrogen reduction on the microstructure, mineralogical and physical properties of the BR-CaO pellets are evaluated.

2. Theory

The Bayer process to produce alumina, BR problem and valorisation are described in this chapter. Moreover, the theories related to the hydrogen reduction of BR-CaO agglomerates are studied, including thermodynamics and kinetics.

2.1 Bayer process

The Bayer process is the main commercially used method for extracting alumina (Al_2O_3) from bauxite ore. The process was invented and patented by Carl Josef Bayer in 1888 and has since then been the leading process for alumina production in the world. The process consists of eight main stages: Milling, desilication, digestion, clarification, precipitation, evaporation, classification and calcination [6][7].

In the milling step, the bauxite ore is crushed down into finer particles. This makes it so that the available surface area is increased for the digestion stage of the process. Additionally, limestone is added to create a pumpable slurry [6][7].

After the milling step, the slurry moves through a process called desilication, which involves removing silica (SiO_2). The slurry is then digested using a NaOH solution, which dissolves the aluminium bearing minerals in the bauxite. These minerals include gibbsite ($Al(OH)_3$, boehmite (γ-AlO(OH)) and diaspore (α-AlO(OH)). When the solution is added, the following reactions happens for gibbsite and boehmite/diaspore, given by Equation 1 and 2 respectively [6][7].

$$Al(OH)_{3(s)} + NaOH_{(aq)} \rightarrow Al(OH)^-_{4(aq)} + Na^+_{(aq)} \tag{1}$$

$$AlO(OH)_{(s)} + NaOH_{(aq)} + H_2O_{(l)} \rightarrow Al(OH)^-_{4(aq)} + Na^+_{(aq)} \tag{2}$$
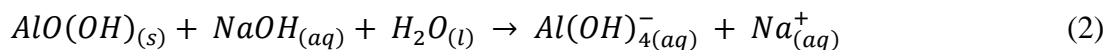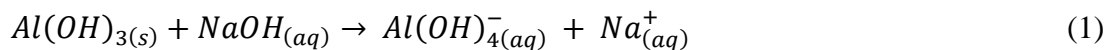
During digestion, different conditions such as temperature, caustic concentration and pressure are needed to process the ores due to differences in properties. For ores with a high concentration of gibbsite, the temperature needed for processing are no more than 140°C. For ores with a high concentration of boehmite and diaspore, the temperature needed for processing are between 200°C

to 280°C. After the processing step, the slurry is cooled down using a series of flash tanks at 1 atm [6][7].

Subsequent to the digestion process, the resulting slurry is prepared for clarification where the BR is extracted and separated away. This is achieved through sedimentation, where chemical additives assist in driving the BR to the bottom of the settling tanks. BR is transferred to washing tanks, where the goal is to recover the caustic soda used in the digestion step, for reusing purposes. The saturated liquid undergoes a series of filtration steps, to ensure that the final product is free from contaminants. BR is left in disposal areas [6][7].

After clarification, alumina is recovered through crystallisation during the precipitation step. Here, the slurry is cooled down to form aluminium trihydroxide crystals ($Al(OH)_3$). The reaction is shown in Equation 3 [6][7].

$$Al(OH)_{4(aq)}^{-} + Na_{(aq)}^{+} \rightarrow Al(OH)_{3(s)} + NaOH_{(aq)} \tag{3}$$
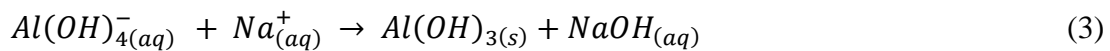
Evaporation of the liquid used during crystallisation takes place in heat exchangers, where it is subsequently cooled afterwards in flash tanks. The condensate that is created through this process is re-used for BR washing or as feed water. Recovered caustic soda is then re-added to the digestion step [6][7].

The crystals are classified into size ranges, using cyclones and gravity classification tanks. For the coarse crystals, separation from liquid and calcination is performed. For the finer crystals, washing to remove organic impurities and re-addition to the precipitation step is performed [6][7].

Calcination of the coarse crystals is done by roasting in calciners. The roasting process takes place at temperatures up to 1100°C. This drives off moisture and water, which eventually creates alumina solids. The calcination reaction is shown in Equation 4 [6][7].

$$2Al(OH)_{3(s)} \rightarrow Al_2O_{3(s)} + 3H_2O_{(g)} \tag{4}$$

The flowsheet of the Bayer process is illustrated in Figure 1.
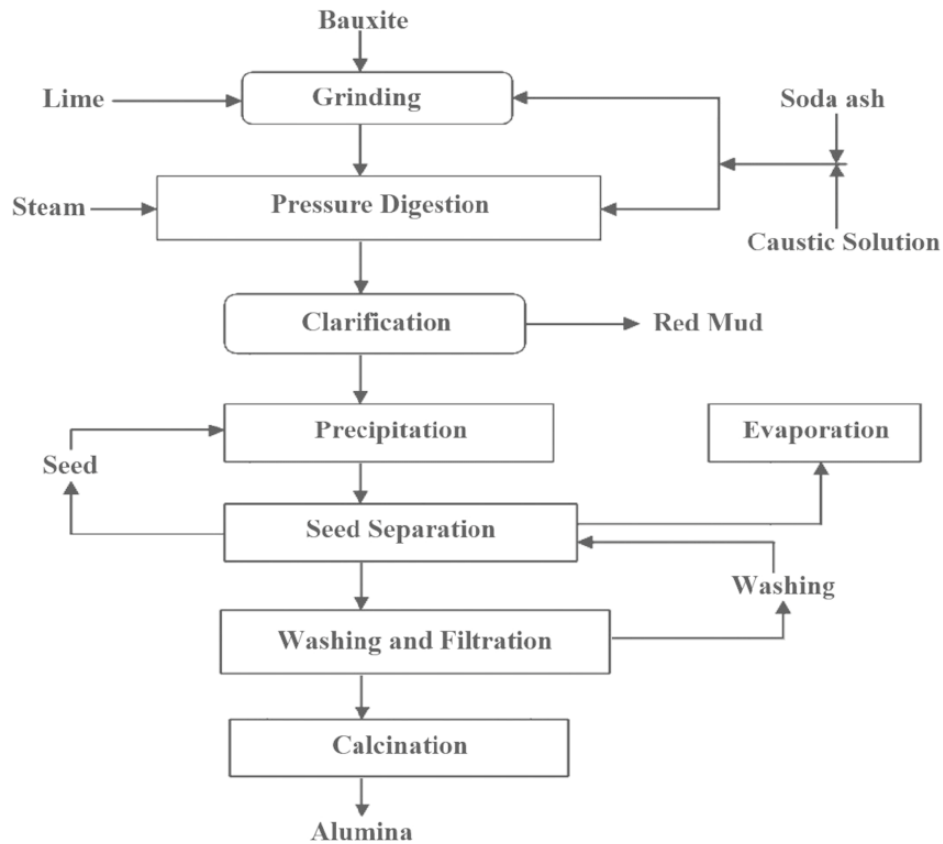
Figure 1: Flowsheet of the Bayer process [8].

2.2 Red mud

Red mud, also known as bauxite residue (BR), is the main by-product generated in the Bayer process. Typically, for each ton of produced alumina from bauxite ore, about 1,5 tons of BR is produced [9]. The generated BR from the Bayer process is stored in large holding ponds, where only 1-2% undergoes recycling [10].

BR is characterised by the presence of iron oxides, which can constitute as much as 50% of its overall composition. In addition, other compounds found in BR includes silica oxides, titanium oxides, aluminium oxides and other oxides. It is also highly alkaline, with a pH level ranging from 12-13 [10]. Due to its high alkalinity, the BR that is stored away in holding ponds poses a great environmental threat to its surroundings. The main way of treating the alkaline BR, is to attempt neutralizing by adding acidic substances such as HCl [10].

Table 1 shows an overview of the main compounds found in BR. The compound that is most present is hematite (Fe_2O_3). This is what gives BR its characteristic red colour. Other compounds that are not present in the table includes goethite ($Fe_{(1-x)}Al_xOOH$), gibbsite ($Al(OH)_3$), boehmite (γ-$AlO(OH)$), diaspore (α-$AlO(OH)$), calcite ($CaCO_3$) and more [11].

Table 1: Typical composition of BR measured by XRF [11].

Composition	Wt%
Fe_2O_3	30-60
Al_2O_3	10-20
SiO_2	3-50
Na_2O	2-10
CaO	2-8
TiO_2	Trace-25

In 2010, an accident related to BR-spillage occurred in Hungary. The accident photo is presented in Figure 2. A BR reservoir connected to the alumina plant in Ajka collapsed, and about $700\,000m^3$ of BR was released into the valley of the Torna River, resulting in flooding of the city Devecser, and the small towns Kolontár and Somlóvásárhely. The flood led to disastrous consequences, killing 10 people and injuring hundreds. Additionally, the flood had huge environmental consequences, resulting in the destruction of agricultural fields in the area [12][13]. Luckily, the long-term effects of the spill turned out to be less severe than first anticipated, with traces of BR in the related areas being almost non-existent today [14].

Figure 2: Aerial view of the broken dyke near Ajka, Hungary [14].

2.3 BR valorisation, importance, and methods

Since BR poses such a big environmental problem, and because of its iron and aluminium rich content, the valorisation of this by-product is therefore quite important to achieve a sustainable and green industry in the future.

2.3.1 BR direct use

Today, BR has been utilised for many purposes, such as construction, additives in cement and other building materials and lightweight aggregates. In cement industries, BR is used as a binder, additive, clay material and as a colouring agent in paint and pigment. It has also been utilised much in ceramics, where BR can be used to make ceramic tiles and ceramic coatings. Some research has also shown promising results when using BR as a filler and reinforcement in polymer and metal matrix composites [15]. These are just some examples of what BR can be used for. Figure 3 shows a flow chart of all the different areas of uses for BR.
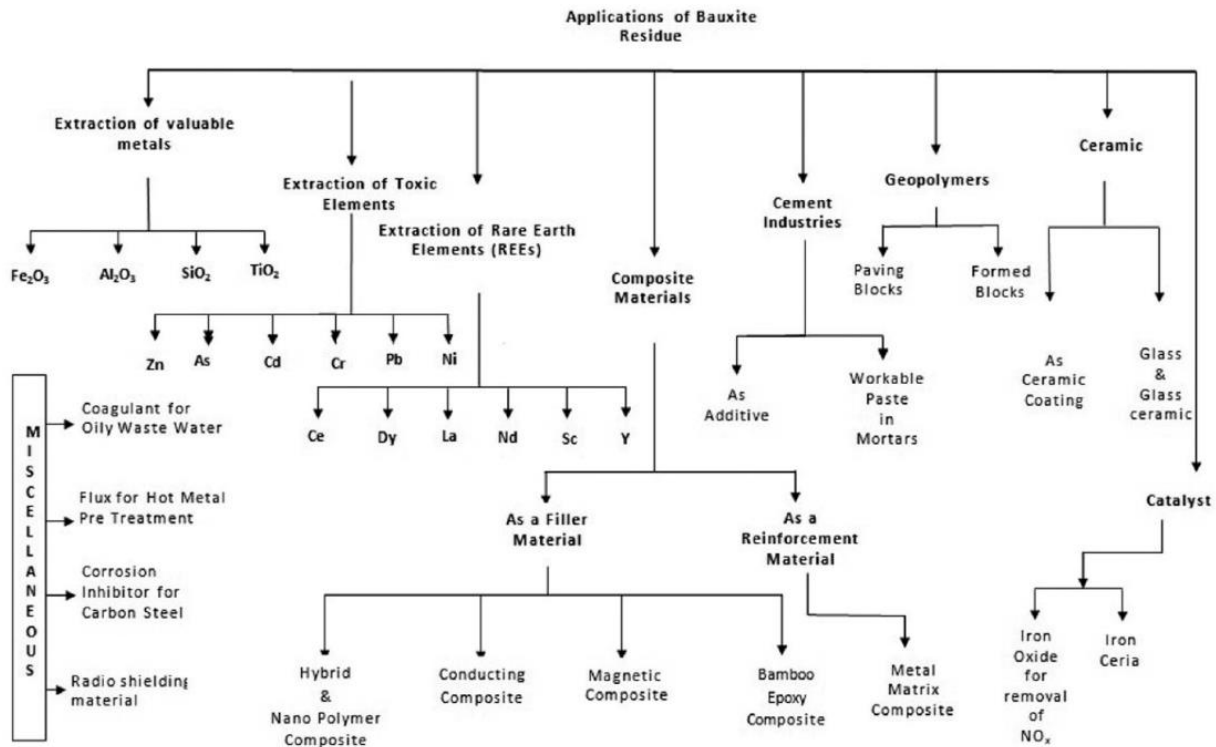
Figure 3: Flow chart about the uses of BR [15].

2.3.2 Material recovery from BR

As seen from Table 1 and Chapter 2.2, BR contains many valuable metals such as iron, aluminium, and titanium, in addition to silicon. Therefore, it is highly interesting to utilise and extract these metals from BR. Over the years, much research has been conducted on the methods for achieving the efficient extraction of valuable metals from BR, including both metallurgical and non-metallurgical methods. One method for iron-extraction from BR is by roasting it in a muffle-furnace, followed by magnetic separation, which separates the metallic compounds (such as iron) from the non-metallic compounds. A previous experiment showed that this gave a 50,5% iron-rich concentrate, which in turn resulted in an iron recovery at 70% [16].

Leaching represents an alternative method for metal recovery from BR. In this method, the BR is leached with oxalic acid before being roasted in a muffle furnace. Before being roasted, a leachate of Fe^{3+} and Al^{3+} ions are separated from the rest of the oxalic acid residue. After roasting, the residue is further leached with hydrochloric acid, to give a leachate of Ca^{2+} ions that is separated

out. Finally, the residue is leached with sulfuric acid, giving a leachate of rare earth elements (REEs), such as scandium, cerium and lanthanum [17].

Efforts has been made to create a zero-waste process for alumina production. The ENSUREAL project is one of these efforts, where the goal was to introduce a new technology which would enhance the alumina yield from the process. As detailed in Chapter 1.1, the Pedersen process was the focal point for ENSUREAL, with the project aiming to improve and modernize this approach. This was due to its potential to significantly reduce waste products, in contrast to the Bayer process. Although the Pedersen process is more economically demanding, the consensus is that increased costs of processing will be balanced with an increase of revenue that the different products give. Furthermore, ENSUREAL proposed a value chain that considered all the processing streams as valorisable products. Currently, the project has ended, but the primary outcome indicated that the amalgamation of the Bayer and Pedersen processes exhibits the greatest potential. Figure 4 shows an industrial process concept from the ENSUREAL project, given in the project's final presentation in 2022 [18].
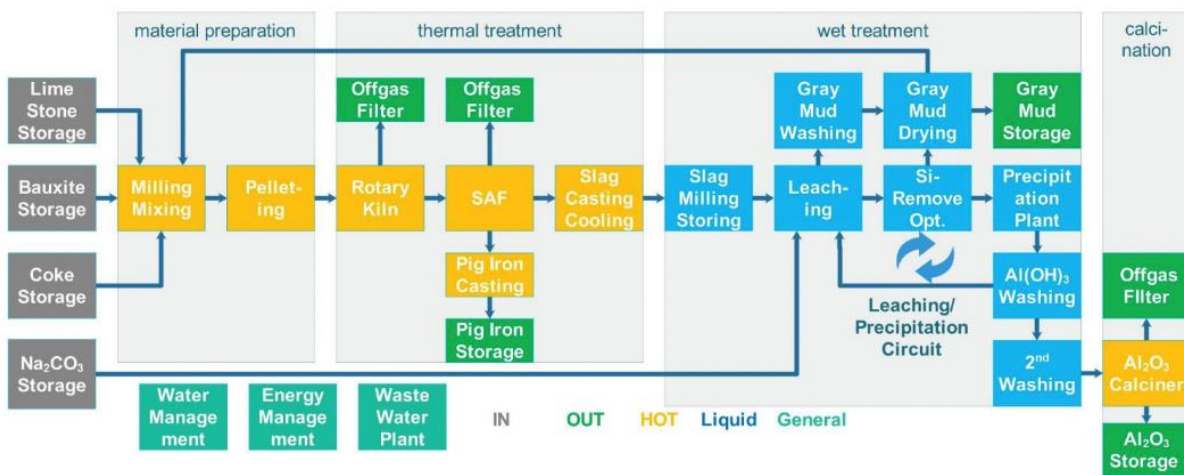
Figure 4: Flow sheet of the proposed process from the ENSUREAL project [18].

The HARARE project aims to valorise BR with the use of hydrogen. In an EU report in 2017, the metallurgical industry stood for 70 million tons of CO_2-emissions annually. Furthermore, importing of materials is another issue related to emissions. By substituting carbon with hydrogen, the industry can potentially become emissions-free. Moreover, the HARARE project aims to

utilise raw materials more efficiently, as this will reduce Europe's dependence on critical raw materials. The HARARE project has a big focus on valorisation of BR, as this is a critical environmental problem because of its highly alkaline properties. By investigating the use of hydrogen to reduce oxides in BR, several problems related to sustainability and environmental issues can be solved, as well as better utilisation and treatment of waste [10][19].

2.4 Sintering

Sintering is a process where powder, or in this case pellets, is herded into more robust material. This occurs when the material in question is substantially heated up, while being maintained below its melting point. Sintering is a pivotal part of the experimental phase, mainly because it reduces the material's ability to resist gas flow, which means that the gaseous H_2-H_2O mixture can more easily travel through the various layer that the samples may contain. It is also convenient for transportation and handling, due to the samples becoming more robust and less likely to fall apart [20].

During sintering of BR-CaO pellets, hematite transforms into brownmillerite ($Ca_2(Al,Fe)_2O_5$). Additionally, complexes such as srebrodolskite ($Ca_2Fe_2O_5$), fayalite (Fe_2SiO_4) and gehlenite ($Al_2Ca_2O_7Si$) forms, thus the weight percentages of oxides increase. Figure 5 shows a normalised XRD-plot, which highlights the aforementioned phases in sintered BR-CaO pellets performed in a previous experiment [21]. Chapter 2.7.3 describes more about the analytical method XRD.
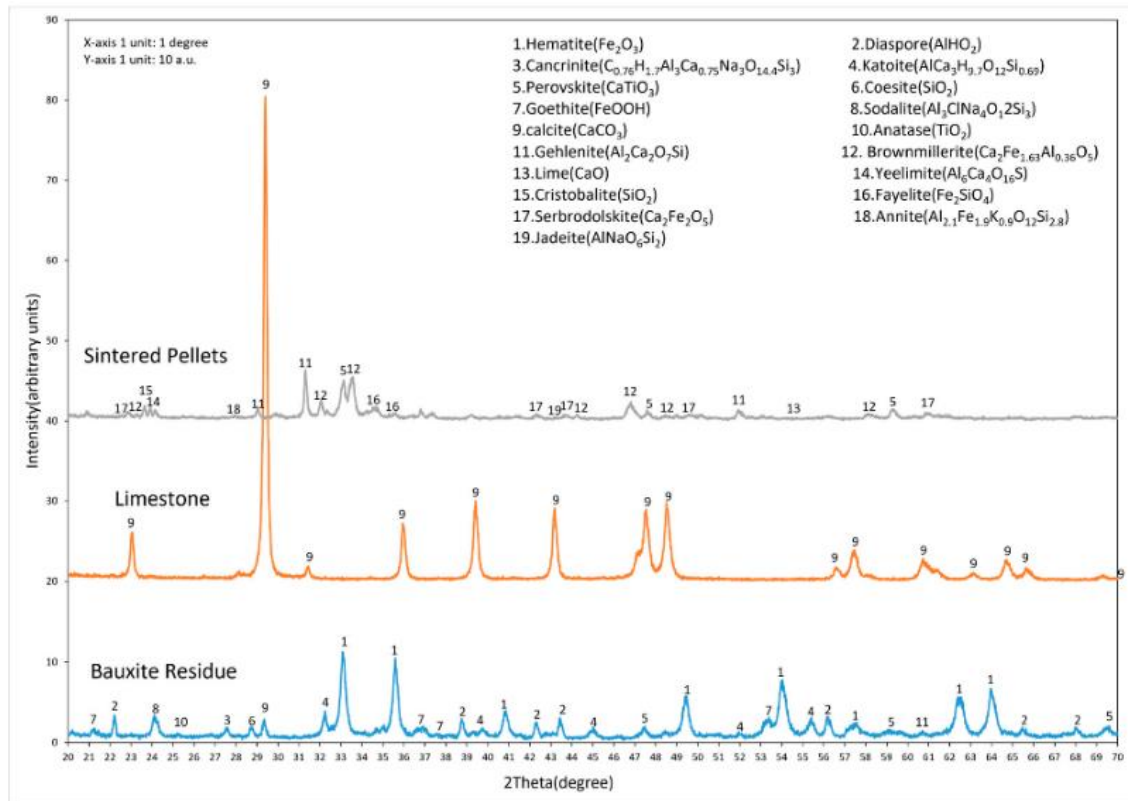
Figure 5: XRD-plot of sintered BR-CaO pellets, in addition to raw BR and limestone [22].

2.5 Thermodynamics and kinetics of iron oxides reduction

To investigate the thermodynamics of iron oxides reduction, Gibbs free energy and the Ellingham diagram must be investigated. Furthermore, for kinetics, the dependence of H_2-H_2O mixtures is important.

2.5.1 Gibbs free energy

Gibbs free energy is a state function that describes the maximum amount of work done by a thermodynamic system during constant temperature and pressure. Gibbs energy is a rearrangement of the second law of thermodynamics and provides information about the spontaneity of a chemical reaction [23]. The general expression for Gibbs free energy is shown in Equation 5.

$$G = H - TS \tag{5}$$

Where G is Gibbs free energy (typically in kJ/mol), H is enthalpy (typically in kJ/mol), T is absolute temperature (K) and S is entropy (typically in J/mol*K).

Generally, to study the spontaneity of a chemical reaction at equilibrium, the following expression is used, shown in Equation 6:

$$\Delta G = -RT \ln K \tag{6}$$

Where R is the universal gas constant (8,314 J/K*mol) and K is the equilibrium constant [23].

The symbol ΔG denotes the change in Gibbs energy for a given chemical reaction. A negative value for ΔG means that the reaction occurs spontaneously, while a positive value indicates a non-spontaneous reaction. The spontaneity of a reaction is also dependent on enthalpy, as well as entropy. This is based on Equation 5, as shown above. Table 2 gives an overview of how these factors affect Gibbs free energy [23].

Table 2: Overview of factors affecting Gibbs free energy.

	$\Delta H < 0$	$\Delta H > 0$
$\Delta S > 0$	$\Delta G < 0$, spontaneous	Only spontaneous at high T
$\Delta S < 0$	Only spontaneous at low T	$\Delta G > 0$, non-spontaneous

The effects of water vapour on the reduction rate, with the use of H_2, is to be studied in this thesis. Therefore, to calculate the Gibbs free energy of the different reduction experiments and understanding how water vapour affects spontaneity, Equation 6 can be rewritten as follows, shown in Equation 7.

$$\Delta G = \Delta G^0 + RT \ln \left(\frac{H_2O}{H_2} \right) \tag{7}$$

Where ΔG^0 denotes standard Gibbs free energy for a given reaction at 25°C and 1 atm.

Due to the dependency of Gibbs free energy on enthalpy, Tables 3 and 4 present a comprehensive summary of the reaction enthalpies and Gibbs free energy for hematite at the temperatures corresponding to those utilized in the experiments. Thermodynamic data is calculated from HSC Chemistry, with pure H_2-gas serving as the basis for these computations.

Table 3: Thermodynamic data at 600°C.

Reaction	ΔH [kJ]	ΔG [kJ]
$3Fe_2O_{3(s)} + H_{2(g)} \rightarrow 2Fe_3O_{4(s)} + H_2O_{(g)}$	11,922	-76,571
$Fe_3O_{4(s)} + 4H_{2(g)} \rightarrow 3Fe_{(s)} + 4H_2O_{(g)}$	99,173	28,676
$Fe_3O_{4(s)} + H_{2(g)} \rightarrow 3FeO_{(s)} + H_2O_{(g)}$	55,245	6,516
$FeO_{(s)} + H_{2(g)} \rightarrow Fe_{(s)} + H_2O_{(g)}$	14,643	7,387

Table 4: Thermodynamic data at 800°C.

Reaction	ΔH [kJ]	ΔG [kJ]
$3Fe_2O_{3(s)} + H_{2(g)} \rightarrow 2Fe_3O_{4(s)} + H_2O_{(g)}$	4,341	-95,730
$Fe_3O_{4(s)} + 4H_{2(g)} \rightarrow 3Fe_{(s)} + 4H_2O_{(g)}$	95,527	13,170
$Fe_3O_{4(s)} + H_{2(g)} \rightarrow 3FeO_{(s)} + H_2O_{(g)}$	50,473	-4,018
$FeO_{(s)} + H_{2(g)} \rightarrow Fe_{(s)} + H_2O_{(g)}$	15,018	5,730

From Tables 3 and 4, formation of magnetite from hematite occurs spontaneously under all temperatures due to negative Gibbs energy. Due to positive change in enthalpy, all the reactions are endothermic, thus needing energy to initiate.

2.5.2 Reduction using H_2-H_2O gas

Described by the Baur-Glassner diagram shown in Figure 6, H_2-H_2O gas behaves as a reducing agent. The diagram shows how the Fe-O-H system behaves under the presence of water vapour [24].
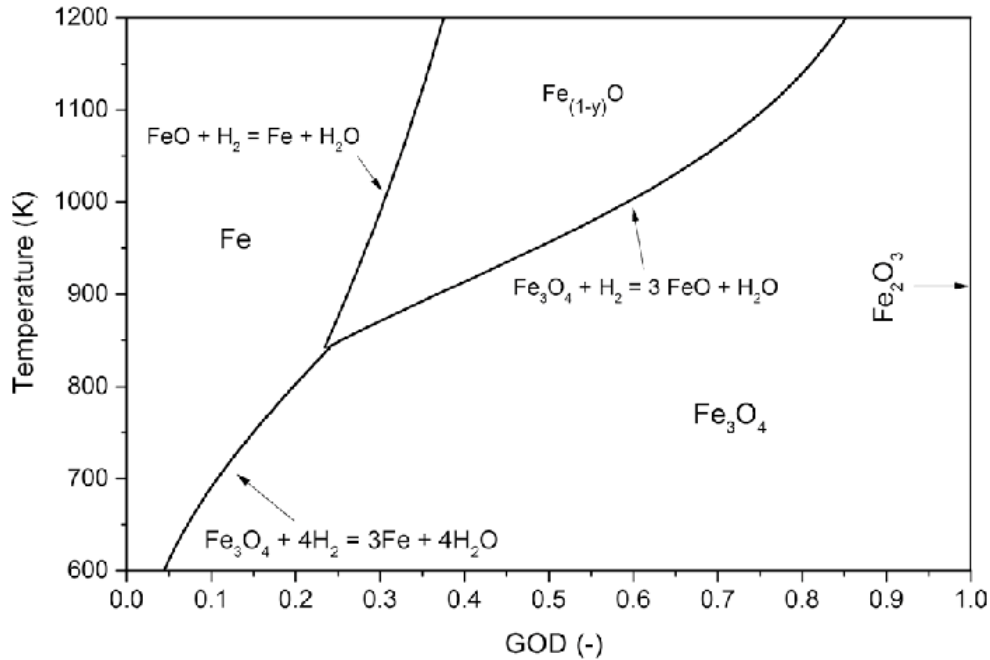
Figure 6: Baur-Glassner diagram, with coherent stability range [24].

The Baur-Glassner diagram shows how temperature, and the GOD (gas oxidation degree) relates to the stability of different phases present. GOD is defined as the ratio between oxidised and oxidisable components in the reducing gas, which is H_2O/H_2 ratio when H_2-H_2O mixtures are used [24]. Stability of both metallic iron and wüstite increases with increasing temperature, meaning that from a thermodynamic point of view, the temperature needs to be as high as possible to achieve a greater yield of reduction [25]. It is therefore important to maintain a high enough temperature over a given amount of time, meaning the reduction process needs to happen isothermally. Pre-heating with argon, and then switching to H_2-gas when the desired temperature is reached is a method to achieve isothermal conditions. A schematic of this procedure is shown in Figure 7.

When H_2-gas is humidified by H_2O-vapour, the H_2-H_2O gas composition can affect the reaction in several ways: According to the Baur-Glassner diagram, the stability of different oxides increases

if more H_2O-vapour is present. On the other hand, excess water molecules may adsorb at the reaction interface, blocking free reaction sites where H_2-gas can initiate a reaction [25].
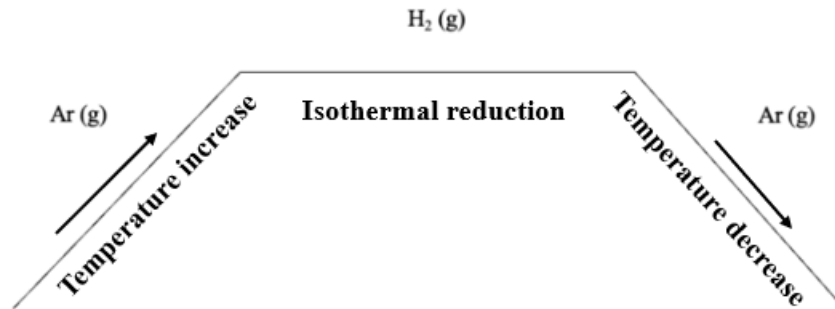
Figure 7: Heating, reduction, and cooling schematic.

Furthermore, magnetite can form wüstite instead of metallic iron, where formation of wüstite from magnetite occurs spontaneous at a temperature of 800°C, as seen from Table 4. In the temperature range spanning 570°C and 1400°C, the direct formation of wüstite from magnetite prevails over the formation of metallic iron, as wüstite exhibits greater thermodynamic stability in this range. Additionally, the oxygen-levels that is required to form wüstite is between 23% and 25,4%. To avoid this and to form metallic iron directly, the oxygen-level must be below 23% [34]. This is seen in Figure 8, which shows a binary Fe-O diagram explaining how and when different iron and iron-oxides stability areas are formed, and its relation to temperature and oxygen-level.
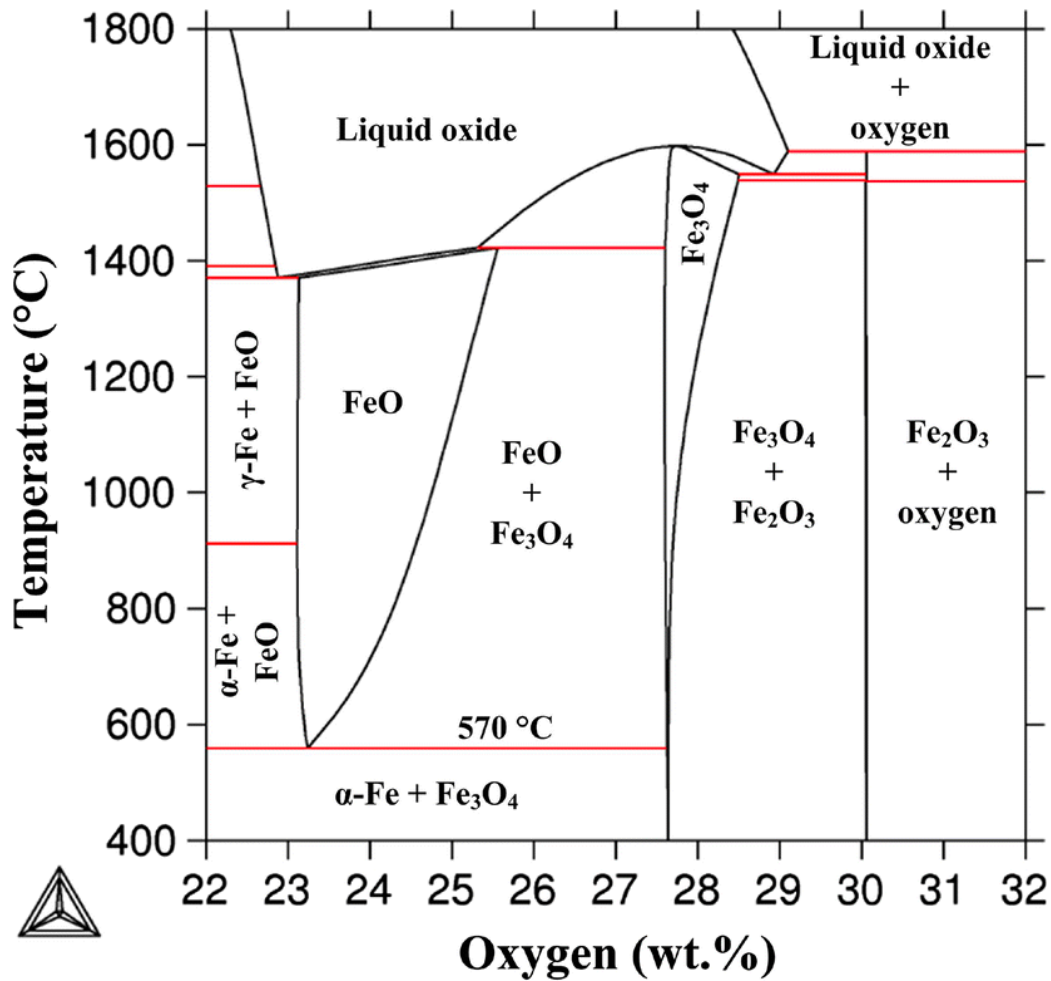
Figure 8: Binary Fe-O system, and its relation to temperature and oxygen levels [27].

2.5.3 Ellingham diagram

The Ellingham diagram is a plot of Gibbs free energy (ΔG) versus temperature (T). This graphically illustrates the thermodynamic stability of a metal oxides at varying temperatures [28]. The plot, seen in Figure 10, displays a series of straight lines where the change of entropy (ΔS) is the slope and change in enthalpy (ΔH) is where the line intercepts with the y-axis. If an intersection between two lines is present, it means that the two metal oxides are at thermodynamic equilibrium. Standard formula for the plots can be seen in Equation 8, where xM is a metal and M_xO_2 is the metal oxide. A necking on the line may occur if one of the elements changes phases, I.e., evaporates or melts [28].

$$xM_{(s)} + O_{2(g)} \rightarrow M_xO_{2(s)} \tag{8}$$

Ellingham diagrams is used to predict the stability of metal oxides in different temperatures and partial pressures of oxygen, carbon monoxide-to-carbon dioxide ratio or hydrogen-to-water ratio, which is the case for this study. It can also see the feasibility of reactions involving metal oxides and other substances, such as carbon and hydrogen [29].
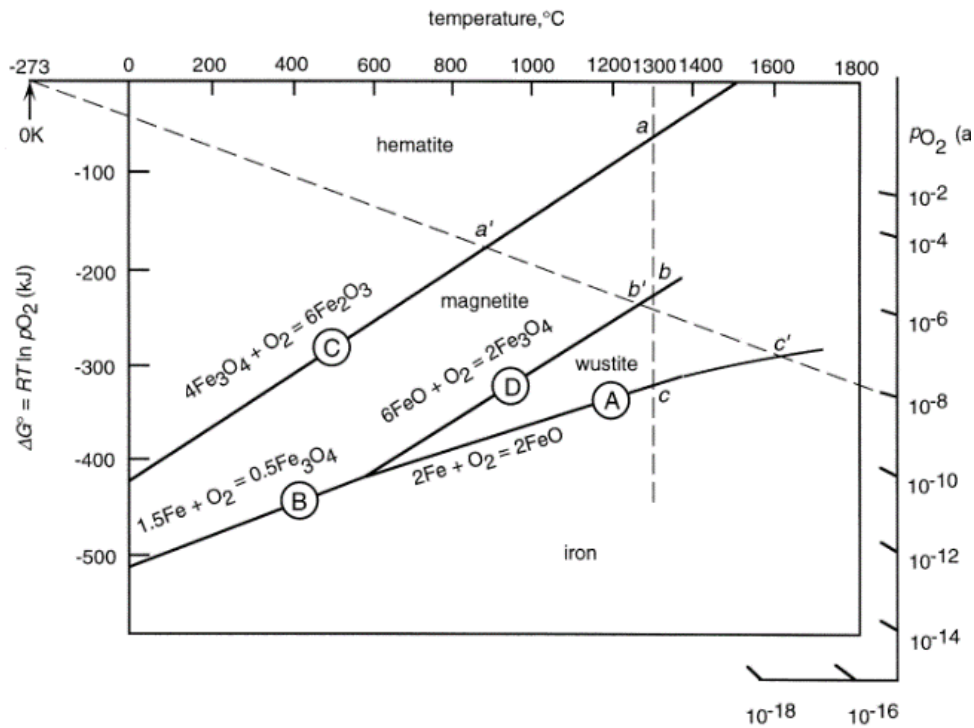
Figure 9: Ellingham diagram for Fe-FeO in different states [22].

This current study investigates the properties of different iron oxides. Figure 9 illustrates hematite (Fe_2O_3), wüstite (FeO) and magnetite (Fe_3O_4), depicting the thermodynamic stability of the different states of iron oxide with respect to temperature and $\Delta G°$ [30]. Line B represents the equilibrium for iron and magnetite, where states above the line the oxygen pressure is higher than required, meaning that magnetite is stable relative to iron. Furthermore, iron is the stable state below this line. This diagram establishes that in any reduction-oxidation equilibrium, the thermodynamically stable oxidized state of a metal is located above the Ellingham line, while the stable reduced state is positioned below the line [30].

In Figure 10, the red and blue lines represent the temperatures 600°C and 800°C, respectively. Since this study focuses on reduction of iron oxides with hydrogen, the lines drawn start from the *H* seen on the left-hand side of the diagram. By identifying the points where the iron oxide equations are at the set temperatures, it is possible to decide what hydrogen-to-water ratio the reactions occurs at the different temperatures. This can also redirect to Gibbs' free energy, mentioned in Chapter 2.5.1. The reactions forming FeO and Fe$_3$O$_4$ starts at 600°C and by drawing a line for both of these reactions from the *H* point until it interferes with the hydrogen-to-water ratio line, it shows that the ratio must be above 7 for the reaction to occur. For 800°C, the optimal ratio is established to lie above 5.
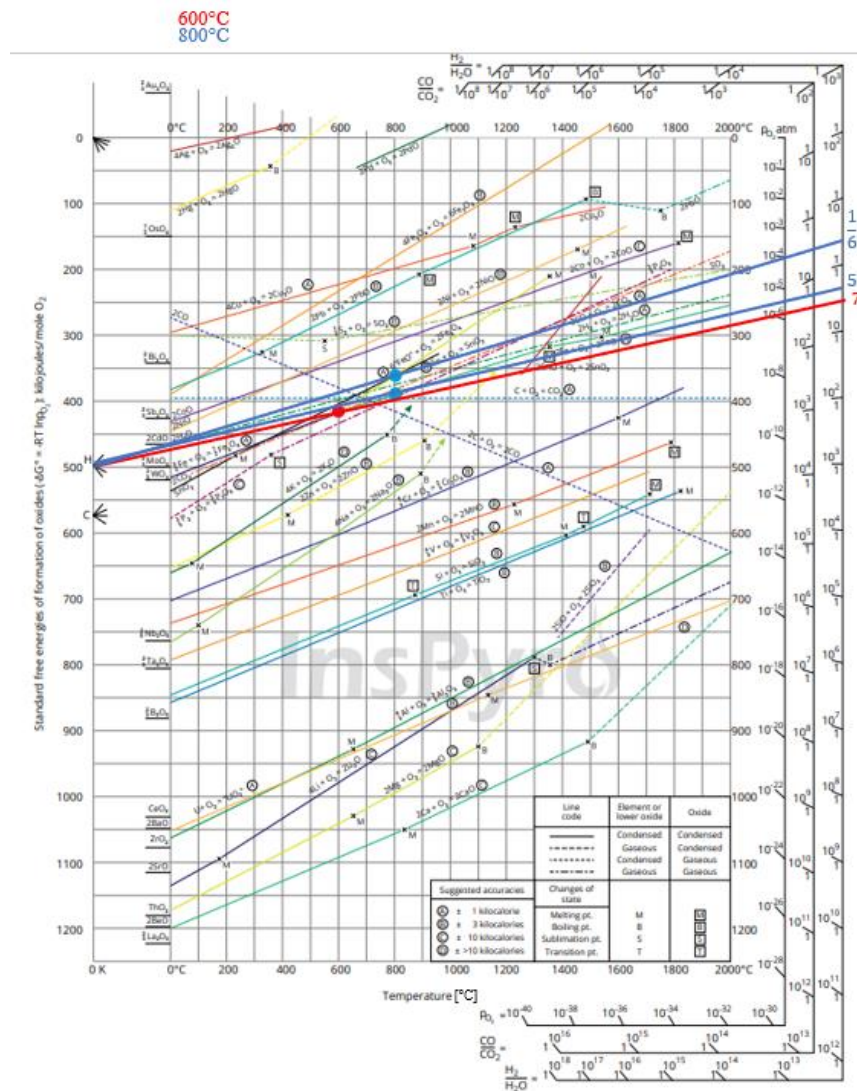
Figure 10: Ellingham diagram *[28].*

There are a few limitations following the Ellingham diagram, such as no information regarding the kinetics or the probability for other reactions to occur. Furthermore, the diagram does consider that reactants and the products are at equilibrium, which does not have to be true.

2.5.4 Kinetics of iron oxides reduction

Studying reaction kinetics is important to understand how fast the reactions occur. In this case, it is interesting to study how water vapour mixed with H_2-gas will affect reaction rate. Reduction of hematite can occur in different steps depending on temperature. For temperatures above 570°C, the reaction follows a three-step mechanism [21]:

$$3Fe_2O_3 + H_2 \rightarrow 2Fe_3O_4 + H_2O \tag{9}$$

$$2Fe_3O_4 + 2H_2 \rightarrow 6FeO + 2H_2O \tag{10}$$

$$6FeO + 6H_2 \rightarrow 6Fe + 6H_2O \tag{11}$$

For temperatures below 570°C, the reaction follows a two-step mechanism [21], and it is seen in Figure 8 that FeO is formed above this temperature:

$$3Fe_2O_3 + H_2 \rightarrow 2Fe_3O_4 + H_2O \tag{12}$$

$$2Fe_3O_4 + 8H_2 \rightarrow 6Fe + 8H_2O \tag{13}$$

Since the experiments in this study are taking place at temperatures above 570°C, the reactions will favour the three-step mechanism. Furthermore, the kinetics regarding temperature can be studied using the Arrhenius' equation, shown in Equation 14 [31]:

$$k = A \exp\left(-\frac{E_a}{RT}\right) \tag{14}$$

Where k is the rate constant, A is the frequency factor and E_a is the activation energy. The Arrhenius' equation shows that with an increase in temperature, the rate of reduction increases exponentially. Figure 11 shows, with the use of Arrhenius' equation, how temperature affects the reduction rate. The greatest increase in reduction rate happens during the earlier stages of the experiment, and eventually becoming less significant over time [31].
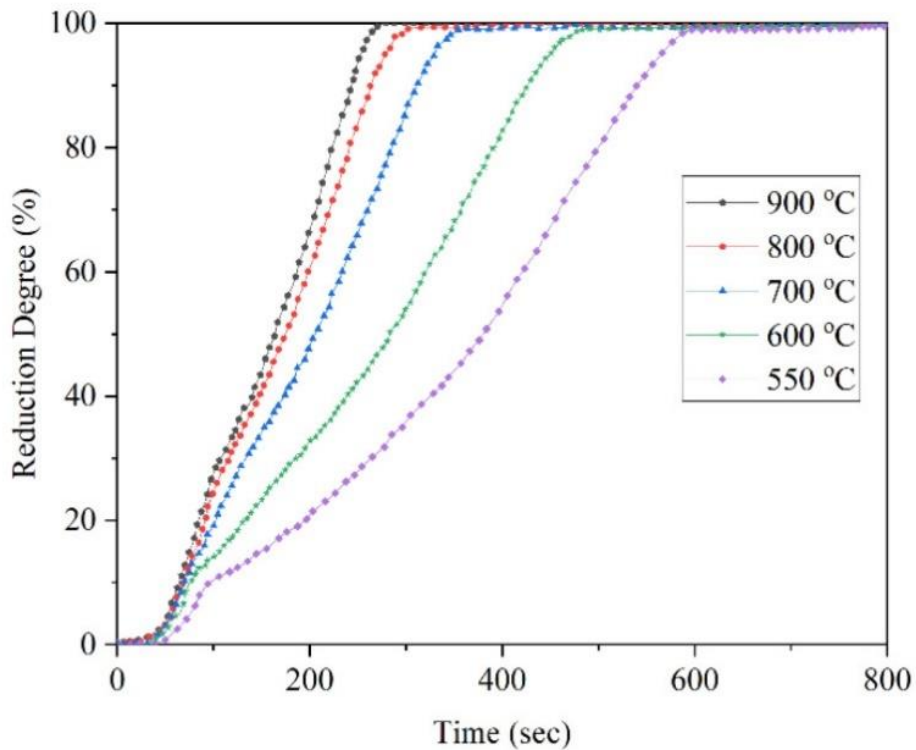
Figure 11: Effects of temperature on the reduction rate of hematite from BR *[31]*.

However, several other parameters are also important to consider when studying reduction kinetics. Morphology, mineralogy, and particle size are all parameters that can affect the reducibility of the BR-pellets. Additionally, it is important to consider how different H_2-H_2O compositions will affect the rate of reduction. Previous experiments suggests that higher levels of H_2O-vapour present in the gas mixture leaves a greater yield of FeO. This indicates that H_2O-vapour hinders diffusion of H_2-gas in the sample and thus preventing complete reduction of Fe_2O_3 to Fe. An example on how this affect reduction time is shown in Figure 12 [32].
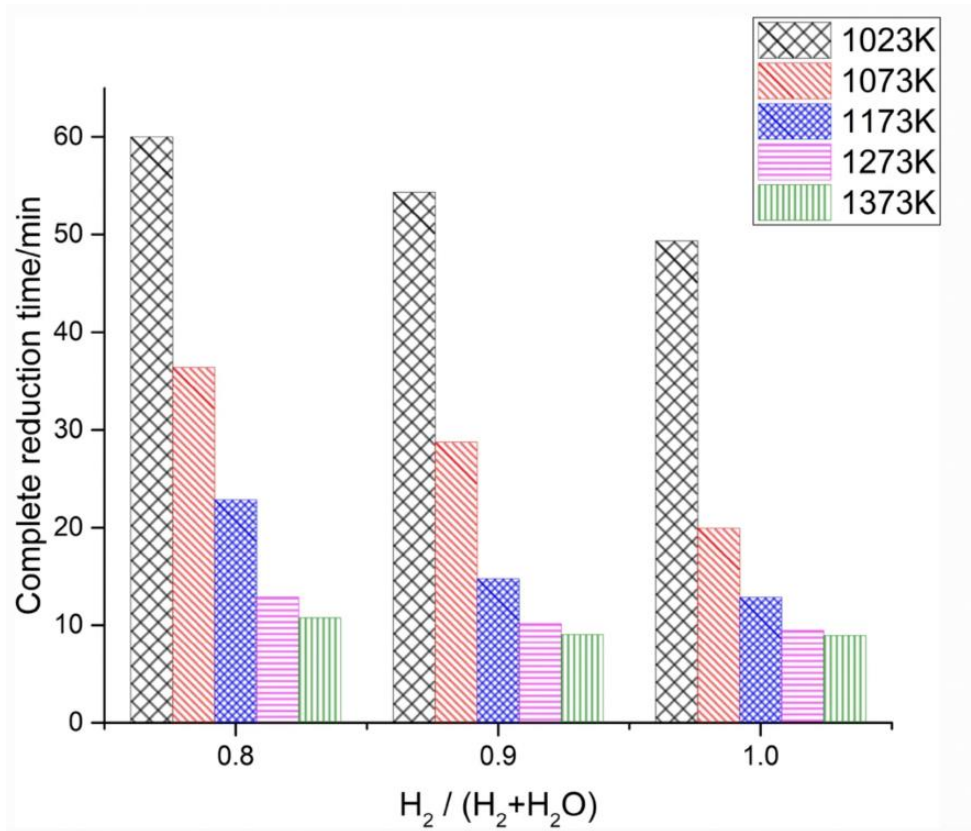
Figure 12: Relationship between H_2-composition and reduction time *[32]*.

Figure 12 also shows that, with higher temperatures, the H_2-H_2O composition becomes less significant. This indicates that temperature may be the most important parameter when it comes to reduction of BR-pellets.

As mentioned, diffusion is an important process that takes place during the reduction of BR-pellets. If the structure of the pellets is somewhat porous, the reducing gas can therefore pass through the surface and react closer to the core. If the particle is not porous enough, different iron-complexes can form on the surface, hindering further reduction inside the sample itself. Porosity can also change during the reduction itself, which can cause the reduction rate to slow down significantly. To understand how the different parameters affects and limits the reduction rate, the unreacted shrinking core model can be studied, shown in Figure 13 [25].
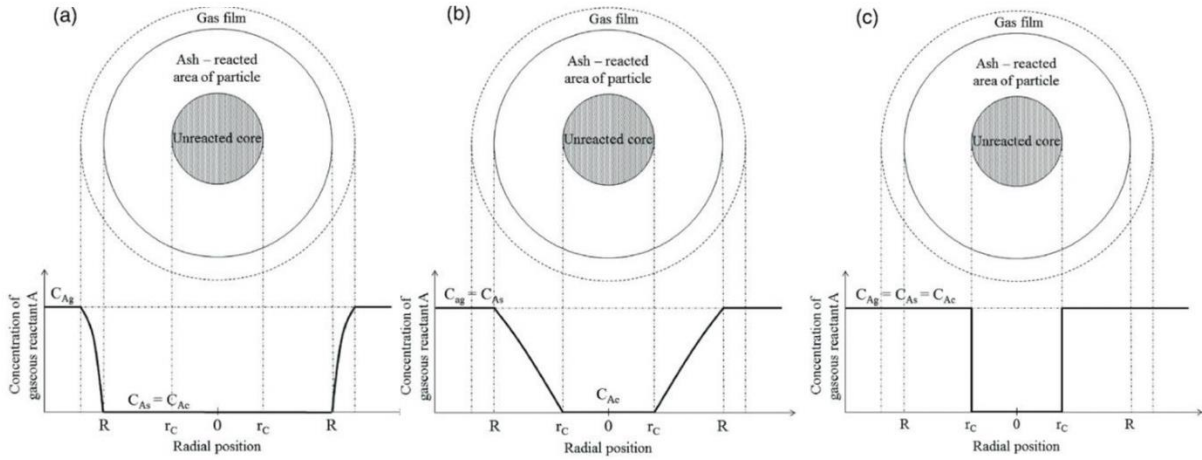
Figure 13: Rate-limiting steps, where a) is limitation by mass-transfer through the film, b) is limitation by pore diffusion, and c) is limitation by chemical reaction *[25]*.

C_{Ag} denotes the concentration of gas-phase reactant A in the reducing gas, C_{As} is the gas concentration at the outer surface of the particle, C_{Ac} is the equilibrium concentration of the reaction and r_c is the radius of the unreacted core.

These rate-limiting steps are characterised by how the concentration profile of the gaseous reactant A are related to the incoming gas stream and the reaction interface. Mass transport becomes rate-limiting if the chemical reaction happens fast, which in turn makes the difference in concentration between the gas and the reaction interface the driving force for the mass transfer. The corresponding result is therefore shown in Figure 13 a), and this phenomenon can be described by Fick's first law of diffusion, shown in Equation 15 [25].

$$J = -D \frac{d\varphi}{dx}$$

(15)

Where J is the diffusion flux, D is the diffusion coefficient, $d\varphi$ is the change in concentration of the particle, dx is the change in position, and $\frac{d\varphi}{dx}$ is the concentration gradient of the gas in the particle [33]. Limitation by mass transfer is only slightly dependent on temperature and is therefore more important to consider at higher reduction temperatures than the other rate-limiting steps [25].

Pore diffusion becomes the rate-limiting step if, during reduction, the pore size and distribution change to be smaller and less abundant. Also, if the material is not porous enough, the reducing gas is not able to diffuse into the core. This results in an insufficient reduction closer the core of the material. Furthermore, reduction starts at the surface layer of the material, creating a metallic iron layer which the gas must pass through as well. This can lead to the more inner oxides to be left unreacted, leading to solid-state diffusion to be dominant and therefore making diffusion the rate-limiting step. Additionally, as mentioned before, the presence of water vapour in the reducing gas mixture can obstruct the available reaction sites on the surface, impeding the diffusing of H_2 into the core and ultimately leading to significant reduction in the rate of reduction [25][26].

When the reduction temperature is between 500°C and 800°C, there are only slight increases in both porosity and surface area. For temperatures over 800°C, these parameters decrease drastically. As seen from Figure 15, the porosity and surface area are the highest for a temperature at 800°C [21].

Pellet size can also affect reduction rate significantly. The bigger the pellets, the more decrease in reduction rate. This happens because of shorter diffusion distances on the particles, and because smaller pellets increase the surface area between H_2-gas and iron oxides. As seen from Figure 14, the smaller the pellet size, the greater the reduction rate becomes earlier in the process. With longer durations, however, this becomes negligible, and at a certain point, the size becomes the rate-limiting step [25][26].
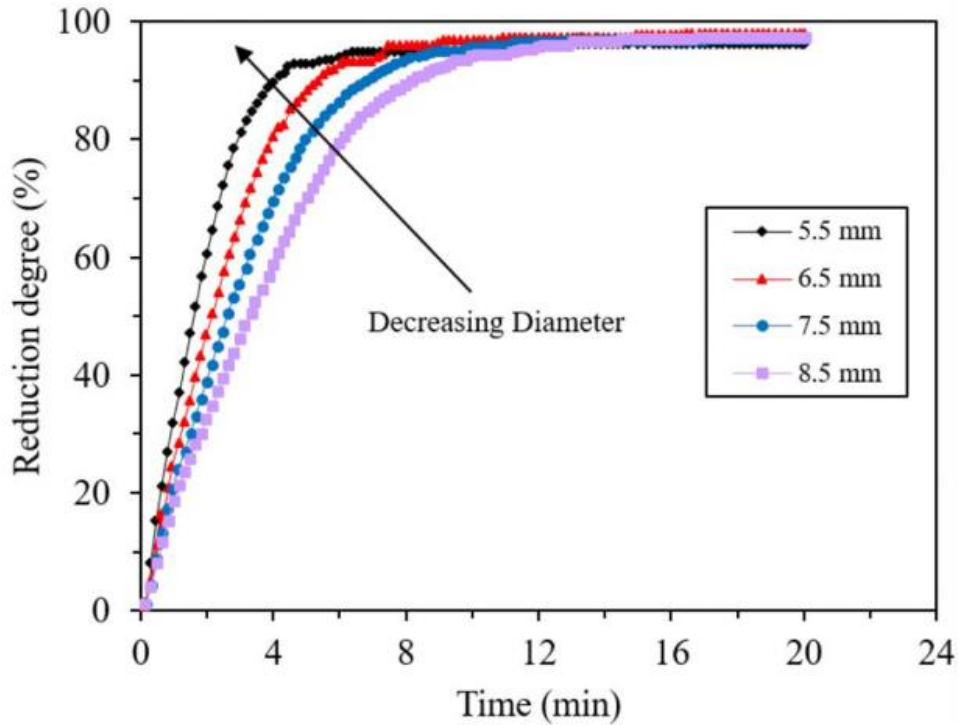
Figure 14*: Effect of hematite pellet size on reduction degree [31].*

2.6 Hydrogen reduction of BR pellets – previous research

Over the last couple of years, much research has been done on reduction of BR using H_2-gas. Kar et al. concluded that by increasing the reduction temperature, the number of iron-oxide complexes formed decreases, while formation of metallic iron increases, indicating faster kinetics with higher temperatures [21]. Velle et al. concluded that for lower temperatures than 1200°C, reduction time becomes increasingly important, as more metallic iron forms when more time is spent on the reduction [26]. Based on these works, both temperature and duration are crucial parameters to consider while conducting research on hydrogen reduction of BR-pellets.

Garg et al. concluded that when the reducing gas contains some level of humidity, and at a low temperature, the reduction degree does not fully reach 100% of theoretical value due to there being unreacted FeO left in the samples. Additionally, it was determined that differences in H_2-H_2O compositions does not affect the first stage of the reaction, Fe_2O_3 to FeO, as the apparent activation energy is not affected. On the other hand, this greatly affects the second stage of the reaction, FeO to Fe, as the apparent activation energy increases. The kinetics analysis also suggested that the

reduction at later stages is controlled by diffusion as H_2O molecules are bigger than the H_2 molecules, leading to difficulties in inter-diffusion and therefore hindering H_2-diffusion in the samples [32]. This indicates that with larger amounts of humidity, the reduction reaction becomes less efficient, and higher temperatures and longer reaction durations should be considered if the results are to reach 100% of the theoretical reduction degree value.

By utilizing BET and BJH analysis, in conjunction with SEM, it is possible to investigate alterations in pore size and distribution before and after H_2 reduction. Figure 15 shows an example on how porosity and surface area changes with different reduction temperatures done in a previous study [21]. BET, BJH and SEM are further discussed in Chapter 2.7.2 and 2.7.5.
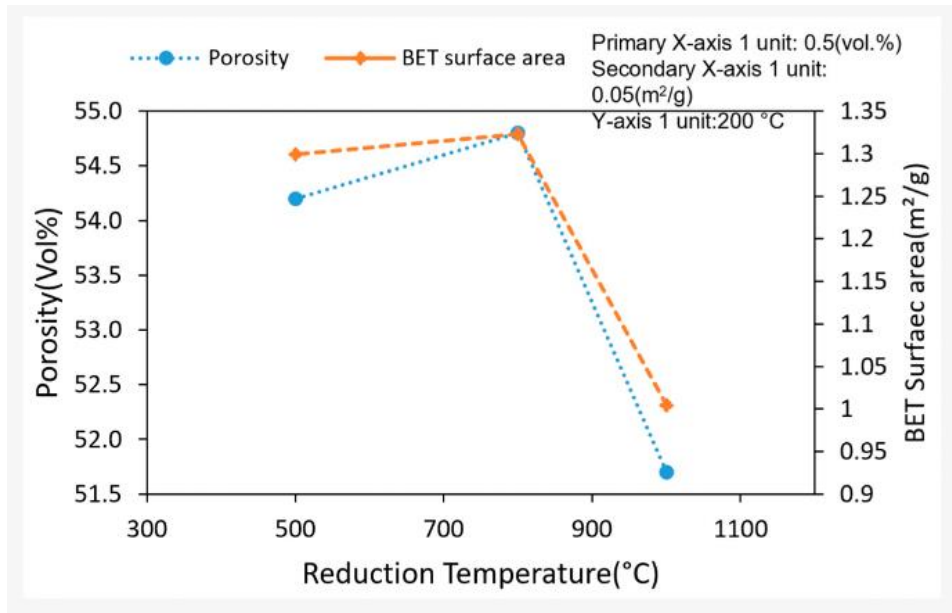
Figure 15: Porosity and surface area of BR-calcite pellets reduced at different reduction temperatures *[21]*.

2.7 Analytical methods

In this study, a combination of analytical techniques was employed to analyse sintered and reduced pellets. These techniques include, XRF, SEM, XRD which were used to investigate the elemental composition and morphology. Additionally, BET and BJH analyses were utilized to study the pore size and surface area of the pellet samples. The use of these analytical techniques allowed for a comprehensive characterisation of the samples, providing valuable insight into their properties and behaviour under different conditions.

2.7.1 X-Ray fluorescence (XRF)

X-Ray fluorescence (XRF) spectroscopy is used to determine the composition of the elements present in a sample. XRF is a non-destructive, rapid and precise analytical tool using the simple relation to the fundamental physics of atom-radiation interaction, called fundamental parameter [34]. The fundamental parameter assumes chemical homogeneity over the area exposed, meaning the reactants are in the same phase. Further on, it presumes that there is a "normal" attenuation of both primary and secondary radiation in the sample matrix. Lastly the geometry for the beam-sample detector has to be well defined and constant over the exposed area [34].

There are two main types of XRF analyses: Energy-dispersive (EDXRF) and wavelength-dispersive (WDXRF). EDXRF is preferred when doing a qualitative analysis. This is because of its capability to simultaneously determine 10-30 elements. In the case of analysing a light element, a poorer peak to background (PB) ratio is obtained compared to using a heavier element [35][36]. The energy of the X-Rays and the atomic number of the element that emitted them, are proportional to each other. This makes it possible to determine which elements are present and in what quantities, making this technique semi-quantitative. This method is also more inexpensive, unlike WDXRF which is more expensive. WDXRF is more precise and sensitive, but it requires more careful preparation [35].

2.7.2 Scanning electron microscope (SEM)

The scanning electron microscope is an analytical method where a beam of electrons is targeting on a very specific small spot on a polished reflecting surface. These electrons get collected back from the targeted object, are then amplified, and used to modulate the brightness of a cathode ray tube. The motion of the tube corresponds to the electron beam over the sample [37]. When using the SEM, the samples can be damaged by the electron beam over time. This can be prevented, or at least limited, by coating the sample with a protective metal, such as gold. The analytical tool does also make it possible to visualize the objects complexity and micro- and nano spaces.

The image formed by SEM can be made to depend on two different variations of electron emissions; backscattered- and secondary electrons imaging. These can be shortened to BSE and SEI respectively [38]. BSE are scattered electrons from the incident beam through large angles so they can re-emerge from the sample. The main difference between BSE and SEI is that BSE have a higher energy making it able to detect greater depths in the specimen [39]. These electrons reflect after an elastic interaction between the beam and the sample, showing high sensitivity to differences in atomic number. The brighter the material showing on the image, the higher atomic number is present. The secondary electrons originate from the atoms of the sample and are a result of an inelastic interaction, providing detailed surface information [40]. The average energy of BSE is less than the primary incident beam, but still within the same order of magnitude [41].

2.7.3 Energy disperse X-Ray-spectroscopy (EDS)

Energy disperse X-Ray spectroscopy is a widely used method to analyse an elements composition of solid matter. In conjunction with the use of SEM, it is possible to do an analysis on nanoparticles [42]. High resolution of the sample surface morphology and the qualitative information on elemental composition can both be achieved within the same scanned region provided by the electron microscope. The sample contains a distinct set of elemental energies, resulting in the emissions of X-Rays with specific energies that facilitate identification of the constituent elements.

The resulting image accomplished from the analysis consists of peaks. There are three kinds of peaks: sum-, escape- and diffraction peak [43]. Sum peaks are often found in XRF or EDS analysis. This peak appears when the energy corresponding to the energy of two photons. The higher number of photons impinging results in a higher intensity of a sum peak. Escape peaks are created in EDS

(EDX) spectra. When the photons interact with a silicon solid state detector, some Si atoms will excite to emit the charactered Kα X-Rays in the detector, which is when an electron cascades from L- to K-shell [44]. There are two different Kα radiations, Kα1 and Kα2, where Kα1 has a shorter wavelength but twice the intensity as Kα2. The intensity of this peak depends on the arrangement, shape, and size of the detector. Finally, the diffraction peak is detected when X-Ray incident on a large single crystal, when diffracted into the X-Ray detector. These types of peaks are found in XRF [43].

2.7.4 X-Ray diffraction (XRD)

The non-destructive technique for characterising crystalline materials, called X-Ray diffraction (XRD), provides information on phases, structural parameters and crystal orientations [45]. XRD relies on the principle of constructive interference between monochromatic X-Ray and a crystalline sample, which is generated through heating of a filament in a cathode ray tube, resulting in the emissions of electrons. The monochromatic radiation is then collimated to concentrate towards the sample, directly. The Kα X-Rays' specific wavelength are characteristic of the target material: Cu, Fe, Mo, Cr, where copper is the most common target material for single-crystal diffraction. The intensity of the reflected X-Rays is recorded as the sample and detector rotates. The X-Ray signal will get processed by a detector that converts the peaks given when the geometry of the incident radiation satisfies Braggs' law. The signal converts the signal to count rate, which will pop up on the computer monitor.

Bragg's law helps to determine the atomic structure of crystals by analysing scattered X-Rays from the incident with the crystal. By measuring angles and intensities of the radiation determines the positions of the atoms and creates a three-dimensional model of the crystal's structure. Mathematically, the law can be expressed as shown in Equation 16. Where λ is the wavelength of the X-Rays, n is an integer called the order of reflection, d is the spacing between atomic planes in the crystal lattice, and finally θ is the angle between the beam and the crystal lattice planes [46]. The assumption being made in deriving the Bragg's equation is that the planes of atoms are responsible for a diffraction peak which behaves as a specular mirror. The angle of reflection is then equal to the incidence θ [20].

$$n\lambda = 2d \ \sin(\theta) \tag{16}$$

The angle θ, formed when perfectly parallel, monochromatic X-Rays is incident on a particular crystal plane, is called the Bragg angle [46]. Shown in Figure 16 is how the electron beams get diffracted by a crystal. The beams named *1* and *1a,* strike the atoms K and P, which gets scattered in all directions. All the X-Rays scattered by the atoms in the first plane, that are parallel to *1'* add their contributions to the diffracted beam. A diffracted beam consists of many rays scattered in different directions, which work together to produce a stronger overall beam [46].
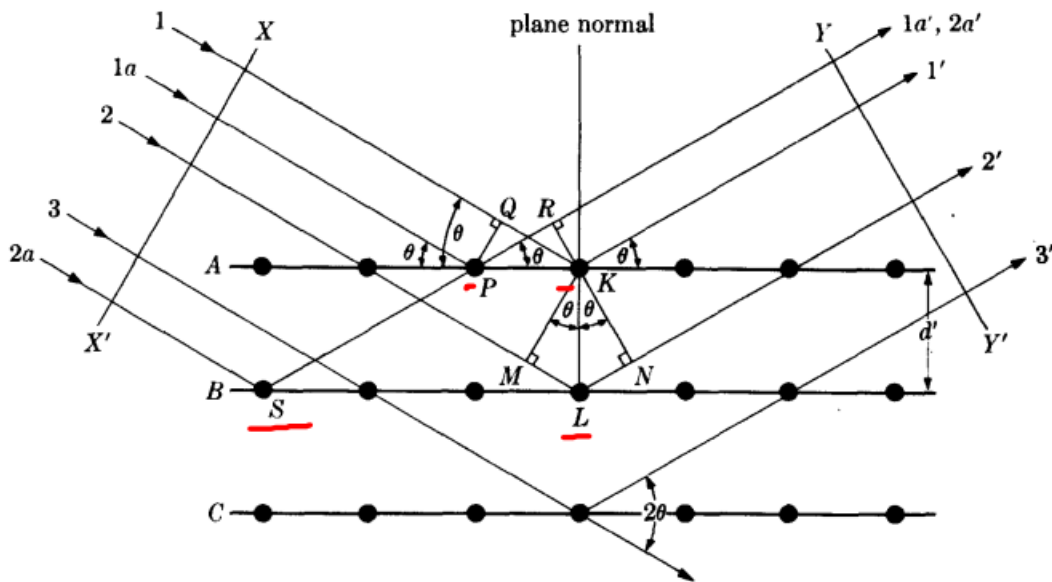

Figure 16: X-Rays diffracted by a crystal *[46].*

A goniometer is used in this analysis to maintain the angles θ and 2θ. These angles are such that the sample rotates in the path of the collimated X-Ray beam, and the X-Ray detector rotates to collect the diffracted X-Rays, respectively [45].

2.7.5 Brunauer–Emmett–Teller and Barrett-Joyner-Helanda (BET and BJH)

The Brunauer-Emmett-Teller (BET) method is used to characterise the surface area of porous materials and are typically reported in units of square per meter, m^2/g. This is done by semiempirical fitting of gas-adsorption isotherms, where nitrogen gas is used at 77K. The method relies on Langmuir's research, which postulates a stoichiometric binding of gas molecules with lattice sites on a flat substrate. This offers a measurable representation of the substrates surface area [47]. When the temperature is about 77K, the interaction between the gas molecules and the surface is governed by Van der Waals (VDW) forces. This results to a reversible physisorption of gas molecules on the surface, and the resulting amount of gas absorbed can be used to determine surface area of the sample.

The Barrett-Joyner-Helanda (BJH) approach characterises and calculates the pore size distribution. Low pressure mercury porosimetry is used to characterise the macropores of the pellets [48]. The same gas absorption method as in BET is also used in BJH, where with BJH the resulting data is the samples pore size. Shown in Figure 17 is a schematic of the BET procedure.
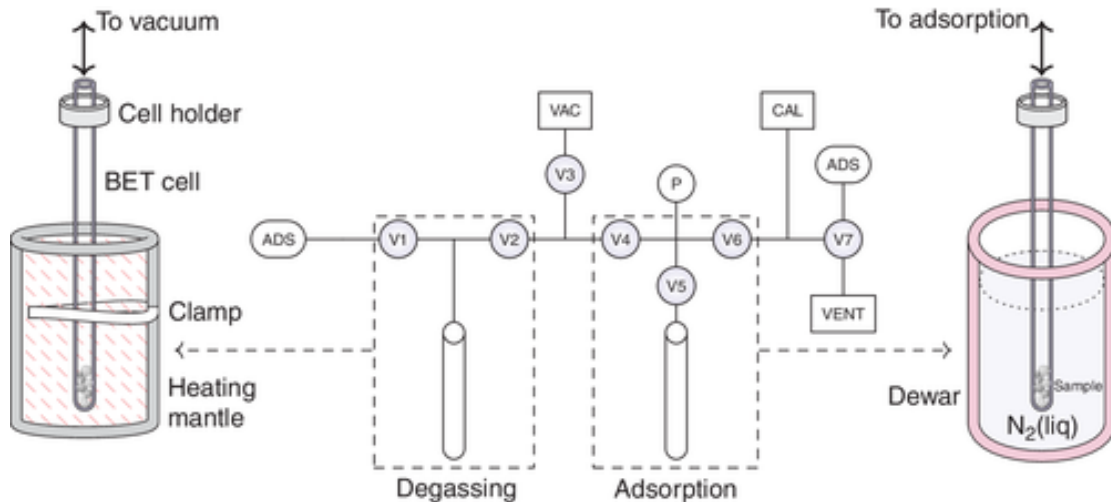

Figure 17: Schematic of BET apparatus equipped with vacuum (VAC), calibration (CAL), adsorbate (ADS), pressure gauge (P) and V1-V7 valves *[48]*.

3. Materials and methods

The following chapter outlines the experimental work that has been utilized in this study. The aim of this investigation was to reduce several samples with different H_2-H_2O mixtures at 600°C and 800°C. These products were then analysed with XRF, XRD, SEM, BET and BJH.

3.1 Raw materials and preparation

The Bauxite residue (BR) that was used in this study was received from Mytilineos, Greece. The sample, weighing 1212,76 kg, was subjected to drying to eliminate any residual moisture and regulate subsequent process chemistry. This was achieved by placing the samples in an oven overnight. The fine calcite powder ($CaCO_3$), was received from Omya, Norway. The powder was utilised to produce calcium hydroxide ($Ca(OH)_2$), shown in Equation 17. The bauxite residue used in this study is presented in Figure 18.

$$CaCO_3 \rightarrow CaO \rightarrow Ca(OH)_2 \tag{17}$$

Figure 18: Bauxite residue in powder form.

3.2 Pelletising and sintering

The BR was pelletised into pellets with a diameter of 3-4 mm with a disc- pelletiser, using approximately 10wt% H_2O to merge the BR together. Bigger pellets were re-added to the pelletiser to create smaller pellets. The method using the disk-pelletiser is visualised in Figure 19. The pellets were then dried for 3 days. When the drying process was finished, the pellets were added to a muffle furnace for sintering. This process was executed at 1150°C under atmospheric pressure for 2 hours. After sintering, the pellets were cooled naturally inside the muffle furnace for 8 hours before being taken out of the furnace.

Figure 19: Disc-pelletiser w/ H_2O and a shovel.

3.3 Reduction furnace, Entech-18

To reduce the sintered pellets, the reduction furnace Entech-18 were utilized. Shown in Figure 20 are both the furnace and a schematic of its inside. The furnace consists of a cylinder-shaped alumina tube, surrounded by a cooling element that is twined around the furnace. A thermocouple was inserted from the top of the furnace to measure the temperature of the crucible, sample holder, illustrated in Figure 20. The furnace features a gas inlet positioned at its lower section, while the gas, having interacted with the sample, were subsequently released through the top of the furnace. The induction heating system was implemented through the utilization of heating elements located on each side of the furnace.
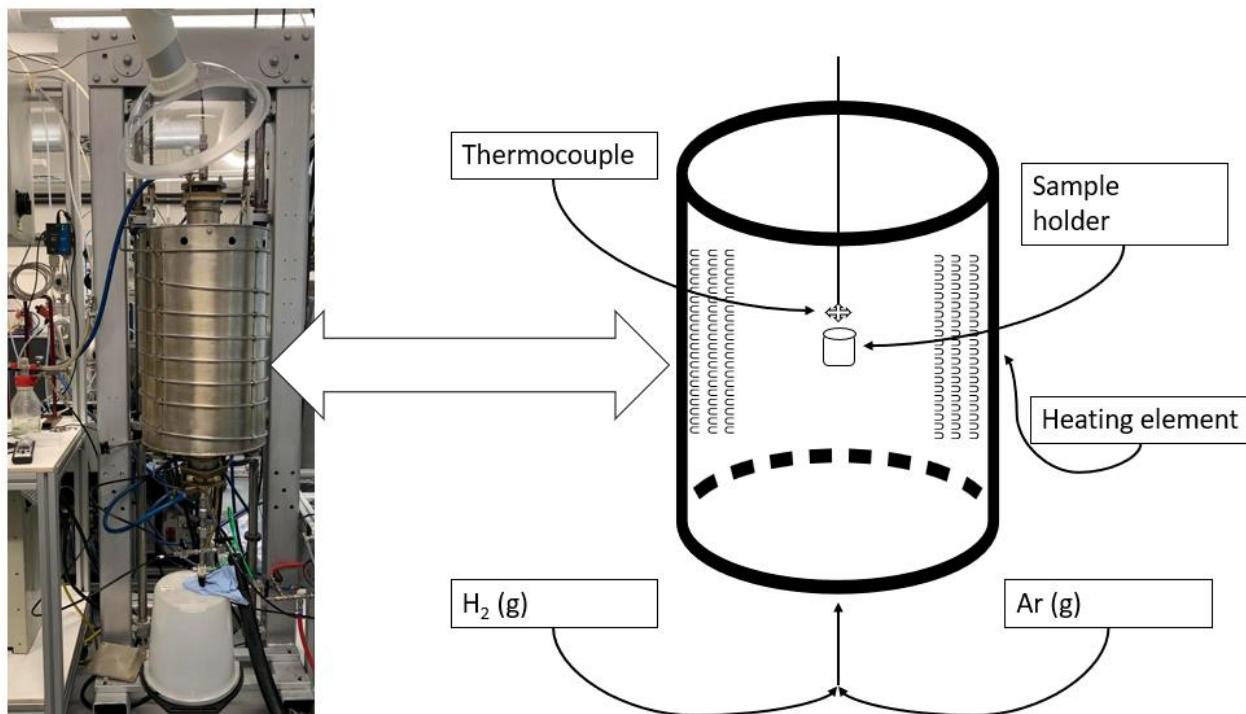
Figure 20: Entech-18 furnace with a schematic describing the furnaces insides.

Before every experiment, a leak test with helium was performed to ensure that there were no gas leakages. The leak-test is very important for many reasons, such as safety, efficiency, and environmental protection. After the leak test, the humidifier was flushed with dry argon gas to ensure that the humidifier was as precise in reaching the desired humidity as possible. After flushing, H_2-gas was introduced. The gas entered the humidifier and was flushed through an off-gas line until the desired humidity level was reached. While this was ongoing, the furnace was heated up using argon gas to 635°C and 835°C. This was due to temperature differences between the crucible and wall. This was done at the heating speed of +10°C/min. When the desired temperature was reached, the off-gas and argon line was closed and the line going into the furnace from the humidifier was opened. The experiment then ran for 2 hours, before the furnace was turned off to cool by introducing argon again. The furnace was left overnight to allow the cooling process to take place.

Both flushing gasses, He and Ar, had a flow of 1 NL/min, while H_2 had different flows respecting the different compositions of H_2-H_2O mixture. Shown in Table 5 are the varied flows of the hydrogen gas, where the total gas flow remains at 1 NL/min even though the composition changes.

Table 5: Hydrogen inlet flows at different H_2-H_2O compositions.

H_2-H_2O composition	Flow [NL/min]
1,00-0,00	1,00
0,95-0,05	0,95
0,85-0,15	0,85
0,75-0,25	0,75

The pellets were added in the furnace from the bottom, where the gas inlet is. The samples are put in a sample holder, crucible, which was then glued to a ceramic stick using an Al fix gel. Each experiment used approximately 20g pellets. The sample holder was positioned by detaching the gas tubes and wires, followed by reattachment after positioning the sample holder. The placement of the thermocouple was also adjusted to ensure accurate measurement of the crucible temperature, with the thermocouple located a few centimetres above the sample.

3.4 Characterization

3.4.1 Chemical composition (XRF)

Both raw and sintered pellets were crushed down to powder using a mortar, shown in Figure 21, before being sent to Degerfors Labs in Sweden and Sintef Norlabs AS for XRF analysis.

Figure 21: Crushing the sintered pellets using mortar, making them ready for XRF.

3.4.2 Phase analysis by XRD

The XRD analysis was done in a DaVinci-1™ instrument where 5 of the sintered pellets were crushed using a mortar. Furthermore, 2 g of each of the reduced samples were grounded down to a fine powder in a ring mill. The fine powder was then added to a back-loader sample holder, shown in Figure 22. The ring mill's settings for crushing the pellets were 700 rpm for 3 minutes. For analysis, a crystalline setting was chosen, and the following parameters were used as given in Table 6.

Figure 22: A back-loader sample holder used for the XRD analysis.

Table 6: Parameters used for XRD-analysis.

Scan duration [min]	Start degree [degree]	Stop degree [degree]	Step [degree]
60	10	80	0,2

3.4.3 Preparation and microstructural analysis by SEM

Four samples were prepared initially, compromising two intact pellets and two pellets that had been halved. The samples were placed in a Struers LaboPress-1™ machine for mounting. For moulding, PolyFast™ resin was used. The pellets were mounted for 6 minutes under a pressure range of 20-25 kN and washed with water for 3 minutes.

Figure 23: Polishing machine, Saphir 550.

The newly prepared SEM samples consisted of 4-7 pellets, both sintered and reduced. These were each moulded in a plastic cast using 14,3 g Epoxy resin and 1,7 g hardener, which was stirred by hand for 1 minute to combine the mixtures together. HSE data for the chemicals used is presented in Appendix VIII. Furthermore, the samples were put in a CitoVac™ machine to remove bubbles from the pellets. The samples were stored and left to dry for at least 12 hours.

The following day, the samples were taken out of the plastic cast, then grinded and polished in the Saphir 550™ machine, shown in Figure 23. The samples were rubbed with sandpaper (grit size: 320 µm, 500 µm, 800 µm, 1200 µm, 2400 µm, 4000 µm) for 3 minutes with a pressure of 5 N. After each polishing step, the samples underwent a thorough washing process using soap and water. For grit sizes exceeding 1200 µm, the sample was subjected to further treatment after

washing with soap and water. The specimen underwent immersion in ethanol and sonicated for a duration of 5 minutes in an ultrasonic bath. When the samples were taken out of the bath, additional ethanol was used to wash the surface before being put back into the Saphir machine. To finish off, the sample was polished with a diamond coated abrasive for 30 seconds. After the grinding and polishing process, the samples were subjected to a 30-second coating of gold utilizing a sputter coater, S150B. The finished prepared samples were then put in the SEM machine to be analysed, seen in Figure 24.
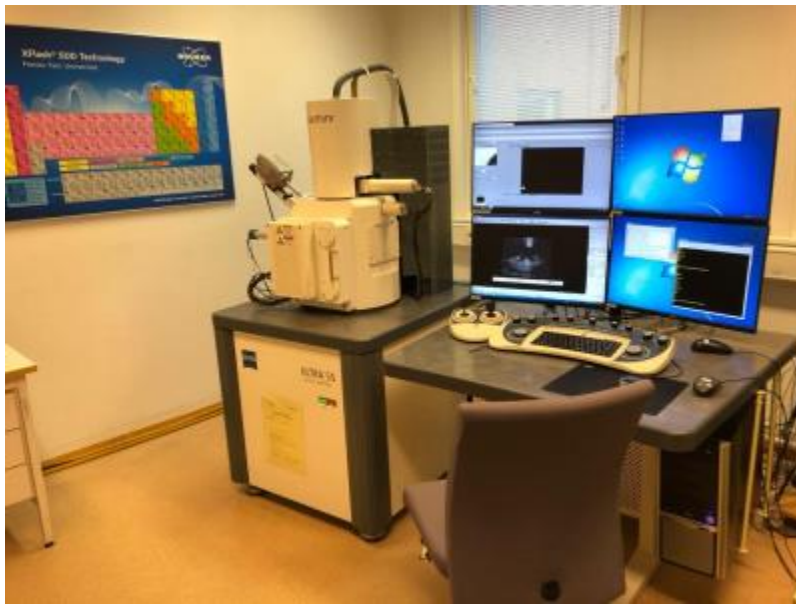

Figure 24: Zeiss – Ultra 55 – FEG – SEM machine [49].

3.4.4 Surface area and pore size by BET and BJH

The instruments used for BET and BJH were Micromeritics 3Flex 3500 and Micromeritics Degas Smartprep for 3Flex, shown respectively in Figure 25 and 26. First the samples, BR pellets, were weighed with the tube used for the analysis. Continuing, the tube with the sample were degassed with nitrogen gas by putting the silver rod inside the tube, and sealing it with a cap. The degassing lasted until the next day, where the tube was then put in the 3Flex 3500. The vessel in Figure 25 was filled with liquid nitrogen, before the sample tubes were fastened on the top of the machine with an isothermal cap. This was left until the day after, where the results were ready to be obtained.

Figure 25: Micromeritics 3Flex 3500.

Figure 26: Micromeritics Degas Smartprep for 3Flex.

4. Results

The following results will be presented in the form of figures and tables where this study aims at investigating the effects of H_2-H_2O mixtures on reducibility of bauxite residue – CaO sintered pellets. Additional results can be found in the appendices.

4.1 Pelletising & sintering

Before starting the reduction experiment, the pellets had to be weighed. Figures 27 and 28 show the pellets before and after sintering, respectively. The total weight of the dried pellets is 845,21g, and the sintered pellets have a total weight of 540,54g. This gives a mass loss of 36%, see Appendix III for calculations, where Equation 18 was used.

$$\%Mass\ loss\ = \ \frac{Mass\ loss}{Mass\ before} \cdot 100\% \tag{18}$$

Figure 27: BR pellets

Figure 28: Sintered BR pellets.

4.2 XRF

Upon analysis using XRF, the raw BR and the sintered and dried pellets that were dispatched to Degerfors Labs in Sweden yielded the following outcomes, showed in Tables 7 and 8, respectively. The paper received from Degerfors Labs can be seen in Appendix II.

Table 7: Wt% of compounds present in raw BR.

Compound	Wt%
Al_2O_3	22,0
CaO	8,8
Fe	28,5
K_2O	0,09
MgO	0,23
MnO	0,08
Na_2O	3,1
P	0,05
S	0,38
SiO_2	7,1
TiO_2	5,0

Table 8: SEM imaging of reduced pellets at 200x for 600°C with 0%, 5%, 15% and 25% humidity

Compound	Wt%
CaO	29,0
MgO	0,37
SiO_2	7,65
Al_2O_3	23,1
Fe_2O_3	30,5
MnO	0,04
Cr_2O_3	0,18
V_2O_5	0,15
TiO_2	3,86
NiO	0,06
Na_2O	3,60
K_2O	0,10
P_2O_5	0,12
SO_3	1,03
ZrO_2	0,11
SrO	0,03
Co_3O_4	0,02

The compound of interest is primarily hematite (Fe_2O_3). In addition, alumina (Al_2O_3) is also of interest. This is due to what intermediate phases these compounds can create during reduction. Also, more amounts of CaO are present in the sintered pellets. This is due to addition of $Ca(OH)_2$.

4.3 Reduction experiments

Table 9 shows the results of the reduction experiments. To determine the reduction degree and mass loss in percentage, the following formulas were used, shown in Equations 18 and 19. For further details on calculations, see Appendix III.

$$\%W_{red} = \frac{\Delta W_{red}}{W_{O,Fe_2O_3}} \cdot 100\% \tag{19}$$

ΔW_{red} denotes weight loss during the experiments and W_{O,Fe_2O_3} denotes the total mass of oxygen in hematite.

Table 9: Reduction experiments with mass loss and reduction degrees.

Experiment no.	Gas comp. [H_2-H_2O]	Temp [°C]	Mass before [g]	Mass after [g]	Mass loss [g]	Mass loss [%]	Reduction degree [%]
1	100%-0%	600	20,0801	19,1328	0,9473	4,72	49,64
2	95%-5%	600	20,0191	19,5329	0,4862	2,43	25,56
3	85%-15%	600	20,0764	19,7288	0,3476	1,73	18,22
4	75%-25%	600	20,0273	19,7288	0,2985	1,49	15,68
5	100%-0%	800	20,0664	18,6885	1,3779	6,87	72,26
6	95%-5%	800	20,0073	18,6412	1,3661	6,83	71,85
7	85%-15%	800	20,0757	18,7507	1,325	6,60	69,45
8	75%-25%	800	20,1392	19,7143	0,4249	2,11	22,20

4.4 Characterisation with different analytical methods

The examination of the sintered and reduced pellets using SEM, as well as the testing with various combinations of H_2-H_2O mixtures, produced the subsequent findings.

4.4.1 SEM imaging

In order to obtain a comprehensive understanding of the diverse samples, SEM imaging was used. The following images being presented have been analysed at the magnifications 200x, 500x and 2000x. Figure 29 presents the sintered pellets.
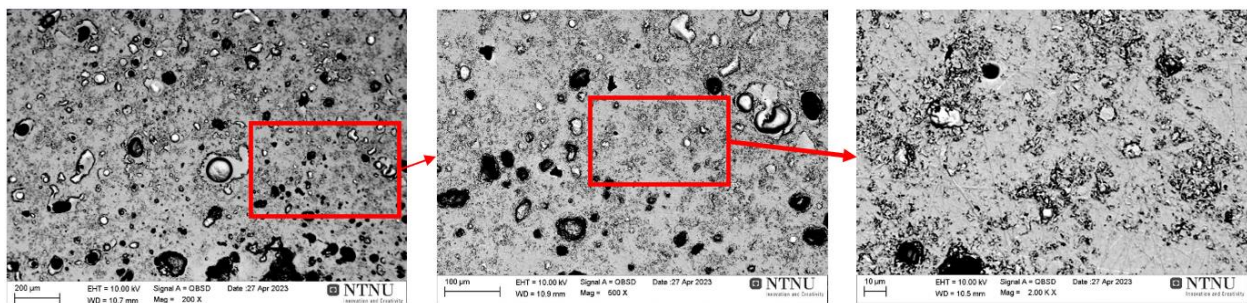

Figure 29: Images of sintered pellets at 200x, 500x and 2000x.

Continuing with SEM images, Figure 30-33 shows the reduced pellets at 600°C with different humidities.
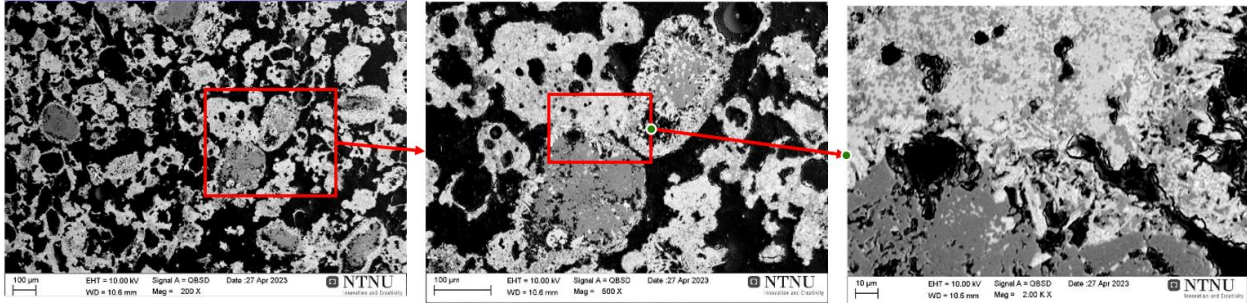
Figure 30: Images of reduced pellets with 0% H_2O at 600°C at 200x, 500x and 2000x.
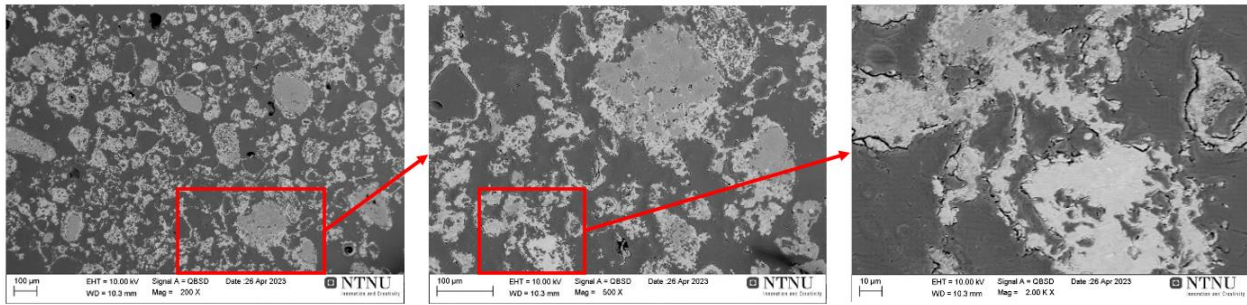
Figure 31: Images of reduced pellets with 5% H_2O at 600°C at 200x, 500x and 2000x.
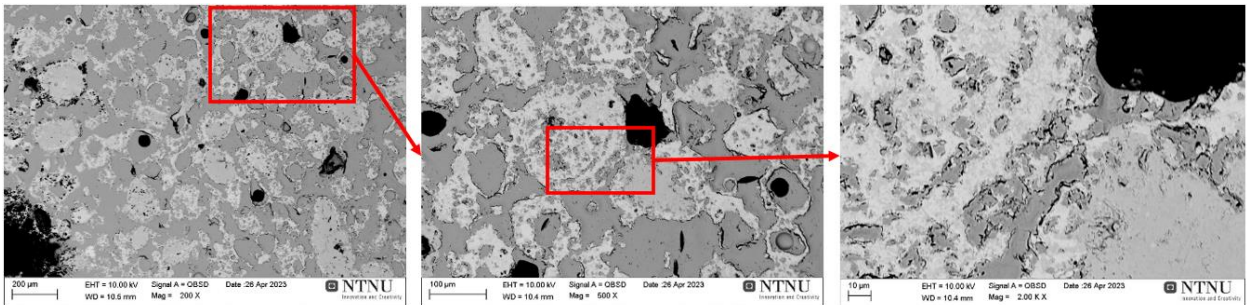
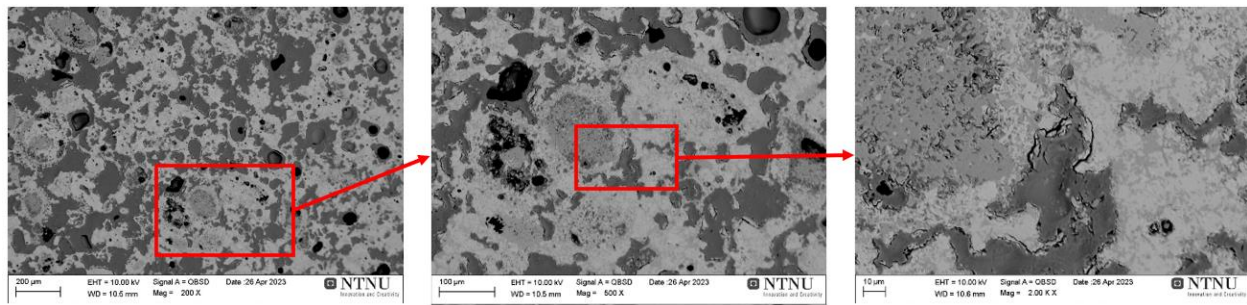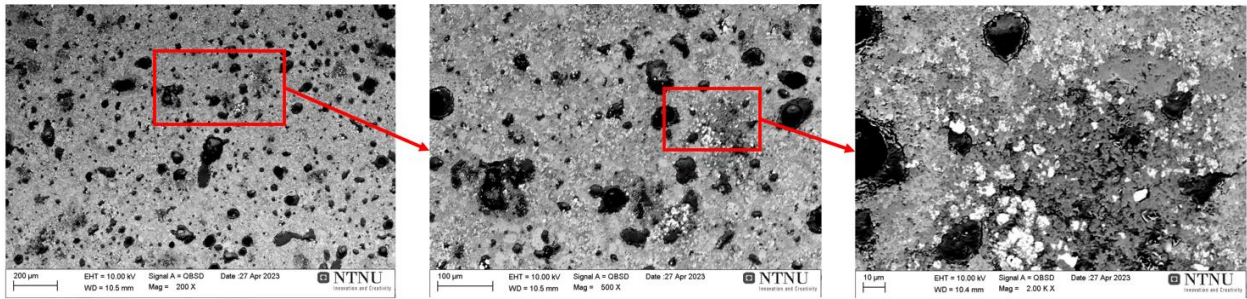**Figure 32:** Images of reduced pellets with 15% H_2O at 600°C at 200x, 500x and 2000x.

Figure 33: Images of reduced pellets with 25% H_2O at 600°C at 200x, 500x and 2000x.

The following images 34-37 displays the SEM images for the reduced pellets with different humidities at 800°C.

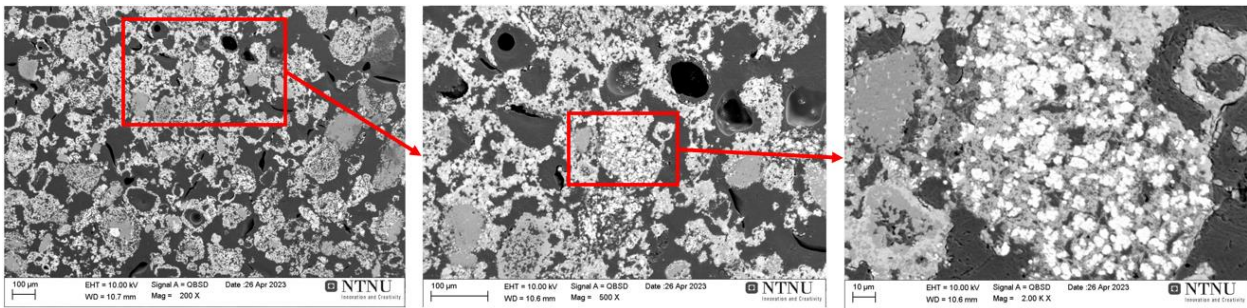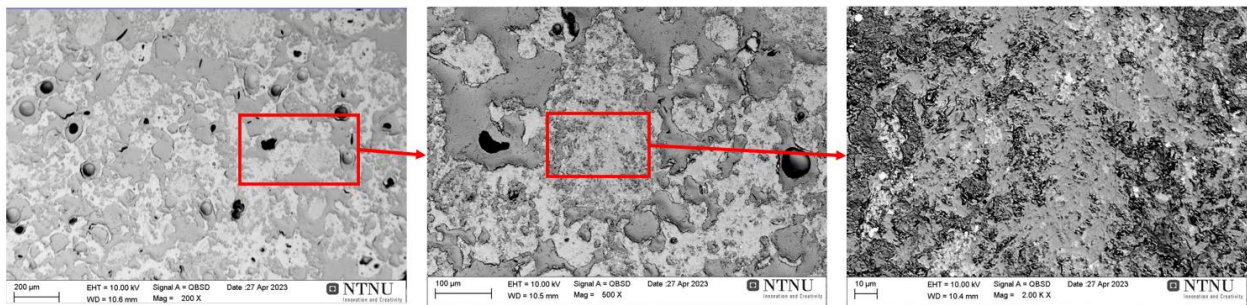**Figure 34:** Images of reduced pellets with 0% H_2O at 800°C at 200x, 500x and 2000x.

Figure 35: Images of reduced pellets with 5% H_2O at 800°C at 200x, 500x and 2000x.

Figure 36: Images of reduced pellets with 15% H_2O at 800°C at 200x, 500x and 2000x.
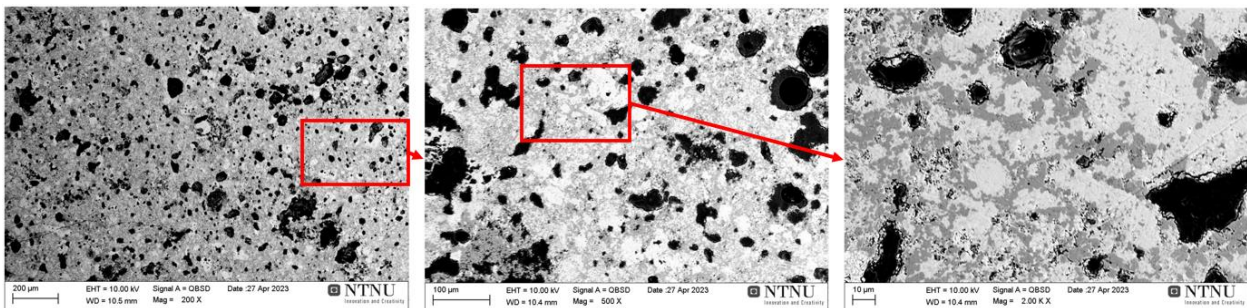

Figure 37: Images of reduced pellets with 25% H_2O at 800°C at 200x, 500x and 2000x.

4.5 EDS (SEM)

Following results demonstrate the outcome of the EDS analysis, in which X-Ray mapping provided information on the elements present in the reduced and sintered pellets. In order to discern the correspondence between compounds and their respective colours, the lower left-hand portion of each hue provides information regarding this. The raw data for point analysis can be found in Appendix IV, while Appendix VII contains unused EDS data from a SEM machine that was used previously.

4.5.1 EDS – point analysis, sintered pellets

The results of point analysis conducted on various samples are presented in the tables and figures below. Each table is accompanied by a corresponding figure indicating the locations of where the points were taken. Table 10 and Figure 38 presents the point analysis of the sintered pellets. Based on the molar concentrations of the species, the type of the phase was estimated as presented in Table 10.

Table 10: Atom percent [at%] of each element for sintered pellets.

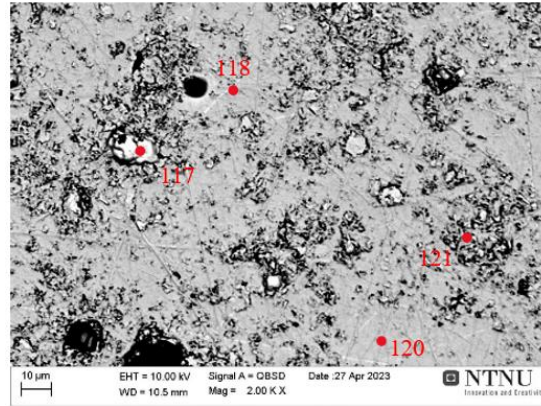| Sample	Point	Fe [at%]	Si [at%]	Ca [at%]	Al [at%]	Ti [at%]	Na [at%]	Mg [at%]	O [at%]	Est. Phase
Sintered	117	29,67	15,02	20,65	17,22	3,88	-	-	8,04	Brownmillerite
	118	35,58	22,88	22,00	16,91	1,44	0,97	0,32	-	Gehlenite
	120	36,29	20,37	20,38	17,89	3,05	1,81	0,21	-	Gehlenite
	121	45,44	12,31	23,26	5,02	7,11	0,69	0,03	6,13	Brownmillerite (Hematite *)

* Likely due to low amounts of aluminium

Figure 38: Point analysis on sintered pellets.

4.5.2 EDS – point analysis, reduced pellets at 600°C

Furthermore, Table 11 and Figure 39 shows the point analysis results from the reduced pellets with different humidities at 600°C. Based on the molar concentrations of the species, the type of the phase was estimated as presented in Table 11.

Table 11: Atom percent [at%] of each element for reduced pellets at 600°C with different humidities.

Sample	Point	Fe [at%]	Si [at%]	Ca [at%]	Al [at%]	Ti [at%]	Na [at%]	Mg [at%]	O [at%]	Est. Phase
0% H_2O 600°C	107	57,00	1,70	8,85	13,28	0,20	3,49	2,43	13,05	Iron, Wüstite
	108	25,10	1,40	31,48	4,11	8,30	0,51	-	29,10	Srebrodolskite
	110	7,57	15,93	25,95	20,52	0,19	0,23	0,07	29,54	Gehlenite
	111	7,84	1,43	11,05	38,53	0,07	14,91	-	26,16	$NaCaAlSiO_6$ *
5% H_2O 600°C	43	4,11	-	12,17	39,49	0,69	11,93	-	26,56	Srebrodolskite
	45	56,65	0,41	23,85	0,29	2,52	-	0,10	16,19	Wüstite
	49	56,15	0,36	19,90	0,73	2,55	-	0,18	20,13	Wüstite
15% H_2O 600°C	51	8,21	2,99	9,68	55,64	0,35	5,06	0,02	18,05	Srebrodolskite
	52	8,02	7,46	19,21	27,31	-	3,84	-	14,06	Gehlenite
	53	41,94	5,31	16,87	18,14	2,13	1,36	0,81	13,42	Srebrodolskite
25% H_2O 600°C	54	11,09	2,19	13,41	42,95	0,02	10,40	0,02	19,92	Srebrodolskite
	55	40,04	-	11,56	14,20	-	-	2,51	19,10	Wüstite
	56	22,22	0,99	30,19	6,90	7,33	-	0,11	32,26	Brownmillerite **
	57	7,74	17,32	27,83	21,51	0,13	0,06	0,05	25,36	Gehlenite

* Sodium calcium aluminium silicate   ** Most likely because of chemical composition
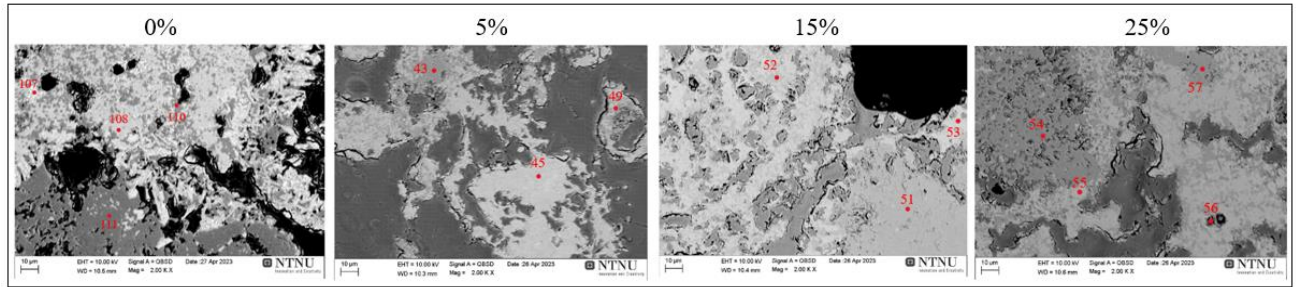
Figure 39: Point analysis spots on the reduced pellets at 600°C with different humidities at 2000x.

4.5.3 EDS – point analysis, reduced pellets at 800°C

Finally, Table 12 and Figure 40 displays the at% of the elements found in the reduced pellets at 800°C with different H_2-H_2O composition. The phase type was estimated based on molar concentrations of the species, as presented in Table 12.

Table 12: Atom percent [at%] of each element for reduced pellets at 800°C with different humidities.

Sample	Point	Fe [at%]	Si [at%]	Ca [at%]	Al [at%]	Ti [at%]	Na [at%]	Mg [at%]	O [at%]	Est. Phase
0% H_2O 800°C	112	95,65	2,43	0,17	0,69	0,10	0,51	0,45	-	Iron
	113	55,42	1,86	20,33	4,08	5,16	0,26	0,13	12,77	Srebrodolskite
	115	8,88	18,29	26,50	19,68	-	0,42	0,37	25,86	Gehlenite
	116	9,33	4,34	12,14	38,00	0,12	4,88	0,83	30,36	Mayenite
5% H_2O 800°C	58	4,56	1,48	10,58	34,08	-	13,90	0,18	35,22	Mayenite
	59	32,85	0,22	26,55	1,60	6,73	0,18	0,04	31,83	Srebrodolskite (Perovskite *)
	60	23,64	1,05	23,79	7,05	1,96	1,44	0,32	40,73	Srebrodolskite
15% H_2O 800°C	99	95,66	2,97	1,17	0,20	-	-	-	-	Iron
	100	13,68	2,98	13,23	44,91	0,05	12,05	-	13,11	Srebrodolskite
	101	21,23	4,70	10,73	46,07	-	8,94	0,22	8,10	Srebrodolskite
	102	38,40	3,44	14,11	30,48	0,73	6,35	0,79	5,69	Srebrodolskite **
25% H_2O 800°C	103	48,16	1,89	6,07	13,27	0,13	4,89	3,14	22,45	Wüstite
	104	9,06	15,05	27,87	20,41	0,33	0,12	-	27,15	Gehlenite
	105	25,76	2,04	26,30	13,19	0,99	4,54	0,06	27,12	Srebrodolskite
	106	31,24	1,71	31,93	5,17	1,80	0,57	-	27,57	Srebrodolskite

* Possibly mixed in   ** Limited amount of oxygen
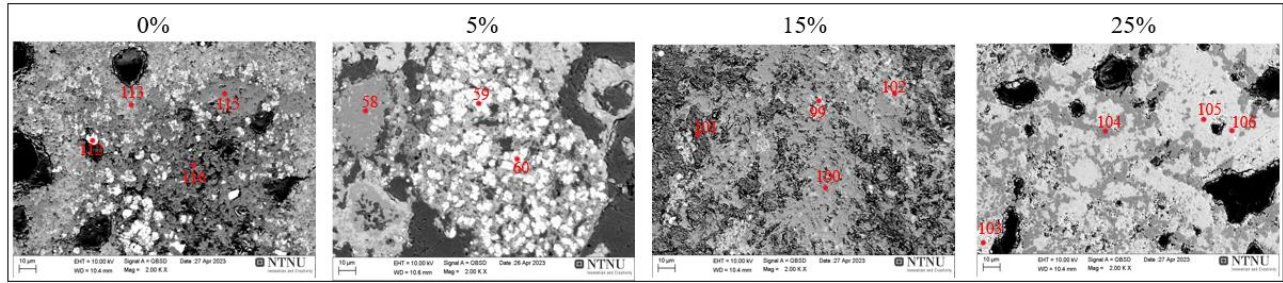
Figure 40: Point analysis spots on the reduced pellets at 800°C with different humidities at 2000x.

4.5.4 EDS – X-Ray mapping, sintered pellets

The X-Ray mapping of elements in the sintered pellets are shown in Figure 41. The area used for the mapping is also illustrated in the figure. The stronger the colour represents a higher amount of a specific element. The darker areas on the X-Ray mapping imitate pores in the sample. The elements being scanned with EDS are Na, Mg, Ca, Ti, Fe, Al, Si and O at 2000x magnification.
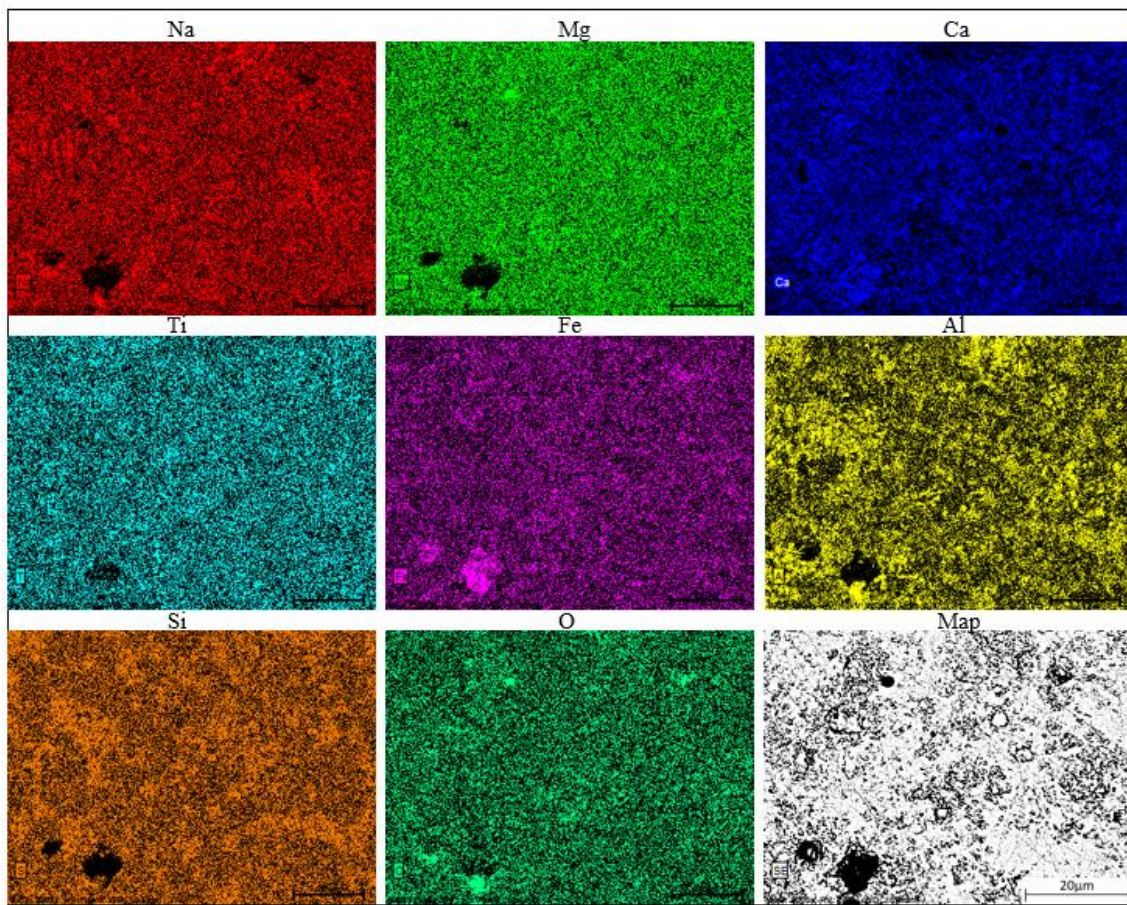
Figure 41: X-Ray mapping results for the sintered pellets at 2000x.

4.5.5 EDS – X-Ray mapping, reduced pellets, 0% humidity, 600°C

The X-Ray mapping on the reduced pellets with 0% humidity is shown in Figure 42. The SEM image of the analysed area used for the mapping is also illustrated in the figure.
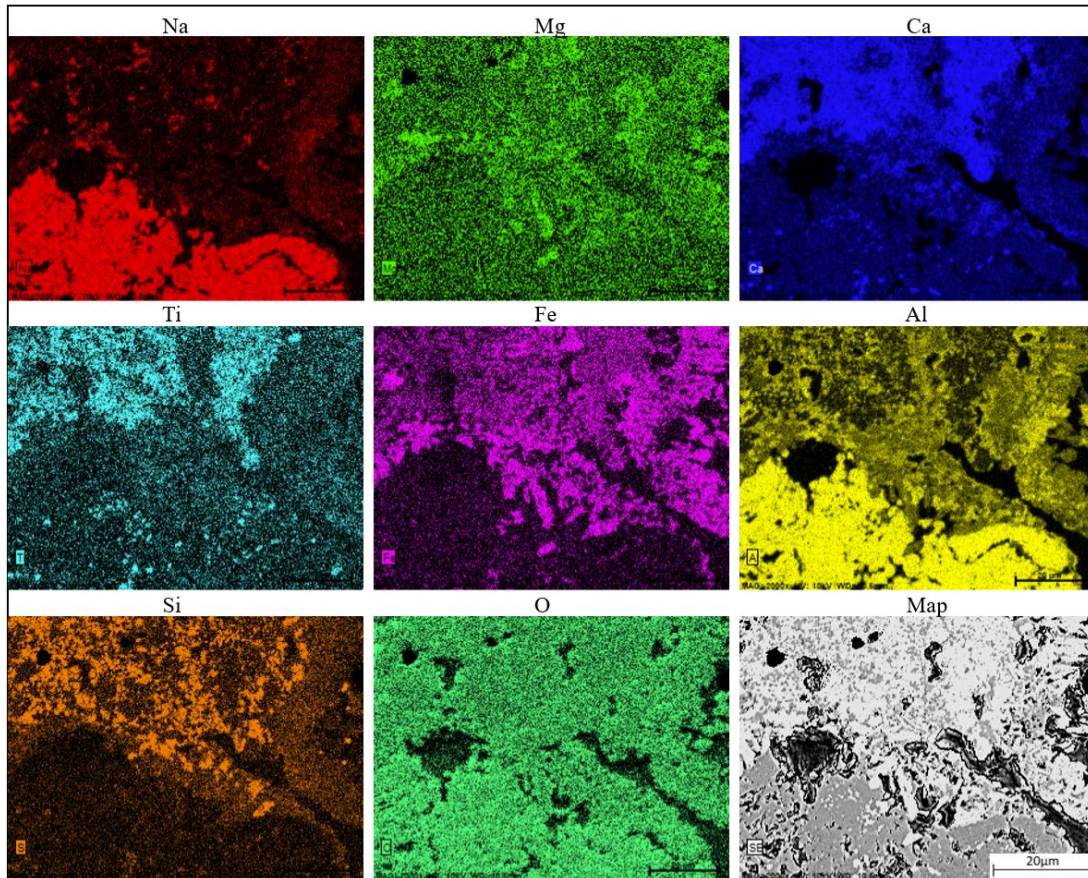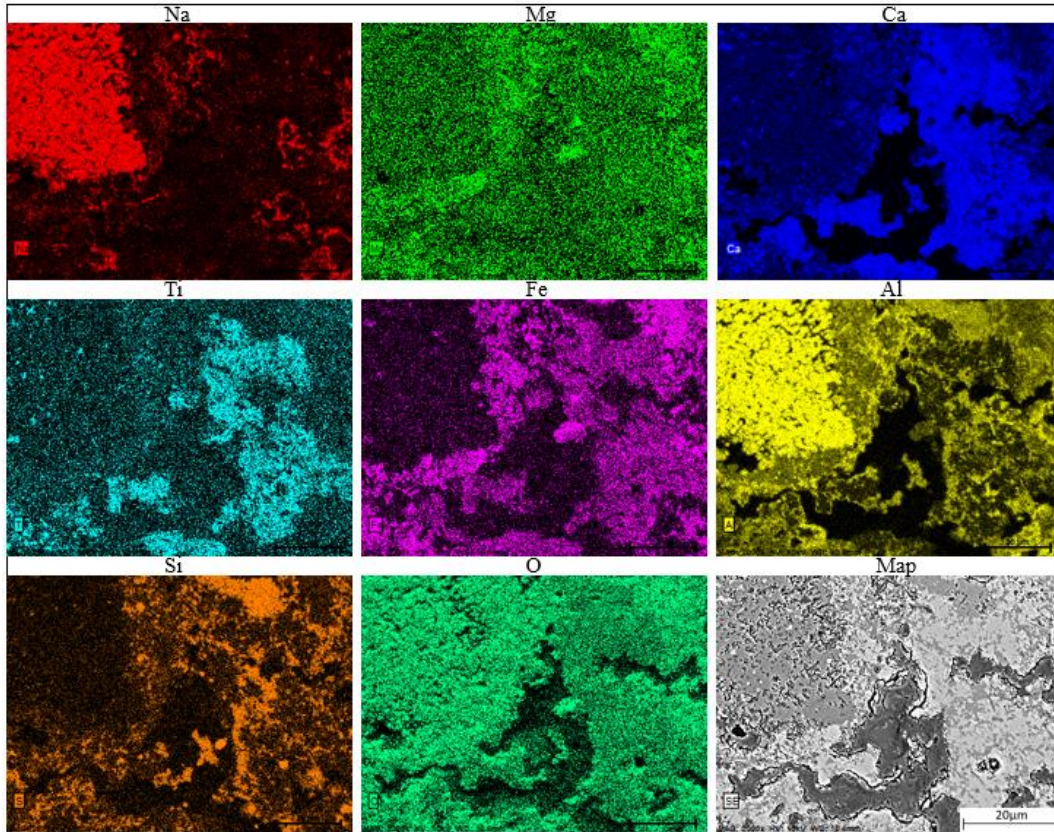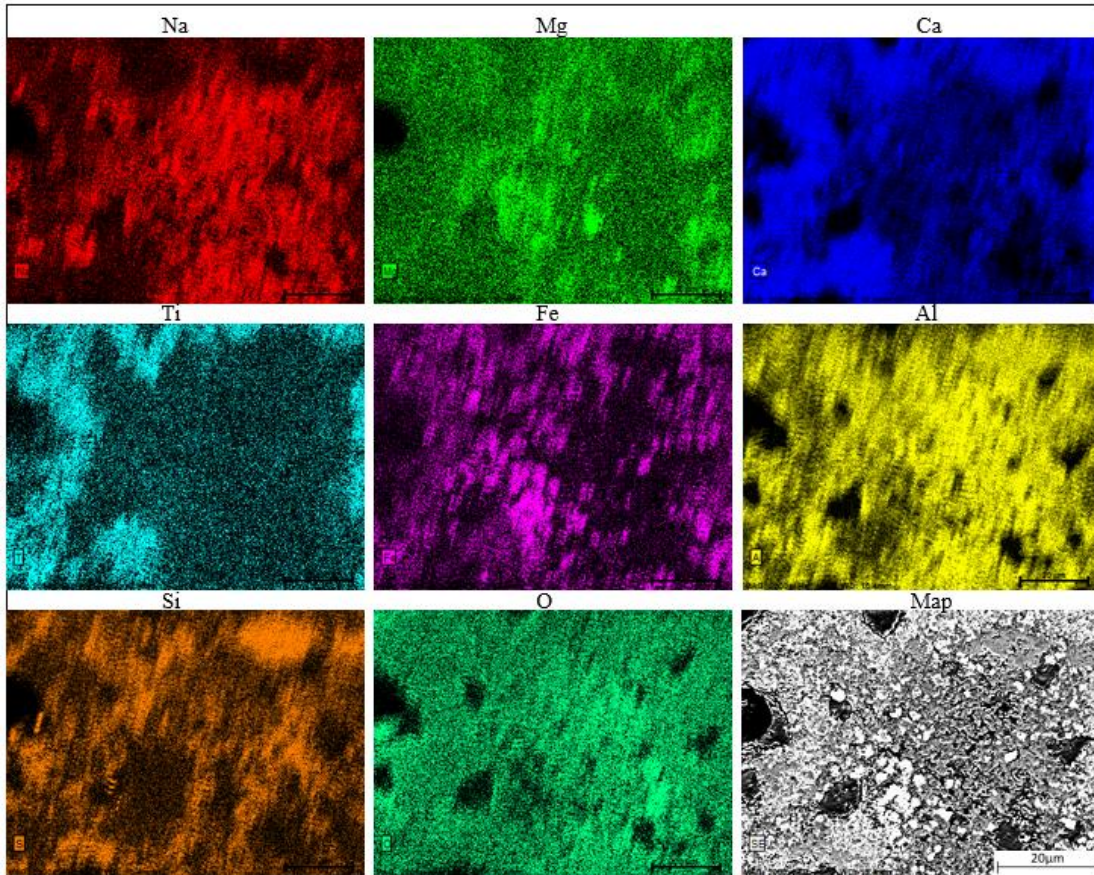

Figure 42: X-Ray mapping results for reduced pellets with 0% humidity and 600°C at 2000x.

4.5.6 EDS – X-Ray mapping, reduced pellets, 5% humidity, 600°C

Figure 43 shows the X-Ray mapping done for the reduced pellets with 5% humidity at 600°C, together with its coherent map area.
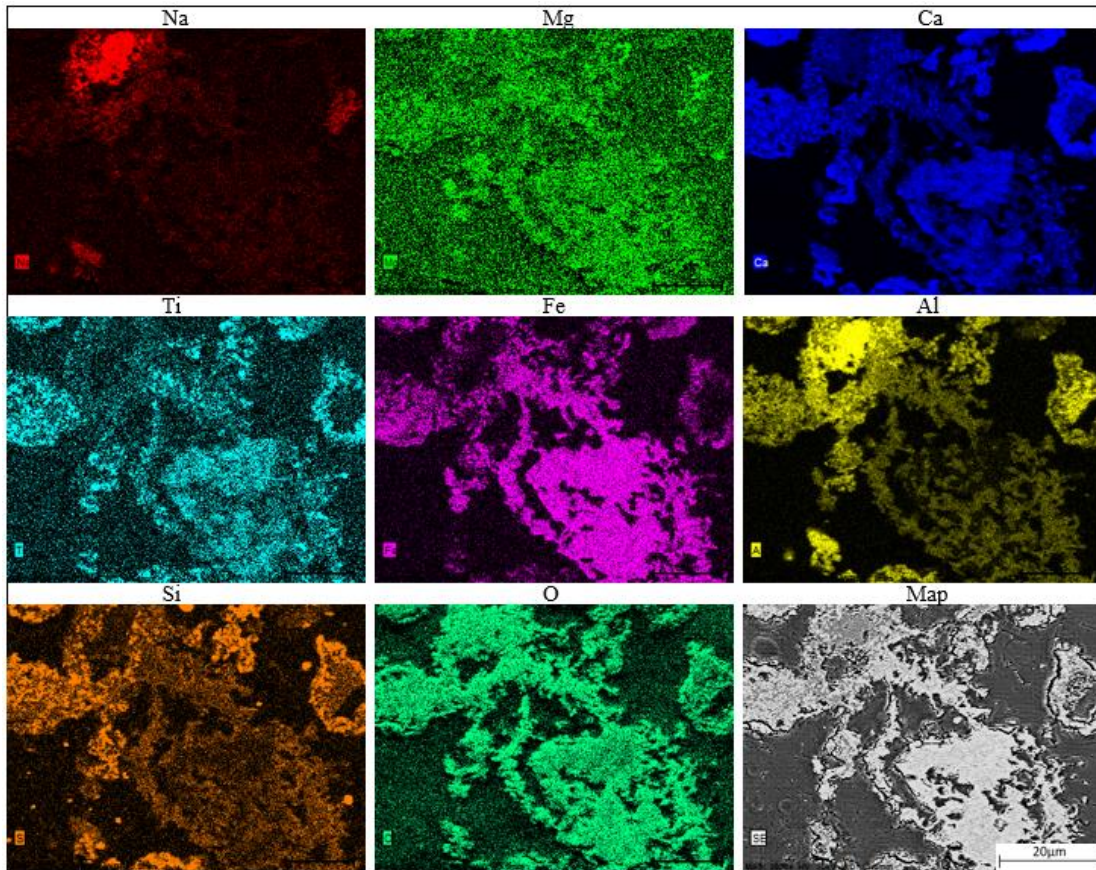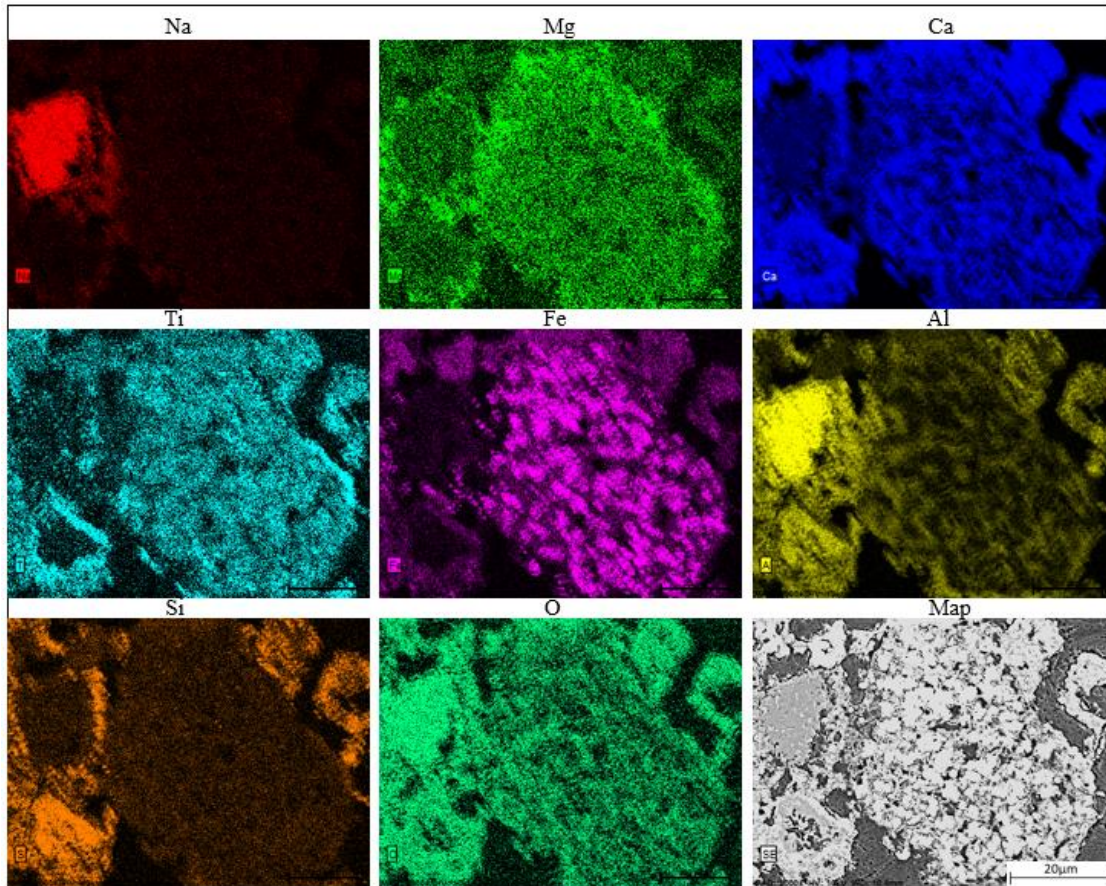

Figure 43: X-Ray mapping results for reduced pellets with 5% humidity at 600°C at 2000x.

4.5.7 EDS – X-Ray mapping, reduced pellets, 15% humidity, 600°C

The X-Ray mapping conducted on the reduced pellets with 15% humidity at 600°C is presented in Figure 44, which includes a coherent map area for reference.
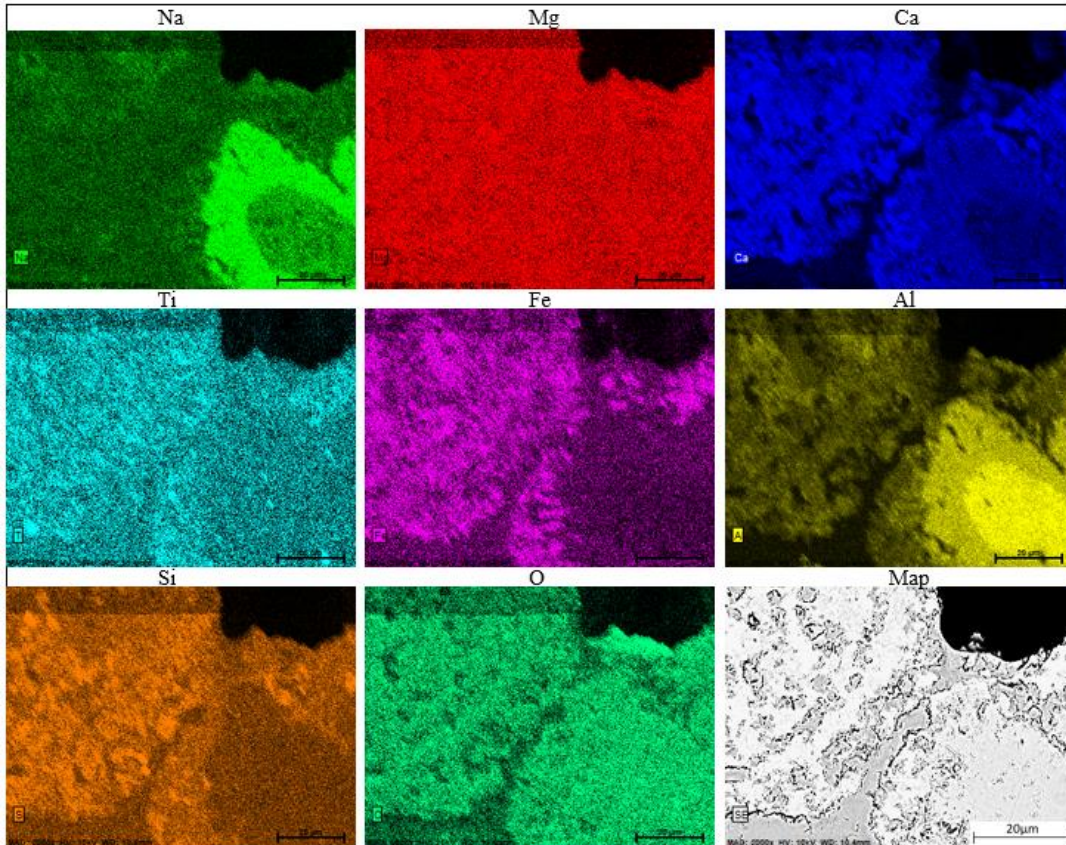
Figure 44: X-Ray mapping results for reduced pellets with 15% humidity and 600°C at 2000x.

4.5.8 EDS – X-Ray mapping, reduced pellets, 25% humidity, 600°C

The EDS analysis for the reduced pellets with 25% humidity at 600°C are presented in Figure 45, together with its coherent map area.
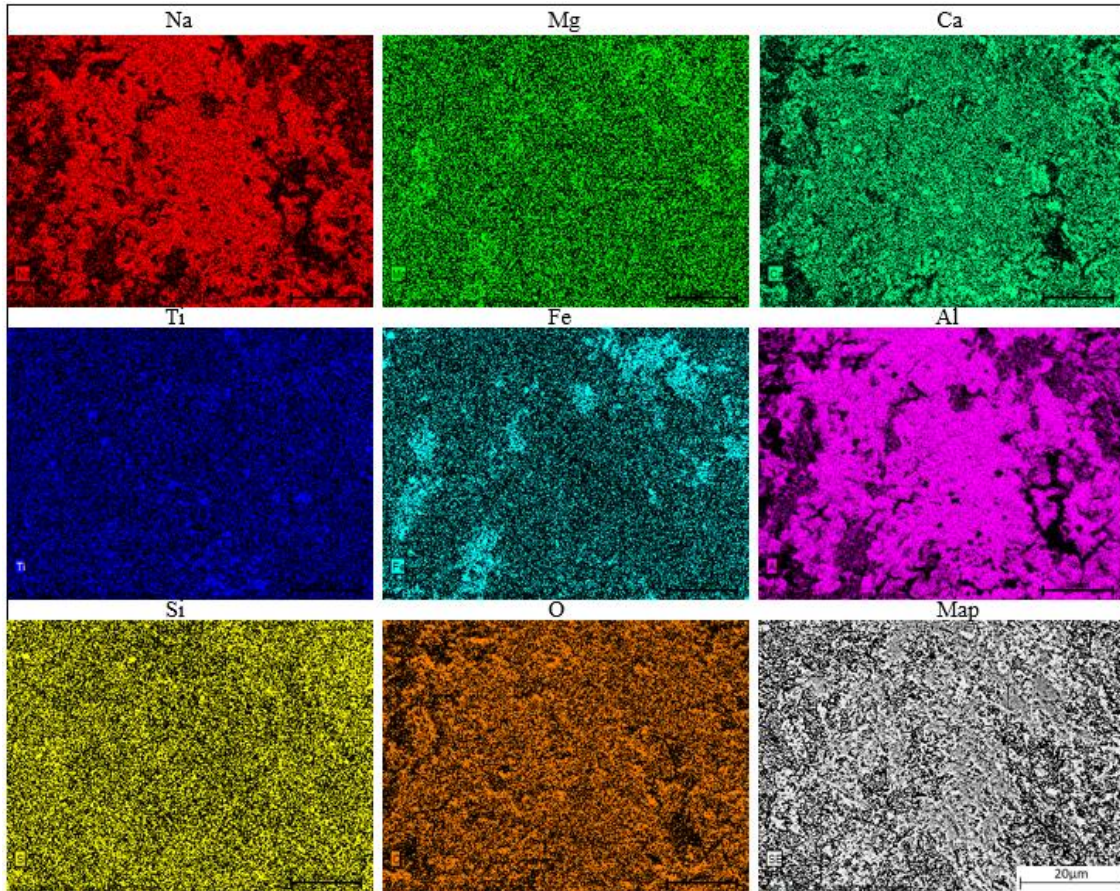

Figure 45: X-Ray mapping results for reduced pellets with 25% humidity at 600°C at 2000x.

4.5.9 EDS – X-Ray mapping, reduced pellets, 0% humidity, 800°C

Figure 46 illustrates the X-Ray mapping results obtained for the reduced pellets with 0% humidity at 800°C, along with a coherent map are to aid interpretation.

Figure 46: X-Ray mapping results for reduced pellets with 0% humidity and 800°C at 2000x.

4.5.10 EDS – X-Ray mapping, reduced pellets, 5% humidity, 800°C

In Figure 47, the X-Ray mapping analysis performed on reduced pellets with 5% humidity at 800°C is displayed, alongside its coherent map area, to provide a visual representation of the element's distribution within the sample.

Figure 47: X-Ray mapping results for reduced pellets with 5% humidity and 800°C at 2000x.

4.5.11 EDS – X-Ray mapping, reduced pellets, 15% humidity, 800°C

Figure 48 shows the X-Ray mapping done for the reduced pellets with 15% humidity at 800°C, together with its coherent map area.

Figure 48: X-Ray mapping results for reduced pellets with 15% humidity and 800°C at 2000x.

4.5.12 EDS – X-Ray mapping, reduced pellets, 25% humidity, 800°C

The reduced pellets with 25% humidity at 800°C were subjected to X-Ray mapping analysis, and the resulting data is presented in Figure 49, which features a coherent map area to facilitate interpretation.
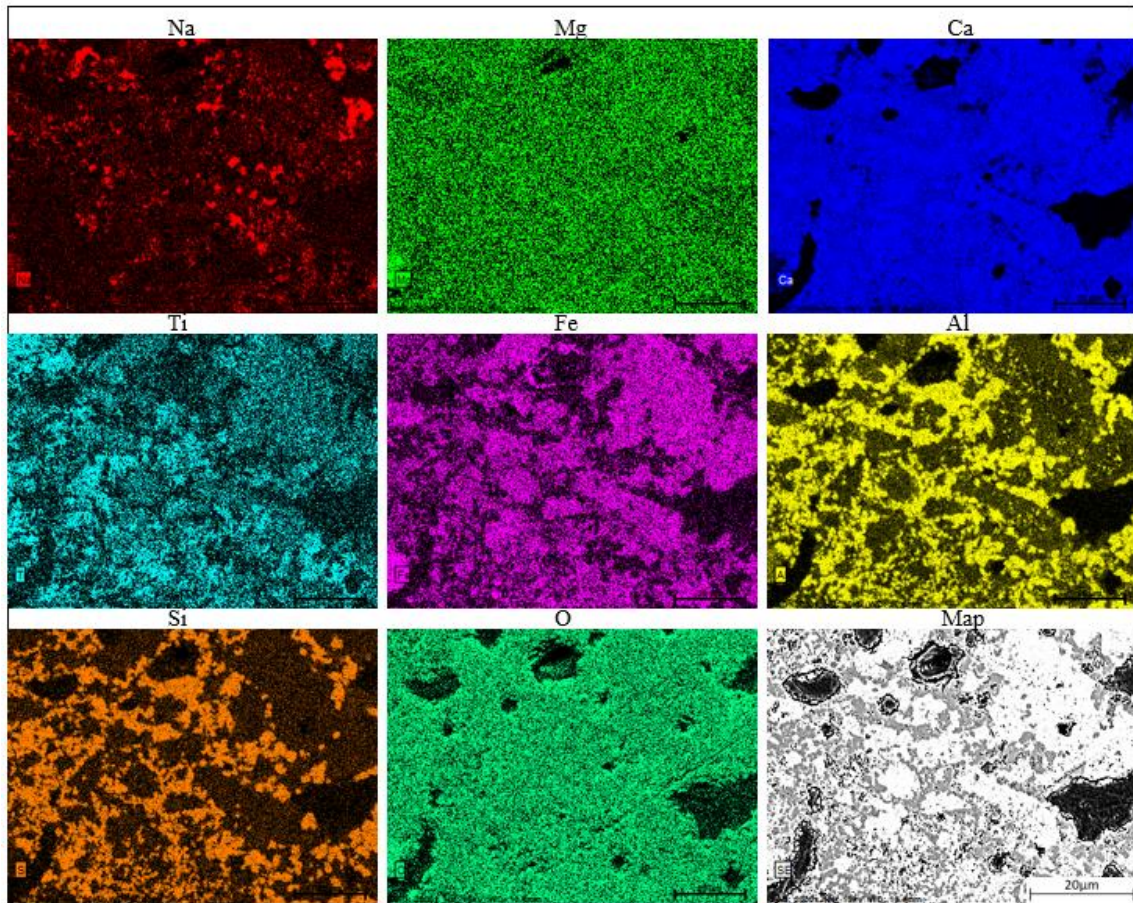
Figure 49: X-Ray mapping results for reduced pellets with 25% humidity and 800°C at 2000x.

4.6 XRD

The XRD analysis gave information about what different compounds were present in the samples. 2-Theta and a WL of 1,54 nm were used during this study. Appendix V presents the raw data of the XRD analysis for all samples.

4.6.1 XRD result sintered pellets

The result for the sintered sample is illustrated in Figure 50.
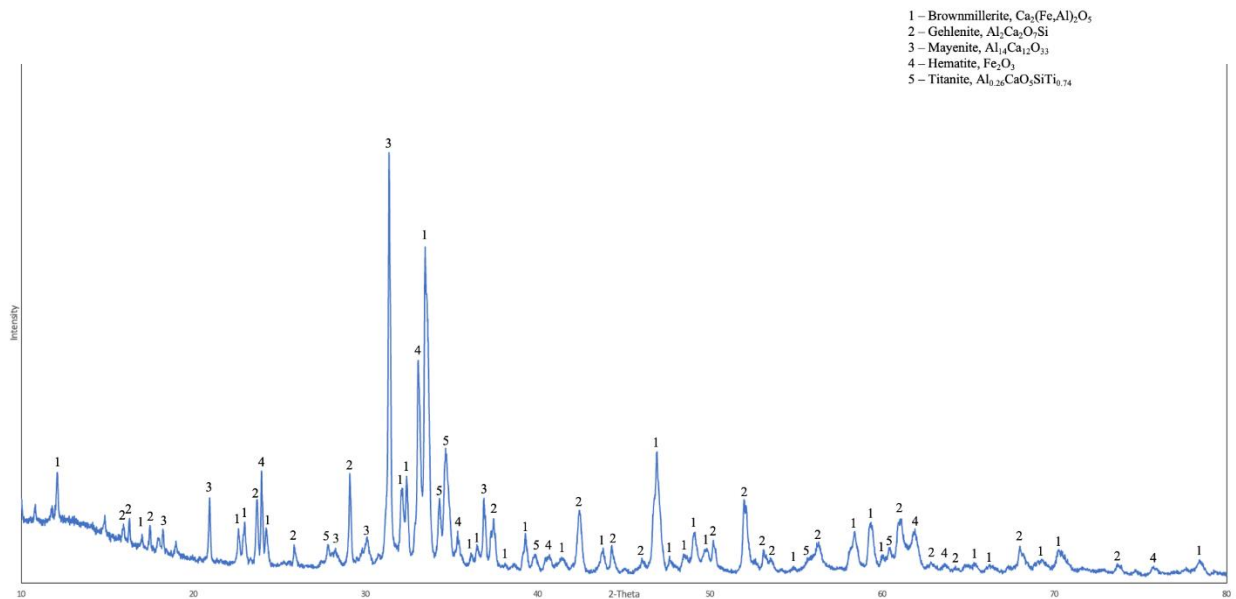
Figure 50: XRD results for the sintered pellets.

The strongest peak represents mayenite, where brownmillerite is the second strongest. There is also some gehlenite, titanite and hematite present in the sintered sample.

4.6.2 XRD results at $600°C$

The XRD was used to study the composition of materials present in the samples. This subsection shows the XRD results obtained using different humidities (0%, 5%, 15% and 25%) at the temperature of 600°C in Figure 51.
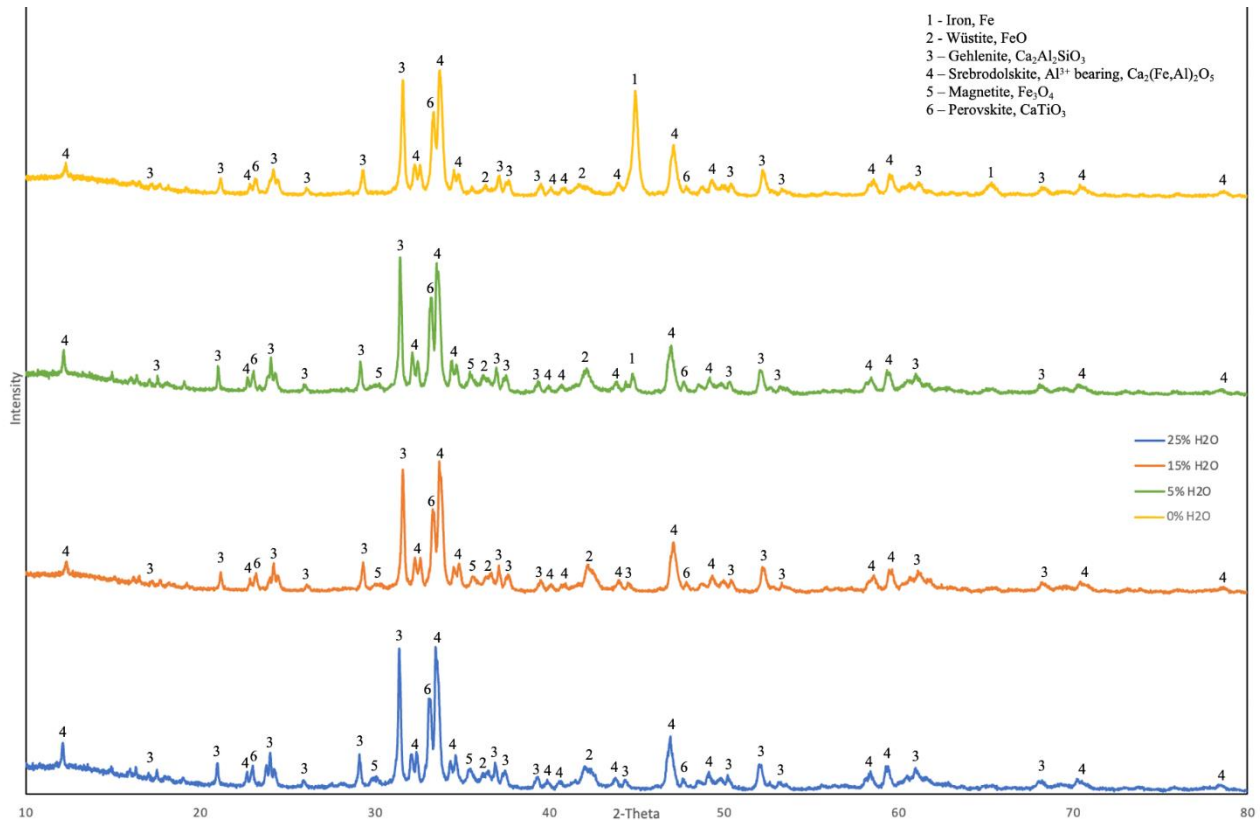
Figure 51: XRD results for the reduced pellets at 600°C using different gas mixtures.

The main difference is that at 0% humidity, iron becomes more abundant. Srebrodolskite is also present in the samples, as well as gehlenite and perovskite. Furthermore, the wüstite peak is less intense than for the rest of the samples. Iron is present in the 5% humidity sample, but not in the 15% and 25% samples. In addition, wüstite becomes more abundant with higher levels of humidity. For all samples containing some level of humidity, magnetite is observed.

4.6.3 XRD results at 800°C

This subsection shows the XRD results obtained from different humidities (0%, 5%, 15% and 25%) at the temperature of 800°C. The results are shown in Figure 52.
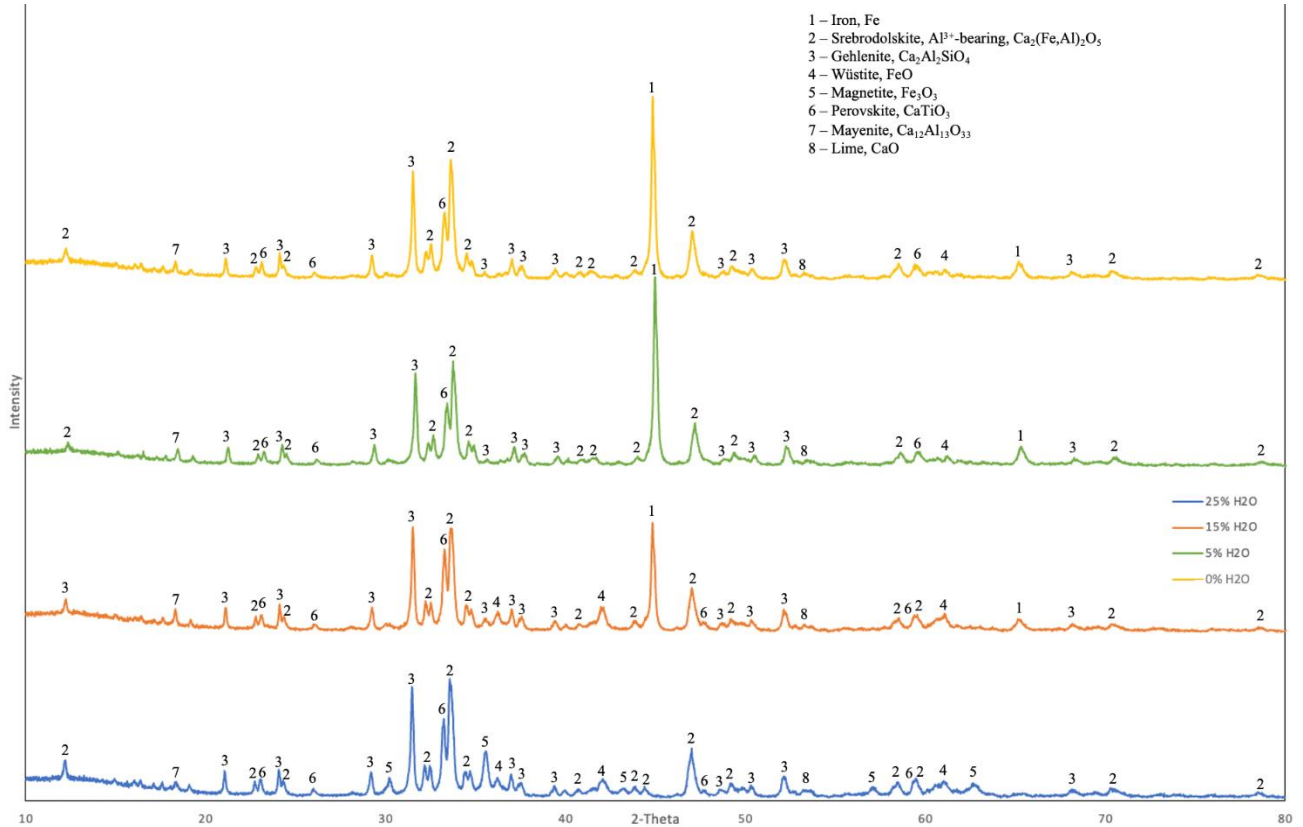

Figure 52: XRD results for the reduced pellets at 800°C using different gas mixtures.

At this temperature, the difference in iron intensity between 0% humidity and 5% humidity is miniscule. The other phases are also coherently similar between these samples. Furthermore, no wüstite is present in these samples. At a humidity level of 15%, the iron intensity of the sample diminishes compared to the previously mentioned sample, with the presence of wüstite. Conversely, at a humidity level of 25%, no iron is observed, and magnetite is detected instead.

4.7 BET & BJH

Figure 53 and 54 presents the outcome of the BET and BJH analyses conducted on the samples. The main focus of the analysis was to determine the surface area and the pore size of each sample. To visualize the results obtained from the analysis, Figure 54 presents a plot of the pore size distribution of each sample, and Figure 53 presents a plot of the surface areas at different humidities. The reduction with pure hydrogen at 600°C yields the largest surface area for the reduced samples, as well as the largest pore size. However, the reduced pellets at 800°C exhibit a larger surface area at 5% and 15% humidity than those reduced at 600°C. In terms of pore size, the 800°C reduced pellets have a smaller pore size across all humidity levels.
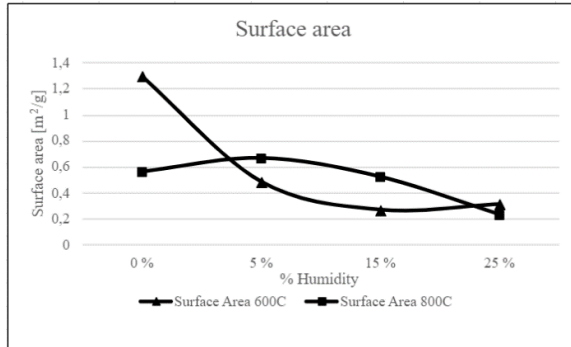
Figure 53: BET results for reduced pellets.
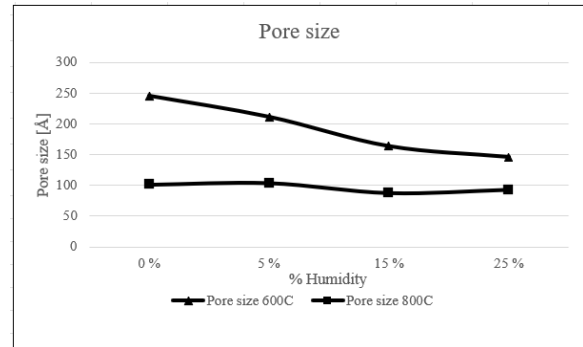
Figure 54: BJH results for reduced pellets.

The samples reduced at 600°C exhibit a consistent trend where the surface area and pore size decrease with increasing humidity, except for a slight increase in surface area observed at 25% humidity. Furthermore, the reduced samples at 800°C show no specific relationship between the humidity and surface area or pore size, seen in Figure 53 and 54. Raw data from the BET and BJH analysis is presented in Appendix VI.

5. Discussion

The discussion section in this thesis have been arranged in chronological order as per the experimental plan, to aid comprehension of the findings. All the reduction experiments were performed with the same duration (2 h) where the only differences were the levels of humidity (0%, 5%, 15% and 25%) and different temperatures (600°C and 800°C).

5.1 Pelletising and sintering

The foundational aspect of this study was the utilization of pelletising and sintering of BR-CaO mixture, which provided the framework for the experimental procedures. The importance of making the pellets to their desired sizes, which were 3-4mm in diameter, and the pellets' ability to not decompose or break during later with the reduction experiments.

Green pellets were subsequently air dried for 24 hours to produce dried pellets and afterwards said green pellets were sintered using a muffle furnace under air atmosphere at 1150°C. Sintering temperature was chosen based on previous research in HARARE project [19].

The sintering of BR-pellets led to a mass loss of approximately 36%, which was expected regarding the decomposition of hydroxides and carbonates. In addition, it is plausible that the liberation of water and volatile constituents, as well as the elimination of impurities, may contribute to this mass loss. Equation 20 describes the mechanism that accounts for the loss of water vapour.

$$Ca(OH)_2 \rightarrow CaO + H_2O_{(g)} \tag{20}$$
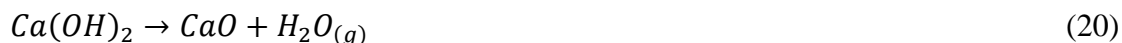
5.2 Reduction extent at different gas mixtures

The main experiment was the reductions of the pellets, where several parameters were considered. Since the furnace had a temperature difference of approximately -35°C between the wall and crucible, the set temperature was set to 635°C and 835°C for each respective experiment. This was done to obtain the desired temperature for the sample holder. The reduction experiment started

when the crucible containing the pellets reached its desired temperature. This led to initiation of hydrogen-water vapour gas to the furnace. By adding H_2-H_2O to the furnace, the temperature increased to some extent, in turn making the temperature in the sample holder about +8°C-12°C above the preferred temperature.

To get an indication whether the reduction experiment went as expected, the samples were weighed before and after. If there had been a mass loss, which coordinates with other experiments to some extent, the reduction was successful. Furthermore, the analytical tools such as XRD, SEM, BET and BJH helped confirm the outcome of the different reduction experiments.

The correlation between the reduction degree and mass loss, indicating that the relationship between these two variables remain consistent regardless of temperature changes. This association is shown in Figure 55. The congruent angles for the plotted lines suggest that further increase in temperature would not affect the established correlation, and instead result in a continuation of the current graph plotted. The R^2-values for both the plotted lines equals 1, meaning a perfect fit of the regression model. This model does also suggest that an increase in temperature would not affect the association between reduction degree and humidity.
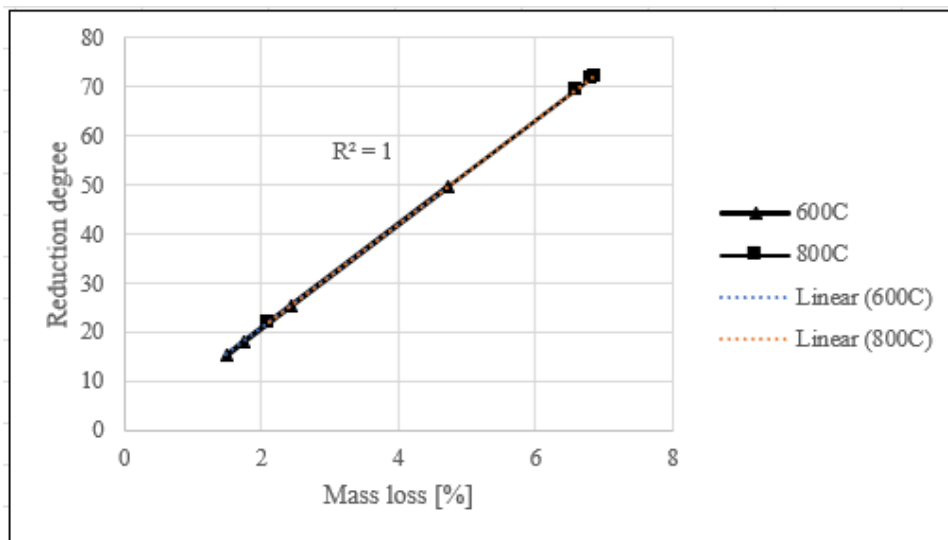

Figure 55: Correlation between reduction degree [%] and mass loss [%].

Figure 56 shows how mass loss changes for different levels of humidity, and after which given point the reduction to metallic iron stops. The general trend is the more humid the reducing gas is, the less mass loss occurs for a given temperature. The plot depicting the mass loss percentage of reduced pellets at 600°C indicates a decreasing trend as the humidity level increases. At 800°C, there is only a slight decrease up to 15% humidity, where a drastic decrease occurs when a humidity level of 25% is used. For this graph, the R^2-values are 0,9901 and 0,9491 for the temperature 600°C and 800°C, respectively. This meaning that further experiments at 600°C are easily predictable when increasing the humidity, than it would have been at 800°C. Both Figure 55 and 56 visualise that at 600°C, the R^2-value is higher than it is for 800°C. This suggests that predictions about further change in mass loss with relation to humidity can be more easily made.
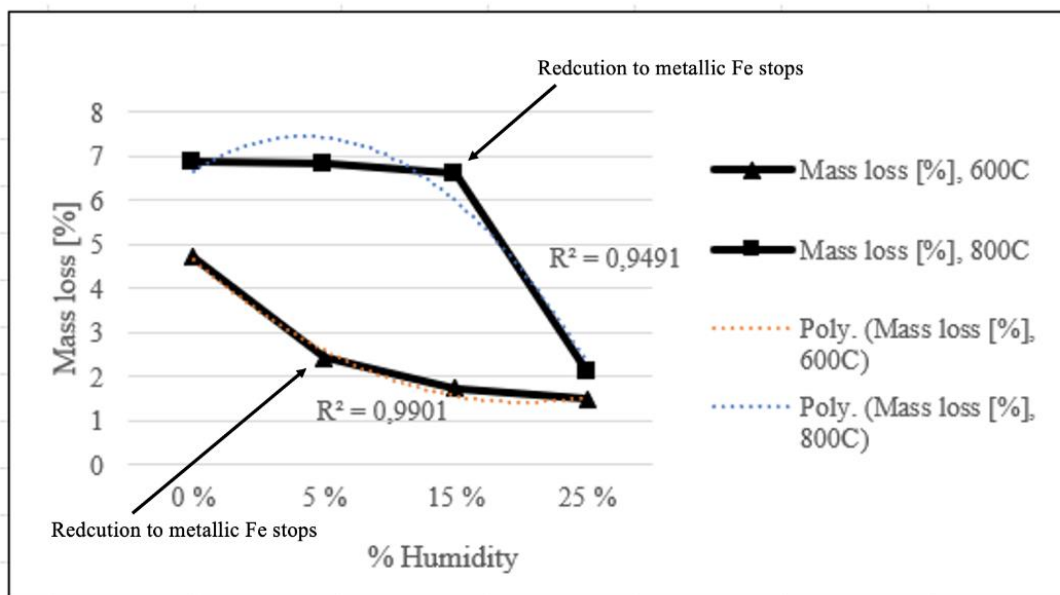
Figure 56: Correlation between mass loss [%] and H_2O levels [%], and after which point reduction to metallic Fe stops.

In the experiment setting where a humidity level of 15% was maintained at a temperature of 600°C, the removal of the sample from the oven resulted in the observation of moisture accumulation in colder regions. This led to the experiment being completely redone with improving the set-up to take away all water vapour after interaction of gas with the sample, as to ensure no errors occurred.

During the redoing of the experiment, a detachment of the crucible from the sample-holder stick occurred while attempting to extract the sample. This also led to the experiment being redone. However, once this was complete, it was observed no significant differences in reduction degree between the first redoing and the second, implying that detachment of the crucible does not matter during reduction.

The experiment with 25% humidity at 800°C showed a significantly lower reduction degree than all the other experiments done at the same temperature, with a reduction degree of only 22,20%. As no extraordinary deviations happened during these experiments, the consensus is that at high levels of humidity, the reduction of iron oxides in the pellets are greatly inhibited. This could be explained by H_2O molecules inhibiting free-reaction sites on the pellets, making further reduction closer to the core of the samples even more difficult. The H_2-gas is not able to diffuse through the particles, in turn making diffusion the rate-limiting step. This is also in line with what has been observed by previous research [25]. The interesting part, however, is that for humidity-levels at both 5% and 15% at 800°C, when compared to 0%, the reduction degree becomes almost negligible. Moreover, these differences were greater at 600°C, where the reduction degree for the humidity levels 0%, 5%, 15% and 25% respectively were 49,64%, 25,56%, 18,22% and 15,68%. This implies that temperature plays a big role when conducting reduction experiments.

5.3 Characterisation

During the characterisation process of the samples, each specimen underwent individual preparations that had the potential to introduce human errors. This could thereby lead to outcomes that were not favourable. The following subsections are arranged in the same sequence as the results section.

5.3.1 XRF

Since the XRF analysis were done by third-parties, Degerfors Labs and Sintef Norlabs, discussions are limited. However, the results from Table 7 and 8 are in-line with the typical composition of BR, shown in Table 1. The only significant change in composition is more amounts of CaO in the sintered pellets, due to addition of $Ca(OH)_2$.

5.3.2 SEM and EDS

In order to conduct the SEM analysis, it was necessary to coat the samples with a conductive material. For this study, gold was used as a coating material. This was required as an electron beam is utilized to scan the surface area, generating an electric charge. The sintered pellets had 90 seconds of coating, while the rest were coated for 30 seconds. This resulted in a poorer X-Ray mapping with EDS and point analysis, as gold covered all the other phases in the sintered pellets. This can be seen especially in Figure 41, where all the elements do not have their distinct areas, compared to other X-Ray mapping. Mentioned in Chapter 2.7.2, the coating does also work as a protection layer, since the electron beam can degrade the sample that is being observed.

When looking at the SEM images in Figures 29-37, there are some correlations between the effects of temperature and humidity when observing pore size and visible phases. Firstly, the reduced pellets at 600°C have an increasing amount of pore and pore size with less humidity, indicating more reduction of the sample. The opposite occurs for the reduced pellets at 800°C, and this may be due to the partial sintering of particles in the samples at this higher temperature. Furthermore, the phase distinction is easier to spot when decreasing the humidity. The samples at 25% humidity have a more monotone grey colour, compared to the samples at 0% humidity.

5.3.2.1 Point analysis

Point analysis was used to determine different phases and compositions present in the samples, that would later be confirmed by XRD-analysis. Interesting points at 2000x, showing different phases, was each analysed by EDS-point analysis. The dominant phases observed in the sintered sample are estimated to be brownmillerite and gehlenite. Point 121 suggests the potential presence of hematite, seen in Figure 38 and Table 10. This might be due to low amounts of aluminium. Furthermore, the phases in the sintered sample seems to be more merged together with each other, making it challenging to spot distinct phases.

For the samples reduced at 600°C at different levels of humidity, the phases become more distinct from each other, as opposed to the sintered sample. Here, more clear phases of iron can be observed in Figure 39, and the main phases are estimated to be metallic iron, wüstite, srebrodolskite, gehlenite and sodium calcium aluminium oxide. Based on the chemical composition indicated by at%, point 56 in Table 11, which represents a point in the sample at 25% humidity at 600°C, is

estimated to be brownmillerite. This may indicate that at this level of humidity, the brownmillerite phase may not reduce completely.

The main phases in the samples reduced at 800°C shows even more distinct phases than the samples reduced at 600°C. This is also seen with point analysis, as higher percentages of iron are detected at some points of interest. For instance, point 112 in Table 12, contains 95,65% iron, clearly indicating that metallic iron is present. The metallic iron is further evidenced by its distinctive bright white colour seen from Figure 40. Other phases estimated are srebrodolskite, gehlenite, mayenite, perovskite and wüstite.

To get a better understanding of what phases and compounds are present in the samples, the XRD-results needs to be discussed together with the point analysis. Chapter 5.3.3 discusses the results obtained from the XRD-analysis.

5.3.2.2 X-Ray mapping

What this study focuses on is the positioning of iron and oxygen, and where they overlap each other. Inspecting the sintered pellets' X-Ray mapping, the pore spotted in the bottom left in Figure 41 is both rich in iron and oxygen. The phase that might be present in this area is hematite (Fe_2O_3) or brownmillerite ($Ca_2(Fe,Al)_2O_5$). Furthermore, the elements are scattered everywhere, meaning there is no distinct phases seen from the mapping. Also, it must be considered that the X-Ray mapping is a relative measurement.

The reduced pellets at 600°C does all have oxygen present together with iron across all the humidities. This is due to the temperature, since it is too low for iron oxides to be reduced to metallic iron. It is seen from the XRD results in Figure 51, that there might be some pure iron product when reduced with pure hydrogen. This was also found in a previous experiment [21]. Otherwise, the main phase found in these samples is Al^{3+}-bearing srebrodolskite ($Ca_2(Fe,Al)_2O_5$).

Elevating the temperature to 800°C has a more pronounced difference, considering metallic iron is desired to be found. Distinct regions exhibiting iron-rich and relatively oxygen-poor features can be identified using the humidity levels 0%, 5% and 15%, presented in Figures 46, 47 and 48. This implies that metallic iron is present in the sample. The amount of iron increases with decreasing humidity, meaning the reduction with pure hydrogen produces the most metallic iron.

The X-Ray mapping for the 800°C with pure hydrogen and 5% humidity, seen in Figure 46 and 47, displays more indistinct images than other samples. This can be due to vibrations or inadvertent contact to the instrument. For further investigation of the different phases, XRD analysis is utilised to assist the assumptions of which phases were present in the analysed samples.

5.3.3 XRD

When analysing using XRD, a back-loader sample holder was used for all the samples. The back-loader is the best choice for a quantitative analysis and is also beneficial when there is a limited amount of powder being analysed. All the samples, except for the sintered one, was milled in a ring mill at 700 rpm for 3 minutes, making the powder fine enough for XRD-analysis. The reason the sintered sample was not milled was due to the ring mill being removed from the lab, so the sample was instead thoroughly crushed with a mortar. How this affected the results is difficult to say, as the XRD-result from the sintered sample came out as expected. Furthermore, when preparing the powder for XRD analysis, the powder needs to be flat on the sample holder with little to no cracks. This was carefully considered when doing the analysis.

When observing the different phases at 600°C in Figure 51, the formation of iron exclusively observed solely under 0% and 5% humidity conditions, with a significantly diminished presence in the sample characterised by 5% humidity. Moreover, wüstite is present in all the samples, becoming increasingly more abundant the more humidity present in the reducing gas. Including wüstite in the samples with 5%, 15% and 25% humidity level, magnetite is also present, which is not the case for the sample with 0% humidity. Metallic iron, wüstite and magnetite are all present in the 5% humidity sample. This shows that with these conditions, the H_2/H_2O ratio is close to equilibrium.

For the experiments done at 800°C, the XRD results for the 25% humidity sample showed minimal iron peaks, presented in Figure 52. The iron peaks observed in the remaining humidity levels conducted at this temperature exhibits the highest intensity within each coherent graph, indicating their prominent presence. Moreover, sample with humidity level 25% at 800°C is the only sample to show a magnetite peak at this temperature, indicating some inhibition for wüstite formation. Also, when comparing the different graphs, the wüstite peaks are weaker at 25% humidity than for the rest. This raises a point: when the humidity reaches a certain level of humidity between 15%

and 25%, formation of metallic iron is inhibited. This also correlates with the low reduction degree that was calculated for these samples, and discussions regarding this are done in Chapter 5.2. It is also seen from the XRD results, that changes in peak ratio only occurs for the iron-containing phases. Therefore, it is a reasonable assumption that only oxides containing iron has been reduced.

From Table 3 and 4, the Gibbs' free energy for each phase at its coherent temperature is presented. The tables provide a visual representation of higher Gibbs' free energy values associated with the formation of wüstite from magnetite at 600°C compared to 800°C. Moreover, the formation from magnetite to wüstite occurs spontaneously at 800°C and not with a temperature of 600°C. This could explain why there are more magnetite present at 600°C samples than in the 800°C samples. Furthermore, the presence of magnetite is solely detected in certain samples, specifically those with the humidity levels 5%, 15%, 25% at 600°C, seen from Figure 51. At 800°C, magnetite is only detected in the sample with 25% humidity. The observation indicates that the humidity plays a role in preventing further wüstite formation. The reason for this could be that when more water is present, the Gibbs' free energy becomes higher. This is making the transformation from magnetite to wüstite less spontaneous than for using pure H_2-gas, in turn inhibiting more wüstite-formation than the amount exists. Seen from the Ellingham diagram in Figure 10, metallic iron formation proceeds beyond these values for H_2/H_2O compositions:

$$600°C: \frac{H_2}{H_2O} > 7$$

$$800°C: \frac{H_2}{H_2O} > 5$$

With only the metallic iron phases present observed at the humidity levels 0% and 5% at 600°C, the H_2/H_2O ratio for these samples slightly exceeds the established numerical values with possible deviations, as wüstite was still identified in these samples. The opposite is true for the other samples at 600°C.

Concerning the samples at 800°C, the samples with 0%, 5% and 15% humidity have exceeded the established values, which is due to identification of metallic iron. This is not the case for the 25% humidity sample, as no metallic iron was identified. According to the Baur-Glassner diagram shown in Figure 6, the more water present makes the wüstite phase more stable, which explains why more wüstite is present with more humidity.

High intensity peaks for srebrodolskite are found in all samples except the sintered one. Brownmillerite, which was found in the sintered sample, is not observed for the other samples. This is somewhat unexpected, as previous studies has shown peaks of brownmillerite after reduction. Given that magnetite is observed in some of the samples containing humidity, the most probable outcome is that brownmillerite has been reduced to magnetite. For comparison, none of the previous studies show magnetite peaks after reduction [21][26]. Since srebrodolskite is identified in all samples, and it being Al^{3+}-bearing, it is likely that these phases are the same. This is due to similarities between the chemical compositions, and srebrodolskite being within the same areas where brownmillerite was identified in the sintered sample. This means that only the compositions have changed, not the amounts. As wüstite is present in all samples except for the humidity levels 0% and 5% samples at 800°C, the three-stage mechanism shown in Equations 10 and 11 has occurred. This implies that humidity does not affect this aspect of the kinetics. Therefore, temperature is the prominent parameter [25].

When comparing XRD and EDS point analysis results together, most phases estimated corresponds to the findings in XRD. The primary distinctions lie in the XRD analysis, where higher peaks of perovskite are detected in all samples except the sintered sample. In contrast, only point 59 from the sample with 5% humidity at 800°C in Table 12 estimated presence of perovskite, where it was possibly mixed in with srebrodolskite. Also, mayenite is estimated to be present at 800°C in point 116 and point 58 in the samples with 0% and 5% humidity, respectively, presented in Table 12. However, the XRD analysis also indicates the presence of mayenite in the 15% and 25% humidity samples, which is not estimated in EDS for these samples. This demonstrates the importance of doing both analytical methods, as to verify what the different phases are, and to find possible deviations.

5.3.4 BET and BJH

The information obtained from BET and BJH analysis are the samples surface area and pore sizes. By comparing the surface areas measured at different humidity levels, it is clear to say that by increasing the amount of water vapour in the gas, the smaller the surface area. Figure 53 visualises the influence of water vapour at the two set temperatures. It resulted in a contradicting relationship between water vapour and temperature. The largest surface area was found in the reduced samples

at 600°C for 0% humidity, which then decreased at 5% and 15% humidity. At 25% humidity, there was a slight increase in surface area from the sample at 15% humidity. The complete opposite was found for the reduced pellets at 800°C. This relationship was also non-linear, which can be connected to a previous study, presented in Figure 14 [21]. Figure 57 displays the correlation between surface area and the mass loss at both temperatures, revealing a positive relationship wherein an increase in mass loss is accompanied by an increase in surface area. The plotted lines have both an R^2-value close to 1, which entails further experiments to be somewhat linear with the already plotted graph.
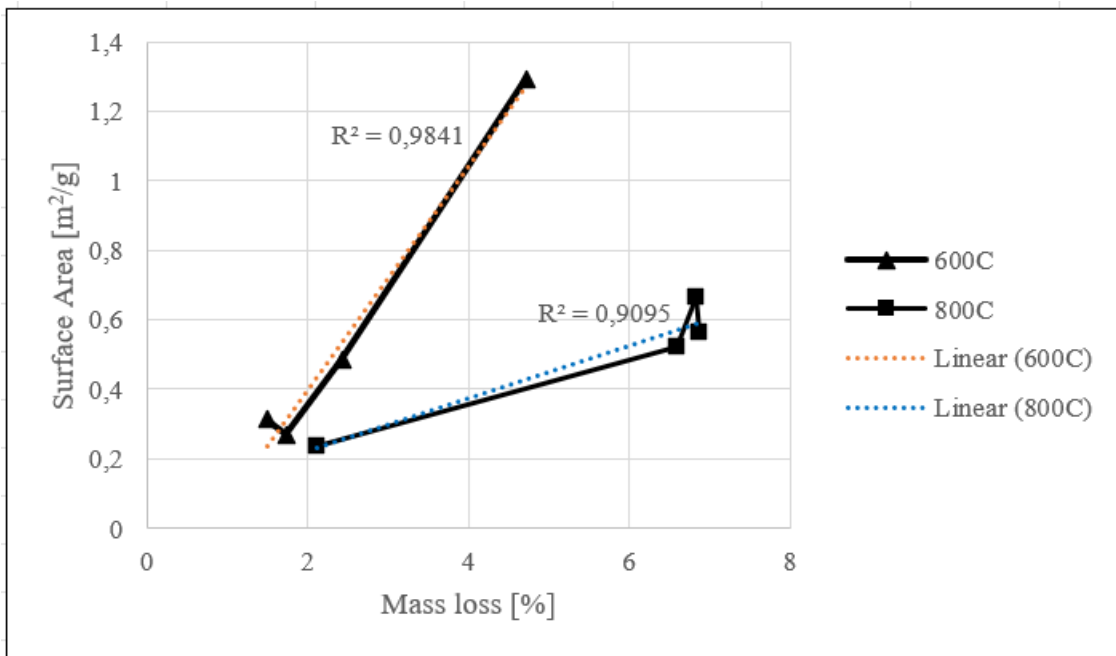
Figure 57: Correlation between surface area [m²/g] and mass loss [%].

Unlike surface area, the pore size shows a linear relationship between temperature and water vapour, seen in Figure 54. When increasing the humidity, the pores seem to shrink and be less prevalent, especially for the reduced samples at 600°C. Furthermore, for these samples, the pore size seems to get larger when the reduction degree increases. This includes the porosity as well. Since higher amount of oxygen is leaving the sample, leading to larger surface area. As for the 800°C samples, the same trend appears, except for the sample with 0% humidity. Even though it has the highest reduction degree, it got a lower surface area and pore size than the sample with 5%

humidity. It was expected a higher porosity for the 800°C samples due to larger extent of reduction, however, some sintering of particles occurred which causes porosity loss and lower surface area.

In the context of BET and BJH, there is a limiting amount that can lead to sources of errors. When it comes to humanly errors, imprecise measurements when preparing the sample can affect the surface area and pore size calculations. When considering the program used, the main thing that can lead to an invalid result is deviations from the ideal gas behaviour, since this can lead to inaccurate calculations regarding the adsorption. Furthermore, if the degassing is incomplete, it can lead to an overestimation of the surface area. This is because gas or water molecules may still be present in the sample if not degassed properly.

5.3.4.1 Comparison of SEM and BJH results

According to the obtained BJH results, the general trend is that the average pore size seems to shrink. This is clear when looking at the SEM images for 600°C, as the dark spaces between each phase are greater the less humidity present. However, it is less clear for the samples at 800°C, and this is supported by both SEM imaging and BJH analysis. Porosity differences are shown in Figure 58 and 59 at a magnification of 200x for 600°C and 800°C, respectively.
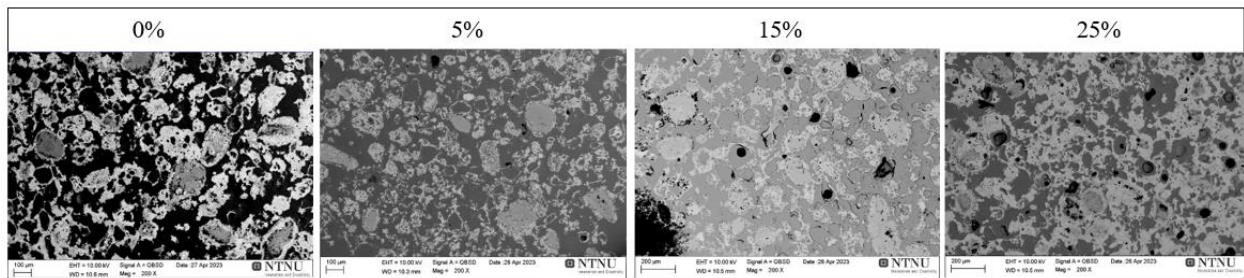
Figure 58: SEM imaging of reduced pellets at 200x for 600°C with 0%, 5%, 15% and 25% humidity.
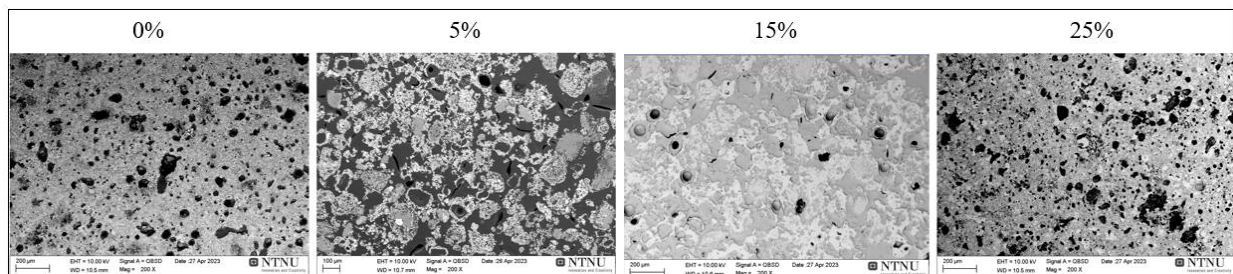
Figure 59: SEM imaging of reduced pellets at 200x for 600°C with 0%, 5%, 15% and 25% humidity.

Changes in porosity is due to partial sintering of particles in the pores. When applying heat during reduction, some particles may merge. This leads to the pores either being completely or partially covered, decreasing the calculated average pore size in the samples. Figure 60 illustrates how partial sintering affects the pores in the samples.

Before reduction   After reduction
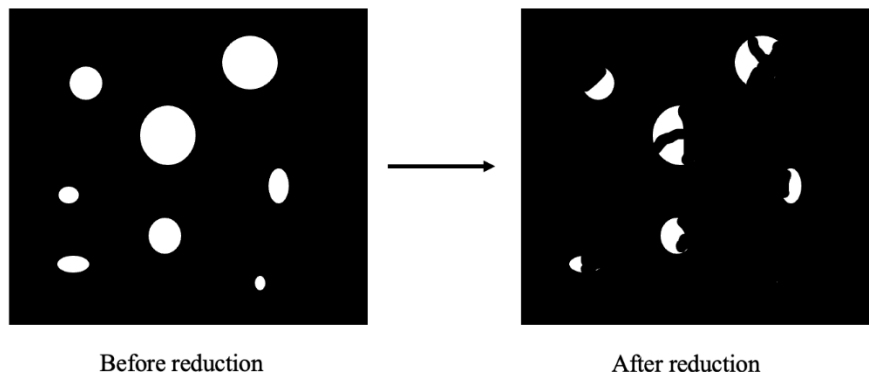
Figure 60: Effects of partial sintering in the sample.

The change in porosity for the 800°C samples are minor compared to the 600°C samples according to BJH. This can be confirmed with the use of SEM imaging. Furthermore, the phases seen from SEM imaging for the 600°C samples become more merged together when more humidity is present, compared to the 800°C samples. The pores in the 800°C samples seem to be somewhat alike to one another across all the levels of humidity, making it hard to spot porosity differences using only SEM imaging. Additionally, the average pore size is smaller at 800°C compared to 600°C, indicating a greater extent of partial sintering at the higher temperature.

6. Conclusions

In this thesis, the effects of H_2-H_2O mixtures on the reducibility of BR were studied. The following conclusions, based on results and discussion, has been made:

- At 600°C, the 5% humidity sample is close to equilibrium conditions. This is because of metallic iron, wüstite and magnetite all being present at the same time.

- At some point between a humidity level of 15% and 25% during reduction at 800°C, reduction of iron oxides stops because of thermodynamic conditions. Already formed wüstite becomes more stable and wüstite reduction to metallic iron is greatly inhibited. This means that the equilibrium for H_2/H_2O lies within this range at this given temperature.

- The experiment that yielded the highest reduction degree was at 800°C and 0% humidity, with 72,26%, demonstrating that H_2O-gas in the reducing gas inhibits the H_2-gas' ability to diffuse, making diffusion the rate limiting step.

- At lower temperatures of 600°C, small amounts of humidity greatly diminish the reducibility of brownmillerite.

- At higher temperatures of 800°C, small levels of humidity give a negligible difference in reduction degree, showing that temperature is the most important factor regarding reaction kinetics.

- Changes in mass loss and reduction degree regarding varying levels of humidity are easier to predict at lower temperatures of 600°C than for higher temperatures of 800°C. This can be seen from the calculated R^2-values being closer to 1 for 600°C than for 800°C.

- Reaction mechanism is unaffected by the humidity levels used, as all the reactions follows the three-stage mechanism for all samples. This is clear because of wüstite formation shown by XRD and EDS analysis.

- The surface areas for the reduced pellets at 600°C decreased with increasing humidity, except at 25%, where the surface area got a slight increase. The opposite was observed for the 800°C pellets.

- Average pore size decreased by increasing the temperature from 600°C to 800°C. Correlation between humidity and pore size had a decreasing trend. This is due to partial sintering in the samples during reduction.

7. Recommendations for further work

For further investigation of this study, it is recommended to increase the temperature to at least 1000°C, with different levels of humidity. Testing with humidity levels between 15% and 25%, to see whether this inhibits reduction at higher temperatures, and to determine exactly at what humidity level reduction to metallic iron stops.

References

[1] A. Lazou, C. Van Der Eijk, K. Tang, E. Balomenos, L. Kolbeinsen, and J. Safarian, 'The Utilization of Bauxite Residue with a Calcite-Rich Bauxite Ore in the Pedersen Process for Iron and Alumina Extraction', *Metall. Mater. Trans. B*, vol. 52, no. 3, pp. 1255–1266, Jun. 2021, doi: 10.1007/s11663-021-02086-w.

[2] R. K. PARAMGURU, P. C. RATH, and V. N. MISRA, 'TRENDS IN RED MUD UTILIZATION – A REVIEW', *Miner. Process. Extr. Met. Rev*, Aug. 2006, doi: 10.1080/08827500490477603.

[3] M. Archambo and S. K. Kawatra, 'Red Mud: Fundamentals and New Avenues for Utilization', *Miner. Process. Extr. Metall. Rev.*, Jun. 2020, Accessed: Feb. 26, 2023. [Online]. Available: https://www.tandfonline.com/doi/full/10.1080/08827508.2020.1781109

[4] E. N. Nedkvitne, 'Leaching and Precipitation Experiments Related to the Pedersen Process', Master thesis, NTNU, 2019. Accessed: Feb. 26, 2023. [Online]. Available: https://ntnuopen.ntnu.no/ntnu-xmlui/handle/11250/2623362

[5] V. Canaguier and E. Ringdalen, 'Reduction Kinetics of Pre-Oxidized Ilmenite Pellets by H2-H2O Gas Mixtures', *Metals*, vol. 13, no. 2, Art. no. 2, Feb. 2023, doi: 10.3390/met13020332.

[6] 'Bayer Process - an overview | ScienceDirect Topics'. https://www.sciencedirect.com/topics/engineering/bayer-process (accessed Mar. 15, 2023).

[7] 'Mining and Refining – Process'. https://bauxite.world-aluminium.org/refining/process/ (accessed Feb. 26, 2023).

[8] A. K. Pandey and R. Prakash, 'Process flow diagram of alumina production (Bayer process)[30]', *ResearchGate*, 2020. https://www.researchgate.net/figure/Process-flow-diagram-of-alumina-production-Bayer-process_fig3_340705023 (accessed Mar. 15, 2023).

[9] C. Brunori, C. Cremisini, P. Massanisso, V. Pinto, and L. Torricelli, 'Reuse of a treated red mud bauxite waste: studies on environmental compatibility', *J. Hazard. Mater.*, vol. 117, no. 1, pp. 55–63, Jan. 2005, doi: 10.1016/j.jhazmat.2004.09.010.

[10] 'Let's talk about Red Mud (Bauxite Residue) – h2020harare.eu'. https://h2020harare.eu/lets-talk-about-red-mud-bauxite-residue (accessed Mar. 15, 2023).

[11] pontikes, 'Characteristics – Red Mud Project'. https://redmud.org/red-mud/characteristics/ (accessed Mar. 15, 2023).

[12] 'Toxic mud effects likely to be long term in Hungary', 2010. https://wwf.panda.org/wwf_news/?195473/Toxic-mud-effects-likely-to-be-long-term-in-Hungary (accessed Mar. 15, 2023).

[13] S. Ruyters, J. Mertens, E. Vassilieva, B. Dehandschutter, A. Poffijn, and E. Smolders, 'The Red Mud Accident in Ajka (Hungary): Plant Toxicity and Trace Metal Bioavailability in Red Mud Contaminated Soil', *Environ. Sci. Technol.*, vol. 45, no. 4, pp. 1616–1622, Feb. 2011, doi: 10.1021/es104000m.

[14] T. Marshall and P. Online, 'Hungarian red mud spill did little long-term damage'. https://phys.org/news/2014-11-hungarian-red-mud-long-term.html (accessed Mar. 15, 2023).

[15] A. S. Verma, N. M. Suri, and S. Kant, 'Applications of bauxite residue: A mini-review', *Waste Manag. Res.*, vol. 35, no. 10, pp. 999–1012, Oct. 2017, doi: 10.1177/0734242X17720290.

[16] S. Agrawal, V. Rayapudi, and N. Dhawan, 'Extraction of Iron values from Red mud', *Mater. Today Proc.*, vol. 5, no. 9, pp. 17064–17072, Jan. 2018, doi: 10.1016/j.matpr.2018.04.113.

[17] W. Li, Z. Li, N. Wang, and H. Gu, 'Selective extraction of rare earth elements from red mud using oxalic and sulfuric acids', *J. Environ. Chem. Eng.*, vol. 10, no. 6, p. 108650, Dec. 2022, doi: 10.1016/j.jece.2022.108650.

[18] 'ENSUREAL's final presentation', Jul. 18, 2022. https://ensureal.eu/ensureals-final-presentation/ (accessed May 04, 2023).

[19] 'h2020harare.eu – Hydrogen-based metal recovery from waste'. https://h2020harare.eu/ (accessed May 04, 2023).

[20] L. Kolbeinsen, 'sintring', *Store norske leksikon*. Jan. 24, 2023. Accessed: Apr. 14, 2023. [Online]. Available: https://snl.no/sintring

[21] M. K. Kar, C. van der Eijk, and J. Safarian, 'Kinetics Study on the Hydrogen Reduction of Bauxite Residue-Calcite Sintered Pellets at Elevated Temperature', *Metals*, vol. 13, no. 4, Art. no. 4, Apr. 2023, doi: 10.3390/met13040644.

[22] 'metals-13-00644-g003.png (3895×2788)'. https://www.mdpi.com/metals/metals-13-00644/article_deploy/html/images/metals-13-00644-g003.png (accessed Apr. 26, 2023).

[23] 'Gibbs free energy and spontaneity (article) | Khan Academy', *Khan academy*. https://www.khanacademy.org/_render (accessed Mar. 15, 2023).

[24] D. Spreitzer and J. Schenk, 'Iron Ore Reduction by Hydrogen Using a Laboratory Scale Fluidized Bed Reactor: Kinetic Investigation—Experimental Setup and Method for Determination', *Metall. Mater. Trans. B*, vol. 50, no. 5, pp. 2471–2484, Oct. 2019, doi: 10.1007/s11663-019-01650-9.

[25] D. Spreitzer and J. Schenk, 'Reduction of Iron Oxides with Hydrogen—A Review - Spreitzer - 2019 - steel research international - Wiley Online Library'. https://onlinelibrary.wiley.com/doi/full/10.1002/srin.201900108 (accessed Mar. 15, 2023).

[26] S. O. Velle, F. Vollan, and O. B. Skibelid, 'Hydrogen-Based Iron Recovery from Bauxite Residue', Bachelor thesis, NTNU, 2022. Accessed: Apr. 09, 2023. [Online]. Available: https://ntnuopen.ntnu.no/ntnu-xmlui/handle/11250/3007027

[27] L. Zhi-feng, Y. Gao, G.-M. Cao, and Z. Liu, 'Fe–O binary equilibrium phase diagram', *ResearchGate*. https://www.researchgate.net/figure/Fe-O-binary-equilibrium-phase-diagram_fig3_335876296 (accessed Mar. 15, 2023).

[28] 'Ellingham diagram'.

[29] 'Ellingham Diagram - Thermodynamics Principle of Metallurgy', *GeeksforGeeks*, Mar. 27, 2022. https://www.geeksforgeeks.org/ellingham-diagram/ (accessed Mar. 15, 2023).

[30] D. R. Gaskell, 'Metal production: Ellingham diagrams', [Online]. Available: https://www.uobabylon.edu.iq/eprints/publication_12_25331_298.pdf

[31] A. Heidari, N. Niknahad, M. Iljana, and T. Fabritius, 'A Review on the Kinetics of Iron Ore Reduction by Hydrogen', *Materials*, vol. 14, no. 24, p. 7540, Dec. 2021, doi: 10.3390/ma14247540.

[32] P. Garg, X. Hu, Y. Li, K. Li, S. Nag, and J. Zhang, 'Kinetics of Iron Oxide Reduction in H2=H2O Gas Mixture: Global and Stepwise Reduction', *Metall. Mater. Trans. B*, vol. 53, no. 3, pp. 1759–1774, Jun. 2022, doi: 10.1007/s11663-022-02485-7.

[33] S. Mukherjee, 'Fick's Laws of Diffusion: Formulas, Equations, & Examples', *Science Facts*, Jul. 10, 2020. https://www.sciencefacts.net/ficks-laws.html (accessed May 02, 2023).

[34] M. J. dos Anjos, R. T. Lopes, E. F. O. de Jesus, J. T. Assis, R. Cesareo, and C. A. A. Barradas, 'Quantitative analysis of metals in soil using X-ray fluorescence', *Spectrochim. Acta Part B At. Spectrosc.*, vol. 55, no. 7, pp. 1189–1194, Jul. 2000, doi: 10.1016/S0584-8547(00)00165-8.

[35] B. Beckhoff, B. Kanngiesser, N. Langhoff, R. Wedell, and H. Wolff, 'Handbook of Practical X-ray Fluorescence Analysis', Nov. 2005, [Online]. Available: https://link.springer.com/book/10.1007/978-3-540-36722-2

[36] U. Kramar, 'Advances in energy-dispersive X-ray fluorescence', *J. Geochem. Explor.*, vol. 58, no. 1, pp. 73–80, Feb. 1997, doi: 10.1016/S0375-6742(96)00053-2.

[37] K. C. A. Smith and C. W. Oatley, 'The scanning electron microscope and its fields of application', *Br. J. Appl. Phys.*, vol. 6, no. 11, p. 391, Nov. 1955, doi: 10.1088/0508-3443/6/11/304.

[38] A. Mohammed and A. Abdullah, 'SCANNING ELECTRON MICROSCOPY (SEM): A REVIEW'.

[39] K. L. Scrivener, 'Backscattered electron imaging of cementitious microstructures: understanding and quantification', *Cem. Concr. Compos.*, vol. 26, no. 8, pp. 935–945, Nov. 2004, doi: 10.1016/j.cemconcomp.2004.02.029.

[40] 'Scanning Electron Microscopy | Electrons in SEM - NO'. https://www.thermofisher.com/uk/en/home/materials-science/learning-center/applications/sem-electrons.html (accessed Feb. 26, 2023).

[41] D. Brandon and W. D. Kaplan, *Microstructural Characterization of Materials*. Israel Institute of Technology: John Wiley & Sons, 1999.

[42] V.-D. Hodoroaba, 'Chapter 4.4 - Energy-dispersive X-ray spectroscopy (EDS)', in *Characterization of Nanoparticles*, V.-D. Hodoroaba, W. E. S. Unger, and A. G. Shard, Eds., in Micro and Nano Technologies. Elsevier, 2020, pp. 397–417. doi: 10.1016/B978-0-12-814182-3.00021-3.

[43] R. Tanaka, K. Yuge, J. Kawai, and H. Alawadhi, 'Artificial peaks in energy dispersive X-ray spectra: sum peaks, escape peaks, and diffraction peaks', *X-Ray Spectrom.*, vol. 46, no. 1, pp. 5–11, 2017, doi: 10.1002/xrs.2697.

[44] P. Mudgal, 'Characteristic radiation | Radiology Reference Article | Radiopaedia.org', *Radiopaedia*. https://radiopaedia.org/articles/characteristic-radiation (accessed Feb. 26, 2023).

[45] A. A. Bunaciu, E. gabriela Udriştioiu, and H. Y. Aboul-Enein, 'X-Ray Diffraction: Instrumentation and Applications', *Crit. Rev. Anal. Chem.*, vol. 45, no. 4, pp. 289–299, Oct. 2015, doi: 10.1080/10408347.2014.949616.

[46] B. D. Cullity, 'Element of X-ray diffraction', 1956.

[47] Y. Tian and J. Wu, 'A comprehensive analysis of the BET area for nanoporous materials', *AIChE J.*, vol. 64, no. 1, pp. 286–293, 2018, doi: 10.1002/aic.15880.

[48] R. Bardestani, G. S. Patience, and S. Kaliaguine, 'Experimental methods in chemical engineering: specific surface area and pore size distribution measurements—BET, BJH, and DFT', *Can. J. Chem. Eng.*, vol. 97, no. 11, pp. 2781–2791, 2019, doi: 10.1002/cjce.23632.

[49] 'BookitLab! - Instrument Specifications'. https://core.bookitlab.com/ntnu/assets/details.aspx?id=367 (accessed May 05, 2023).

Appendix

List of Appendix Figures

I – Risk assessment

RISK ASSESSMENT (RiskManager alternative)

Unit/Institute:	IMA			Date: 17/1/2023	
Responsible line manager (name):	Ida Westermann			Revised:	
Responsible for activities being risk assessed (name):	Prof. Jafar Safarian				
Participants in the risk assement (names):	Prof. Jafar Safarian, Dali Hariswijaya, Sivert Ragnhildstveit Erland, Elias Trondsen Dahl				
Description of the activity, process, area, etc.: .					

Sintering and reduction process of bauxite residue and Fe-containing synthetic minerals with hydrogen gas. The experiment will consist of 2 main parts. The sintered pellets are going to be reduced with a mix of H2-H2O gas and pure H2 gas at some point, reduction temperature shall be between 800-1000 C degree. In the second part red mud (bauxite residue) will be mixed with Ca(OH)2 and made into pellets using a pelletizer. CaO in this experiment will be made from industrial limestone by calcining in a muffle furnace at 950 C for 4 hours. The pellets will be sintered in air atmosphere and similarly with previous experiment it will be reduced with a mix of H2-H2O gas and pure H2 gas. In the second part, hydrogen recovery process of the flue gas from reduction process will be attempted. Separation of H2O in the flue gas will be done by distillation and the remaining gas will be reintroduced into the furnace along with input gas line.

Activity / process	Unwanted incident	Existing risk reducing measures	Probability (P) (1-5)	Consequence (C)				Risk value (P x C)	Risk reducing measures - suggestions	Residual risk after measures being
				Health (1-5)	Material values (1-5)	Environment (1-5)	Reputation (1-5)		Measures reducing the probability of the unwanted incident happening should be prioritized.	
Drying of Bauxite residue (BR)in oven	Burn injury due to direct contact with hot container or heating element	Heat-resistant gloves	1	1	1	1	1	1	Using heat resistant gloves everytime a sample is going to be put in or taken out	1
Adding powder mix (BR-Ca(OH)2) into pelletizing disc	The bauxite residue sample may have harmful properties	Lubrication of dies	1	2	1	1	1	2	Make sure the dies is lubricated properly before each usage	1
Pelletizing of bauxite residue mix		PPE	1	1	1	1	1	1	- Check with the sample owner about possibility of harmful properties and ask for safety declaration form - Make sure to examine the data sheet for chemicals in the mix	1
Adding powder mix (BR-Ca(OH)2) into pelletizing disc	Inhalation of sample or reagent fines can cause lung damage, contact with eye may cause irritation	Protective goggle and mask	1	1	1	1	1	1	Make sure to wear protective goggle and mask during pelletizing	1
Drying the green pellets	Burn injury due to direct contact with hot container or heating element	Heat-resistant gloves	1	1	1	1	1	1	Make sure the sample is properly cooled before taking it out and wear heat resistant gloves.	1
Sintering process of pellets in muffle furnace (1100 C degree)	Burn injury due to direct contact with hot container or heating element	Heat-resistant gloves	1	1	1	1	1	1	Using heat resistant gloves everytime a sample is going to be put in or taken out	1
Sintering process of pellets in muffle furnace (1100 C degree)	Hazardous gas being produced from unknown reaction in the pellet	Point suction	1	1	1	1	1	1	Make sure to put the point suction on gas outlet and turn it on before each usage	1
Connecting and opening H2 gas bottle to the alumina tube furnace (will be handled together with engineer)	Gas leakage	Room gas detector	2	2	2	1	1	4	Using helium gas and helium detector to check for leakage before experiment. Follow safety rules for usage of hydrogen gas.	2
Hydrogen reduction of sintered pellets in alumina tube furnace (600-1000 C degree)	One undesirable action is mixing the outlet and inlet cooling water levers. This will cause overpressure, which is undesired. This may also cause fire.	Fire extinguisher	1	2	3	1	1	2	Turn off power and inform the room responsible, close hydrogen gas line	1
	Furnace is not properly sealed, gas can come out when overpressure happens	Gas detector	2	2	1	1	1	4	- Modify furnace flange to have better sealing system. - Close hydrogen gas line, turn off power and inform the room responsible.	2
	Water/residue clogging on gas outlet	Gas detector	2	2	1	1	1	4	Clean and check gas outlet line before each usage	2
	No automatic off system on the furnace when gas leakage happened	Gas detector	1	2	1	1	1	2	- Quickly shut off the gas line when gas leakage is detected and inform room responsible - Installs point suction above the furnace to minimize gas leakage effect'	1
	If the furnace is not properly cooled the sample may be hot. This may cause skin burns.	Heat-resistant gloves	1	1	1	1	1	1	Make sure the sample is properly cooled before taking it out and wear heat resistant gloves.	1
Shutting off H2 gas valve after usage	H2 gas line is connected with other furnaces in other rooms, other people might still use the gas when the experiment finished	-	1	1	1	1	1	1	Communicate with other lab users everyday about their H2 gas usage plan	1
Making powder samples for XRF and XRD analysis in ring mill	Inhaling fine particles when the chamber is opened	Having mask and safety glasses	1	1	1	1	1	1	Work under ventilation so that possible dust is taken awa	1
Preparing metallography sample for SEM	Inhaling evolved gas from the resin and skin damage	Gloves will be used and the work in fume hood	1	1	1	1	1	1	The work will be done with the lab engineer/co-supervisor	1
Handling liquid nitrogen during BET anlysis	Frost damages to skin	Cold-resistant gloves and protective face gear	1	1	1	1	1	1	Always use protective gloves and face gear when filling the tank with liquid nitrogen	1

Appendix Figure 1: Risk assessment for this study.

II – XRF results from Sintef Norlabs and Degerfors laboratory, raw data

A – Raw BR

Prøvenr.: 103533-002	Prøvetype:	Dato:	Prøvemerking: Red mud/bauxite residue			Prøvetaker: Oppdragsgiver	Mottaksdato: 30.06.21
Analyse/Parameter		Resultat	Enhet	Usikkerhet	Analysedato	Metodbeskrivelse	
*) Al2O3		22.0	%		01.07.21	Intern metode, XRF	
*) CaO		8.8	%		01.07.21	Intern metode, XRF	
*) Fe		28.5	%		01.07.21	Intern metode, XRF	
*) K2O		0.09	%		01.07.21	Intern metode, XRF	
*) MgO		0.23	%		01.07.21	Intern metode, XRF	
*) MnO		0.08	%		01.07.21	Intern metode, XRF	
*) Na2O		3.1	%		01.07.21	Intern metode, XRF	
*) P		0.05	%		01.07.21	Intern metode, XRF	
*) S		0.38	%		01.07.21	Intern metode, XRF	
*) SiO2		7.1	%		01.07.21	Intern metode, XRF	
*) TiO2		5.0	%		01.07.21	Intern metode, XRF	

Appendix Figure 2: Raw data for XRF analysis from Sintef Norlabs.

B - Sintered BR

D-LAB
DEGERFORS LABORATORIUM AB

1 (1)

Provningsresultat / Test Results:

Ordernr / Orderno
DL-76080

Beställare / Client	Referens / Reference
NTNU	Dali Hariswijaya

Adress / Address
Alfred Getz Vei 2, N-7034 TRONDHEIM

Er beställning / Your order No	Ankomstdag / Sample Registration Date	Utskriftsdatum / Date of issue	DL ID
	2023-03-24	2023-03-28	730165

Provbeteckning / Sample identity
Mix of bauxite residue and calcium hydrate

Noteringar / Notes

Resultat/
Results

CaO	29.0 %
MgO	0.37 %
SiO_2	7.65 %
Al_2O_3	23.1 %
Fe_2O_3	30.5 %
MnO	0.04 %
Cr_2O_3	0.18 %
V_2O_5	0.15 %
TiO_2	3.86 %
NiO	0.06 %
Na_2O	3.60 %
K_2O	0.10 %
P_2O_5	0.12 %
SO_3	1.03 %
ZrO_2	0.11 %
SrO	0.03 %
Co_3O_4	0.02 %

This report may not be reproduced other than in full, except with the prior written approval of the issuing laboratory.

Note: The results are only valid for the sample that has been delivered to the laboratory.
We are not responsible for electronically transferred reports due to changes of data during transmission. Please contact us in doubtful cases.

DEGERFORS LABORATORIUM

Björn Bernhardsson

Rapporten är signerad digitalt/
The report is digitally signed

Degerfors Laboratorium AB
Box 54
SE-693 21 DEGERFORS

Phone +46 586- 21 63 50

Web: www.degerforslab.se
Email: info@degerforslab.se

Bankgiro: 5735-6784
Bank: Swedbank, Degerfors
IBAN: SE848000081562983744494

Appendix Figure 3: Raw data for XRF analysis from Degerfors Labs.

III – Calculations

From Equation 19, the reduction degrees can be calculated. Total amount of oxygen in Fe_2O_3 for each sample was calculated using Excel. The mass loss percentage was calculated using Equation 18.

Experiment no. 1 (0% humidity, 600°C):

$$\%W_{red} = \frac{0,9473\ g}{1,908229756\ g} \cdot 100\% = 49,64\%$$

Experiment no. 2 (5% humidity, 600°C):

$$\%W_{red} = \frac{0,4862\ g}{1,902432871\ g} \cdot 100\% = 25,56\%$$

Experiment no. 3 (15% humidity, 600°C):

$$\%W_{red} = \frac{0,3476\ g}{1,907878141\ g} \cdot 100\% = 18,22\%$$

Experiment no. 4 (25% humidity, 600°C):

$$\%W_{red} = \frac{0,2985\ g}{1,903212125\ g} \cdot 100\% = 15,68\%$$

Experiment no. 5 (0% humidity, 800°C):

$$\%W_{red} = \frac{1,3779\ g}{1,906927832\ g} \cdot 100\% = 72,26\%$$

Experiment no. 6 (5% humidity, 800°C):

$$\%W_{red} = \frac{1,3661\ g}{1,901311507\ g} \cdot 100\% = 71,85\%$$

Experiment no. 7 (15% humidity, 800°C):

$$\%W_{red} = \frac{1,3250\ g}{1,907811620\ g} \cdot 100\% = 69,45\%$$

Experiment no. 8 (25% humidity, 800°C):

$$\%W_{red} = \frac{0,4249\ g}{1,913846081\ g} \cdot 100\% = 22,20\%$$

Mass loss in percentage for all experiments:

Mass loss from dried pellets to sintered pellets:

$$\%Mass loss = \frac{(854,21 - 540,54)}{854,21} \cdot 100\% = 36,7\%$$

Experiment no. 1 (0% humidity, 600°C):

$$\%Mass\ loss = \frac{0,9473}{20,0801} \cdot 100\% = 4,72$$

Experiment no. 2 (5% humidity, 600°C):

$$\%Mass\ loss = \frac{0,4862}{20,0191} \cdot 100\% = 2,43$$

Experiment no. 3 (15% humidity, 600°C):

$$\%Mass\ loss = \frac{0,3476}{20,07643} \cdot 100\% = 1,73$$

Experiment no. 4 (25% humidity, 600°C):

$$\%Mass\ loss = \frac{0,2985}{20,0273} \cdot 100\% = 1,49$$

Experiment no. 5 (0% humidity, 800°C):

$$\%Mass\ loss = \frac{1,3779}{20,0664} \cdot 100\% = 6,87$$

Experiment no. 6 (5% humidity, 800°C):

$$\%Mass\ loss = \frac{1,3661}{20,0073} \cdot 100\% = 6,83$$

Experiment no. 7 (15% humidity, 600°C):

$$\%Mass\ loss = \frac{1,325}{20,0757} \cdot 100\% = 6,60$$

Experiment no. 8 (25% humidity, 800°C):

$$\%Mass\ loss = \frac{0,4249}{20,1392} \cdot 100\% = 2,11$$

IV - SEM point analysis, raw data

The following section shows all the raw data obtained from the point analysis.

A – Sintered
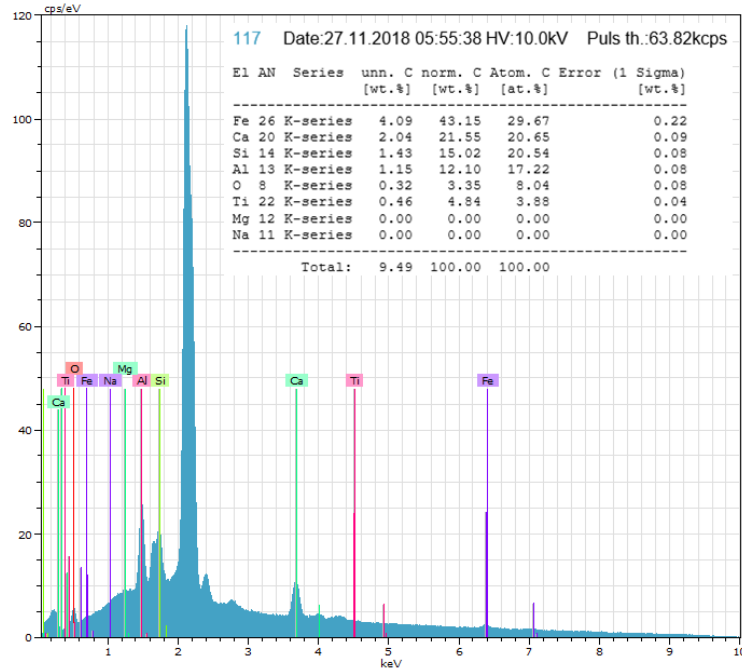
Appendix Figure 4: Point analysis for sintered pellets, point 117.
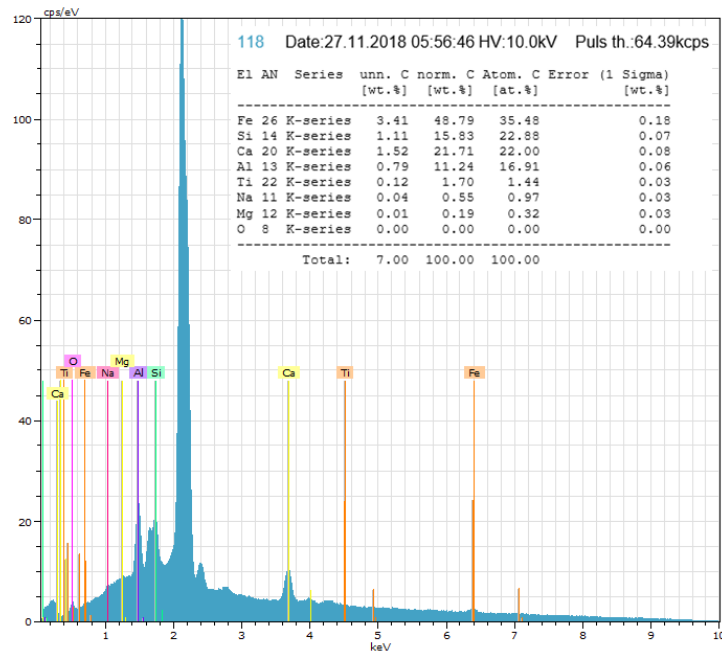
Appendix Figure 5: Point analysis for sintered pellets, point 118.
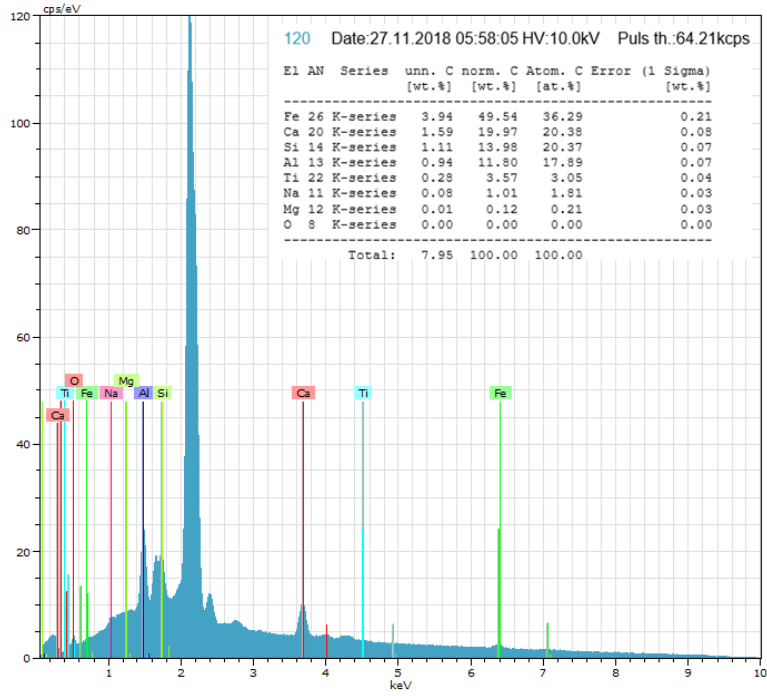
Appendix Figure 6: Point analysis for sintered pellets, point 120.
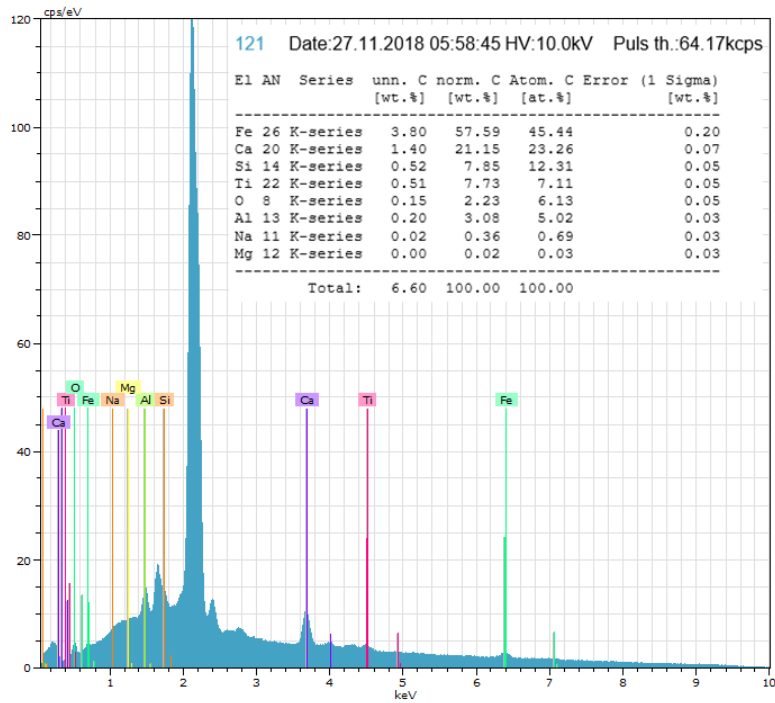
Appendix Figure 7: Point analysis for sintered pellets, point 121.
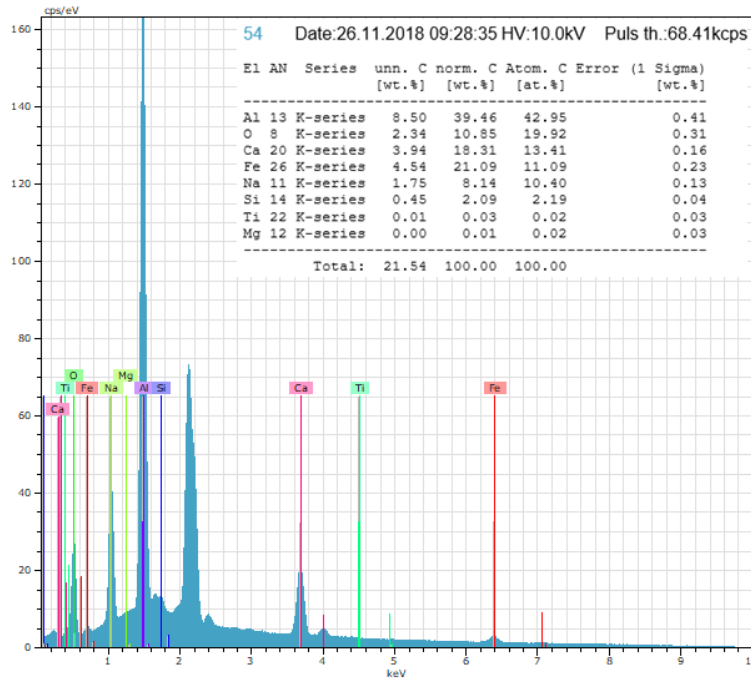
B – 0% H$_2$O 600°C
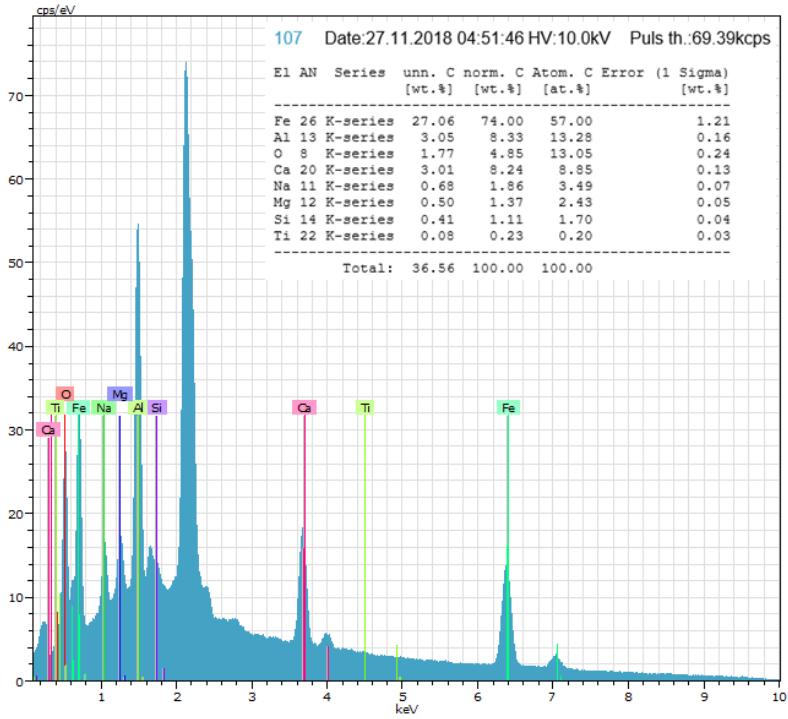
Appendix Figure 8: Point analysis for reduced pellets, 600°C 0% humidity, point 107.
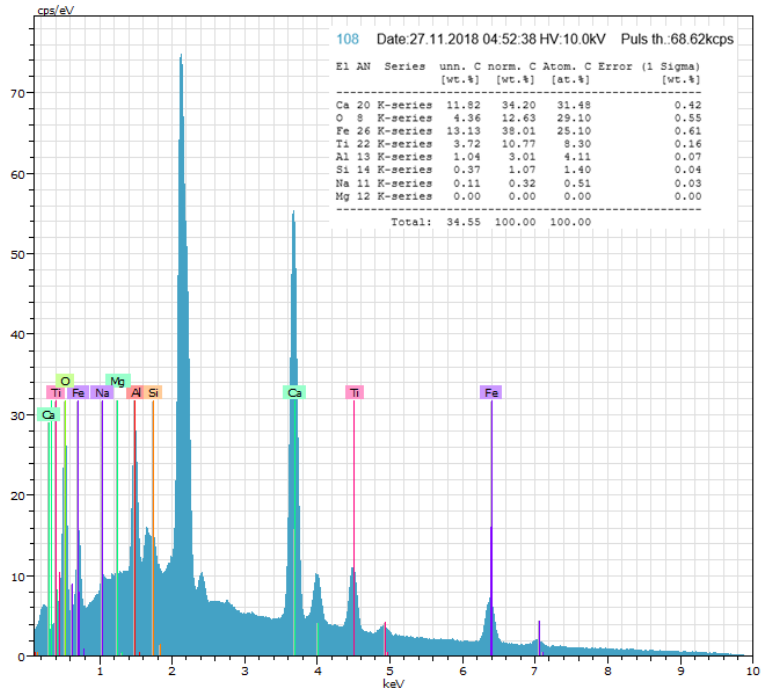
Appendix Figure 9: Point analysis for reduced pellets, 600°C 0% humidity, point 108.
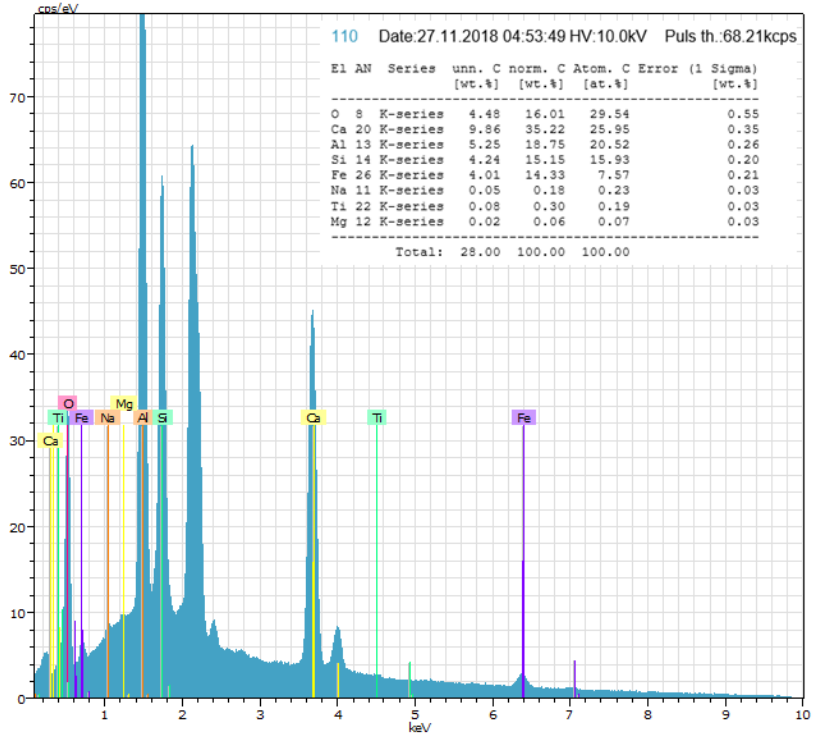
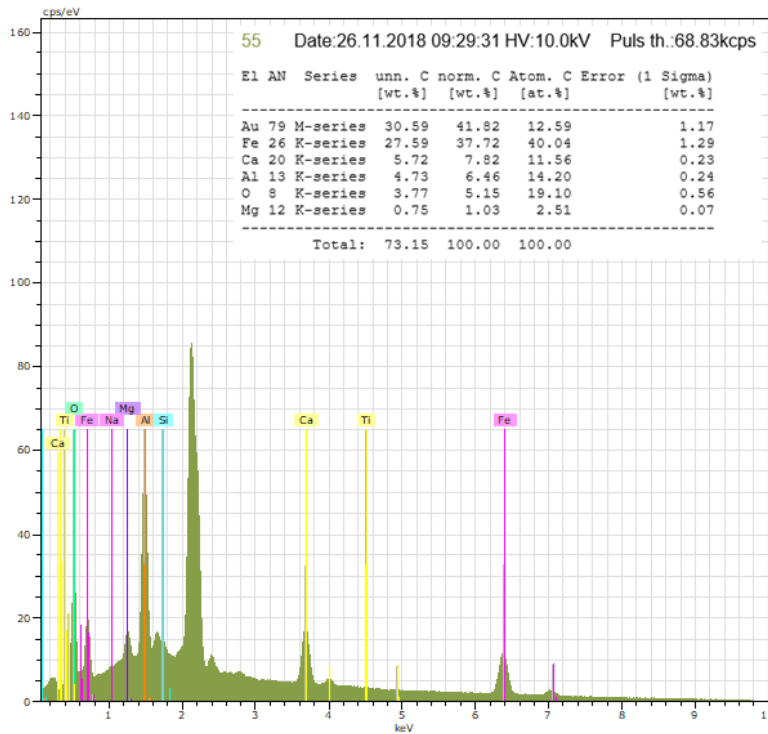**Appendix Figure 10:** Point analysis for reduced pellets, 600°C 0% humidity, point 110.
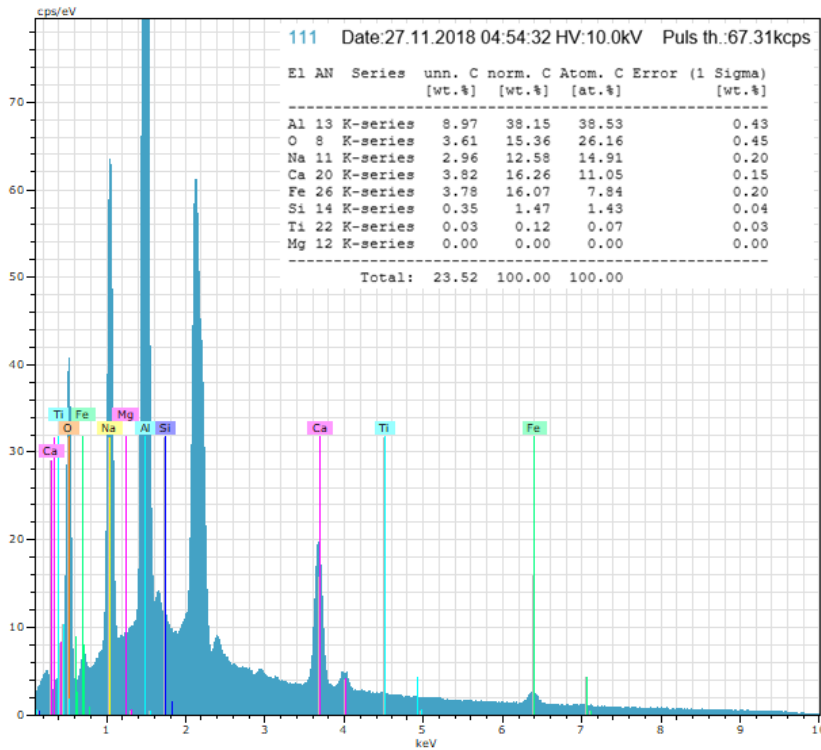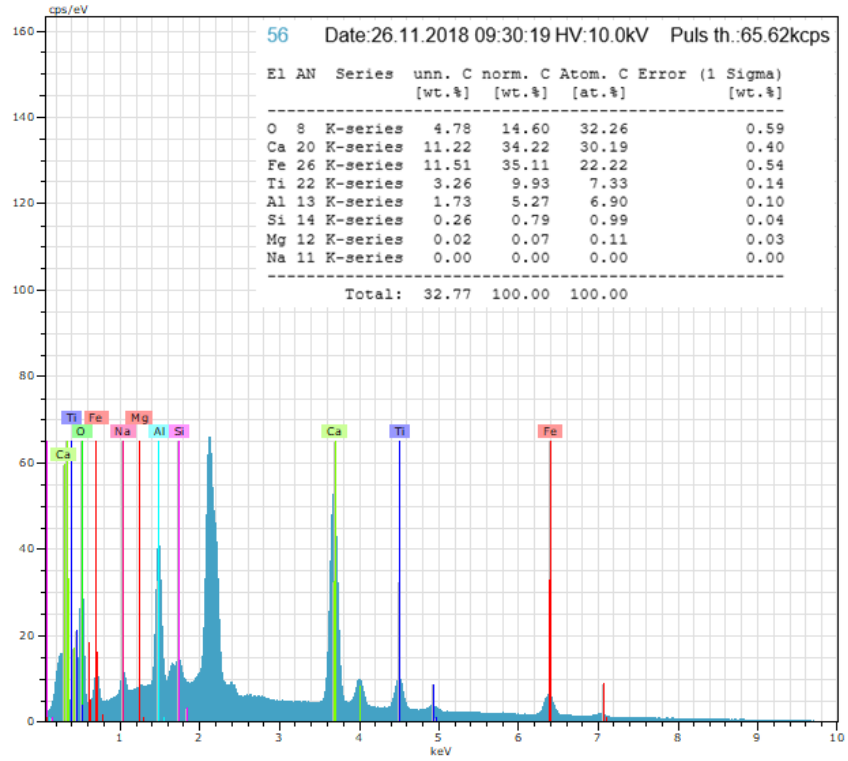

Appendix Figure 11: Point analysis for reduced pellets, 600°C 0% humidity, point 111.
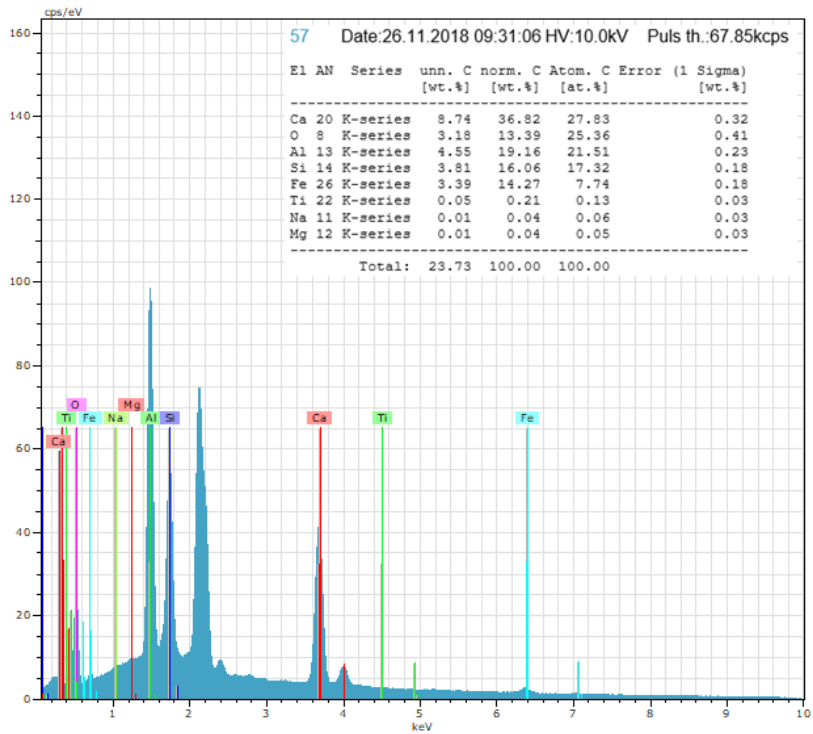
C – 5% H₂O 600°C
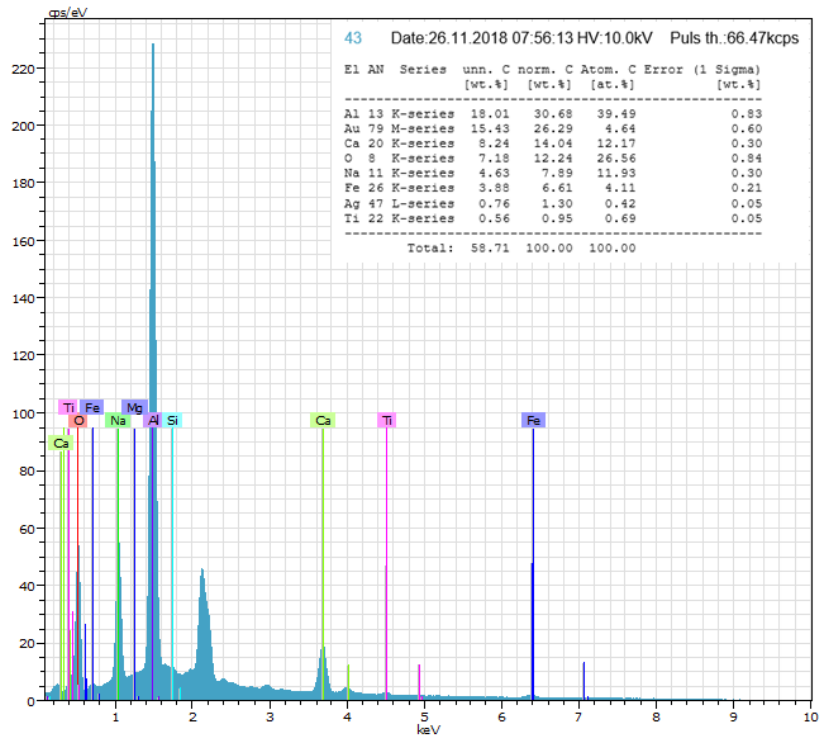
Appendix Figure 12: Point analysis for reduced pellets, 600°C 5% humidity, point 43.
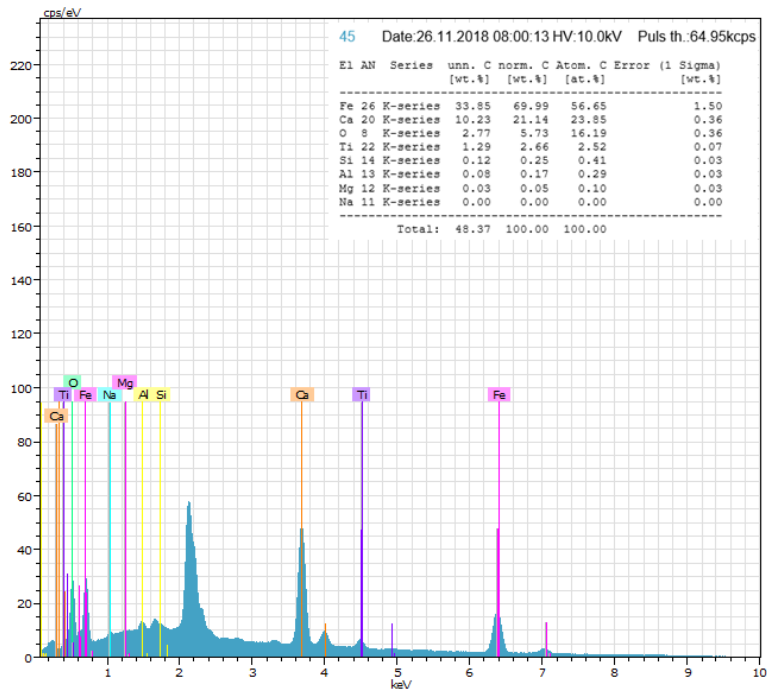
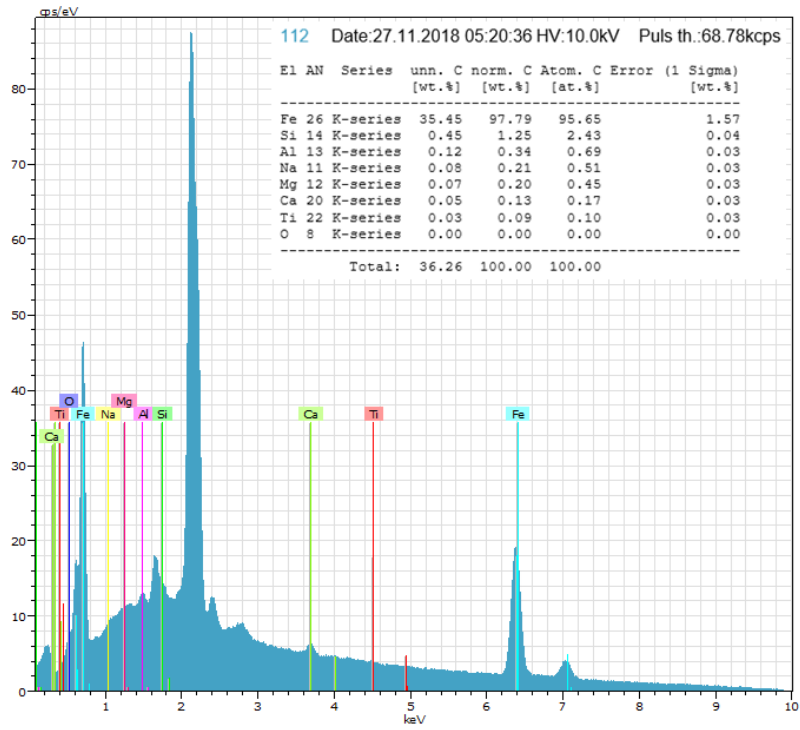**Appendix Figure 13:** Point analysis for reduced pellets, 600°C 5% humidity, point 45.
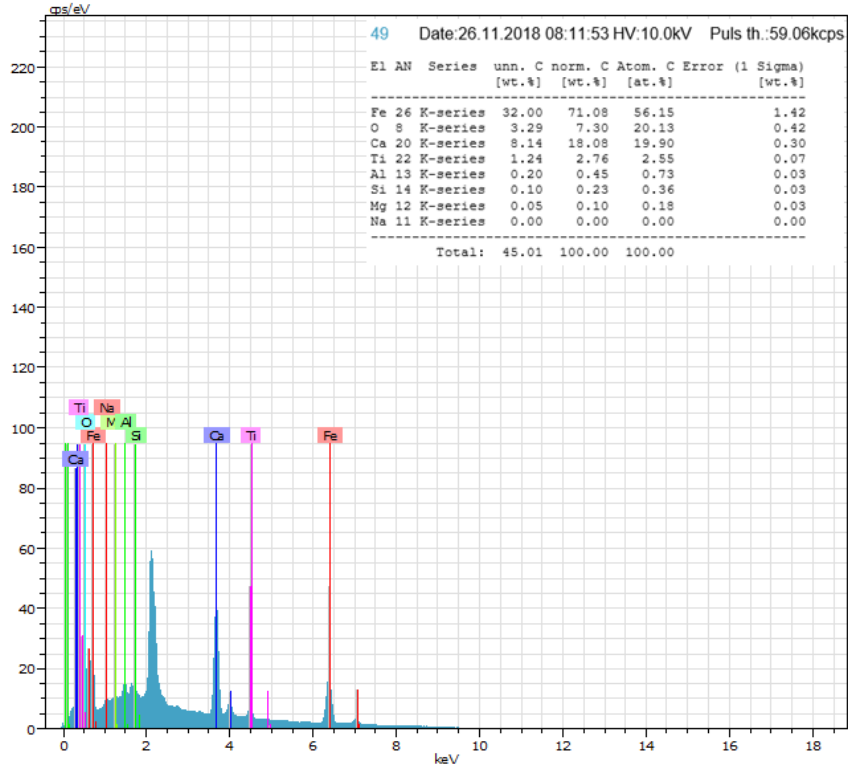
Appendix Figure 14: Point analysis for reduced pellets, 600°C 5% humidity, point 49.

D – 15% H₂O 600°C
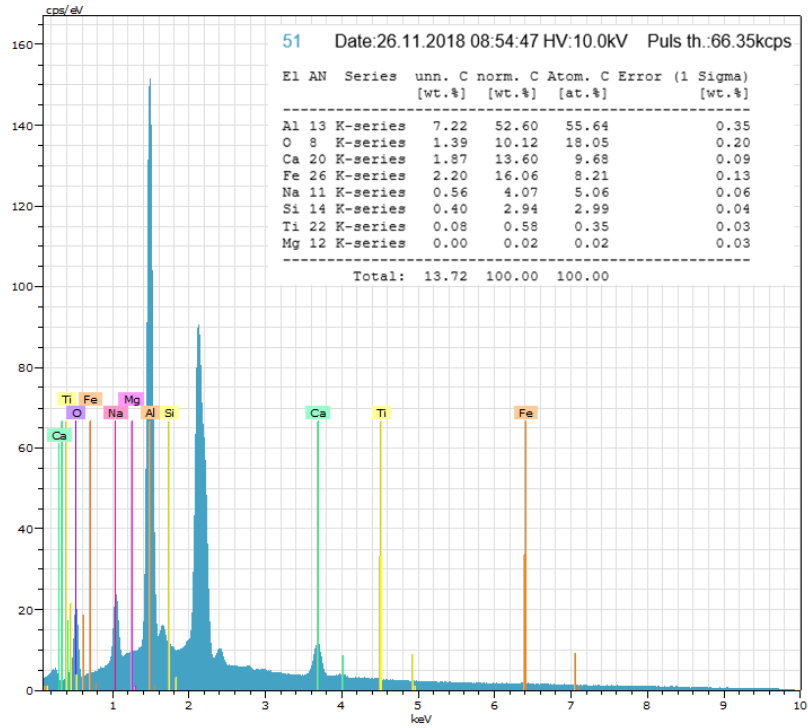
Appendix Figure 15: Point analysis for reduced pellets, 600°C 15% humidity, point 51.
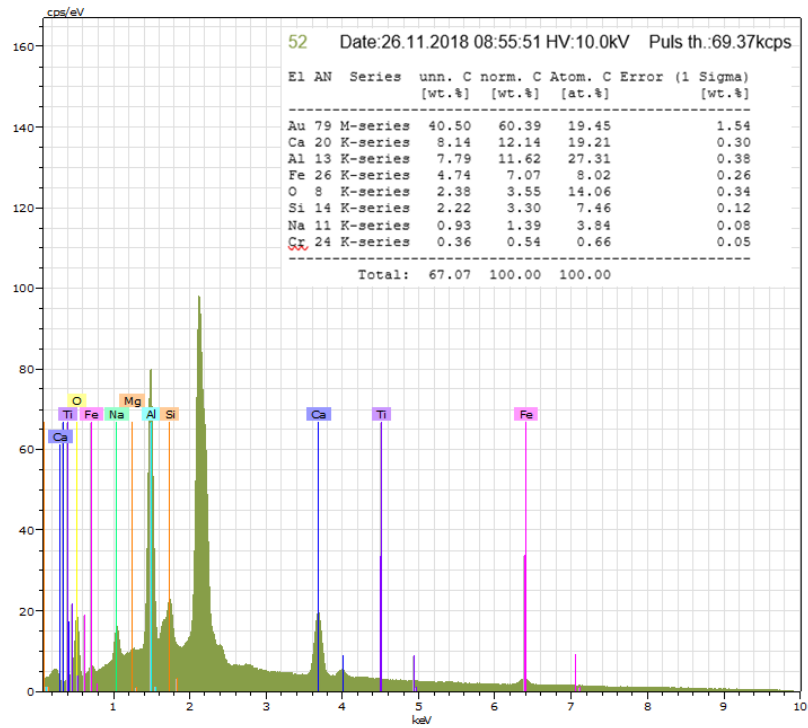
Appendix Figure 16: Point analysis for reduced pellets, 600°C 15% humidity, point 52.
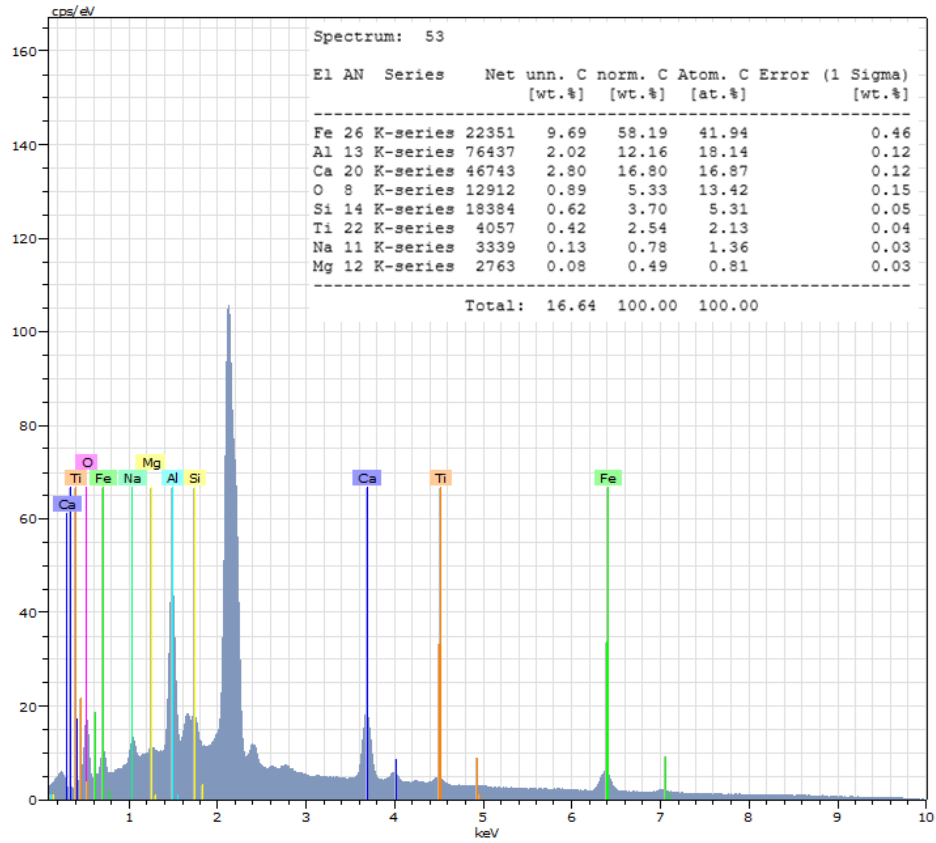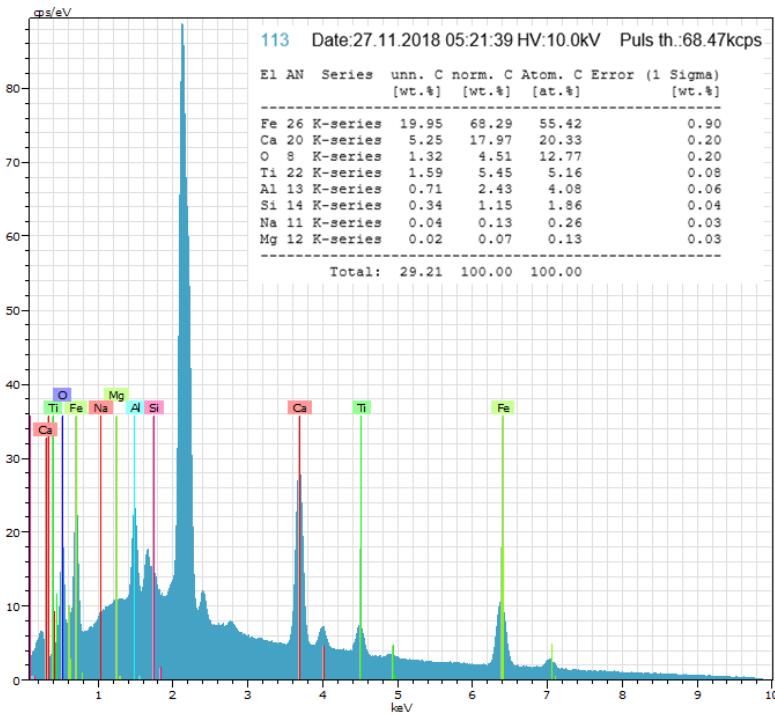
Appendix Figure 17: Point analysis for reduced pellets, 600°C 15% humidity, point 53.

E – 25% H₂O 600°C

Appendix Figure 18: Point analysis for reduced pellets, 600°C 25% humidity, point 54.

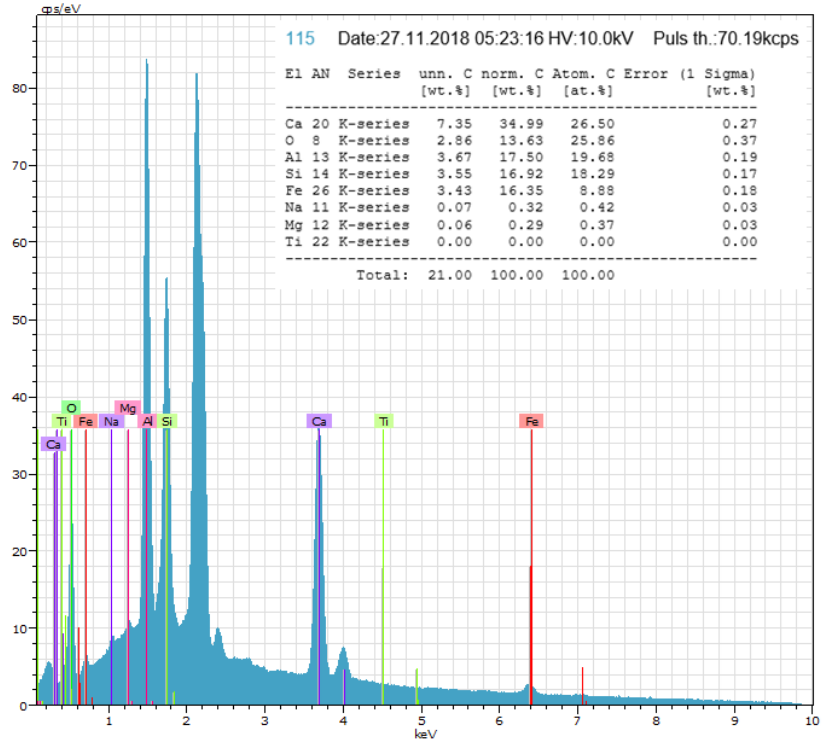**Appendix Figure 19:** Point analysis for reduced pellets, 600°C 25% humidity, point 55.

Appendix Figure 20: Point analysis for reduced pellets, 600°C 25% humidity, point 56.

Appendix Figure 21: Point analysis for reduced pellets, 600°C 25% humidity, point 57.
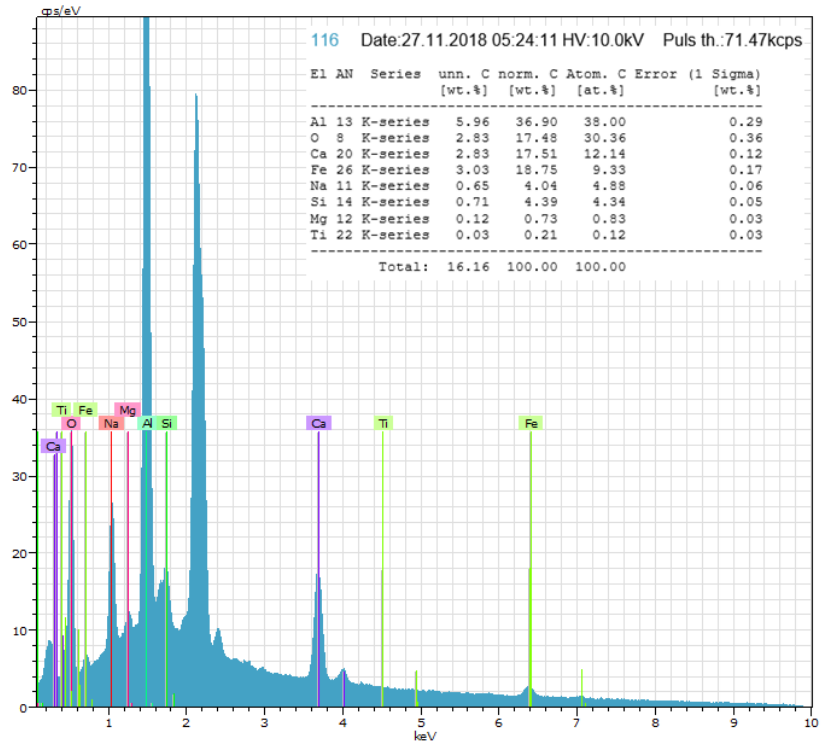
F – 0% H₂O 800°C

Appendix Figure 22: Point analysis for reduced pellets, 800°C 0% humidity, point 112.

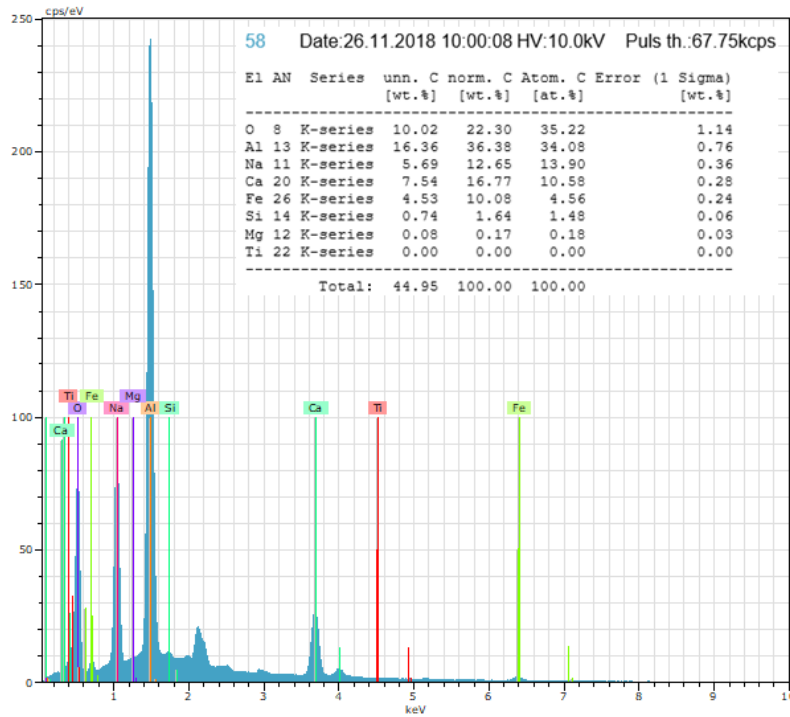**Appendix Figure 23:** Point analysis for reduced pellets, 800°C 0% humidity, point 113.

Appendix Figure 24: Point analysis for reduced pellets, 800°C 0% humidity, point 115.

Appendix Figure 25: Point analysis for reduced pellets, 800°C 0% humidity, point 116.

G – 5% H$_2$0 800°C

Appendix Figure 26: Point analysis for reduced pellets, 800°C 5% humidity, point 58.

Appendix Figure 27: Point analysis for reduced pellets, 800°C 5% humidity, point 59.
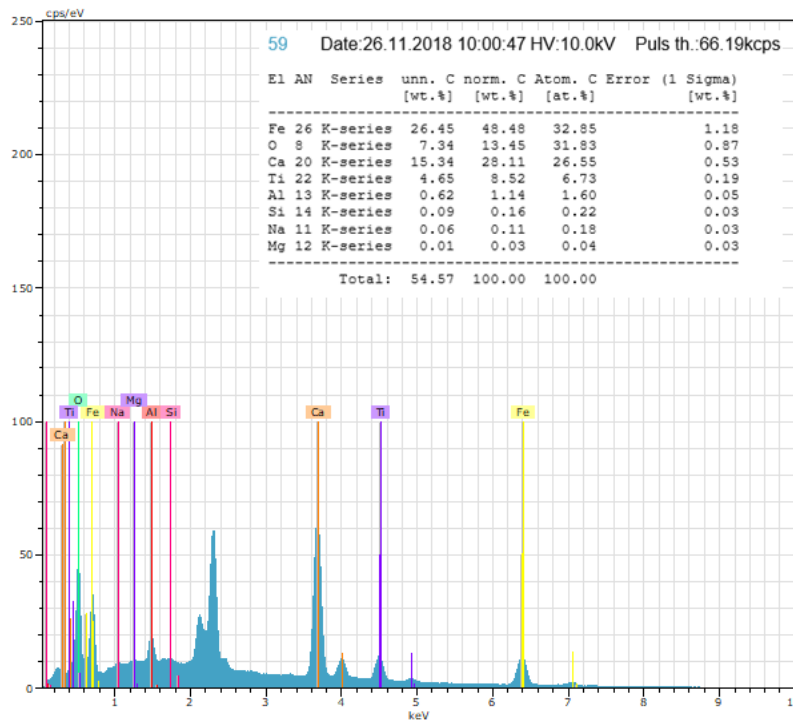
Appendix Figure 28: Point analysis for reduced pellets, 800°C 5% humidity, point 60.
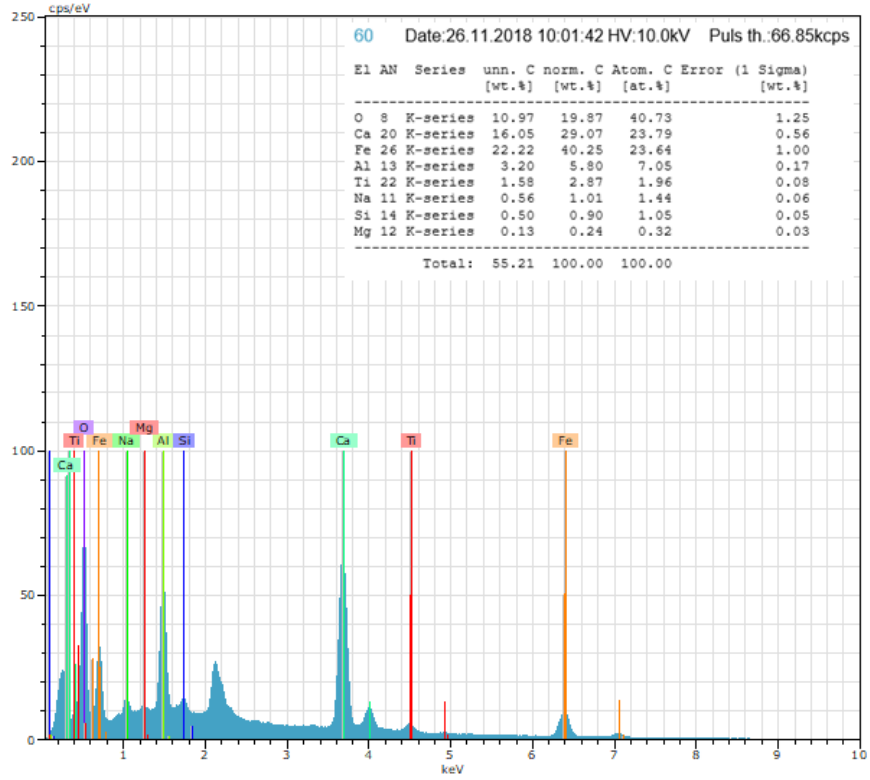
H – 15% H₂O 800°C

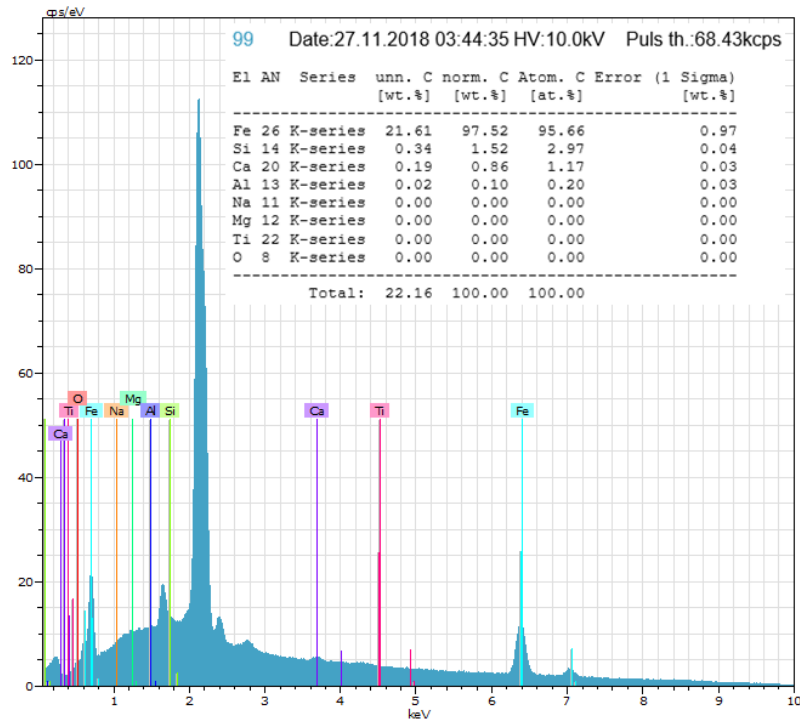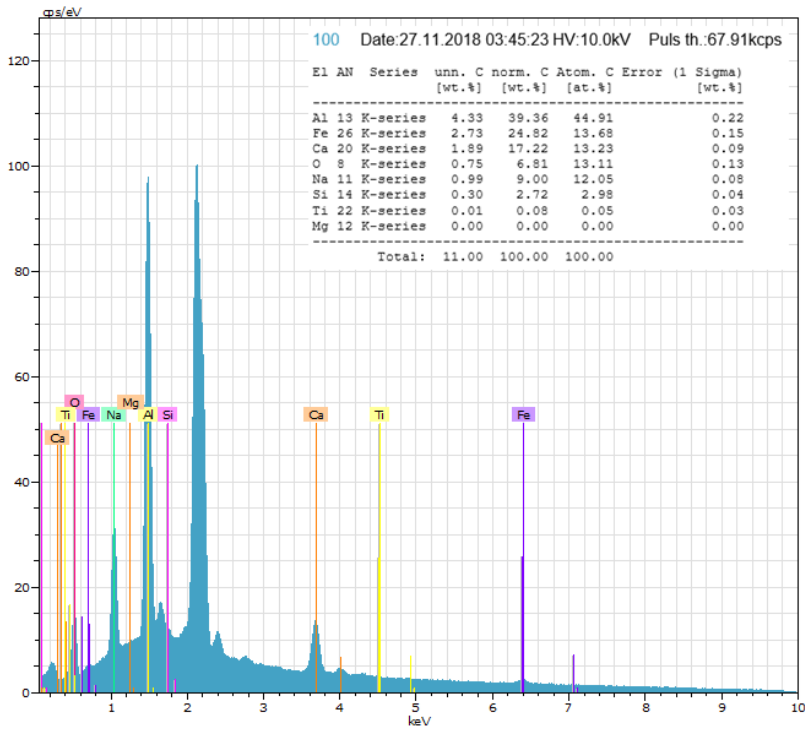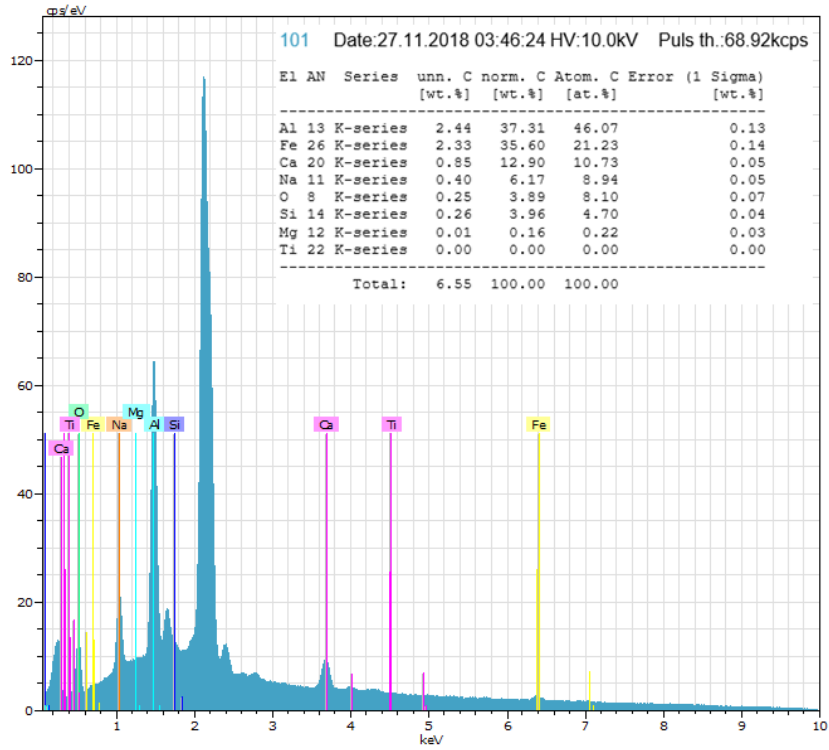**Appendix Figure 29:** Point analysis for reduced pellets, 800°C 15% humidity, point 99.

Appendix Figure 30: Point analysis for reduced pellets, 800°C 15% humidity, point 100.

Appendix Figure 31: Point analysis for reduced pellets, 800°C 15% humidity, point 101.

Appendix Figure 32: Point analysis for reduced pellets, 800°C 15% humidity, point 102.

I – 25% H₂O 800°C
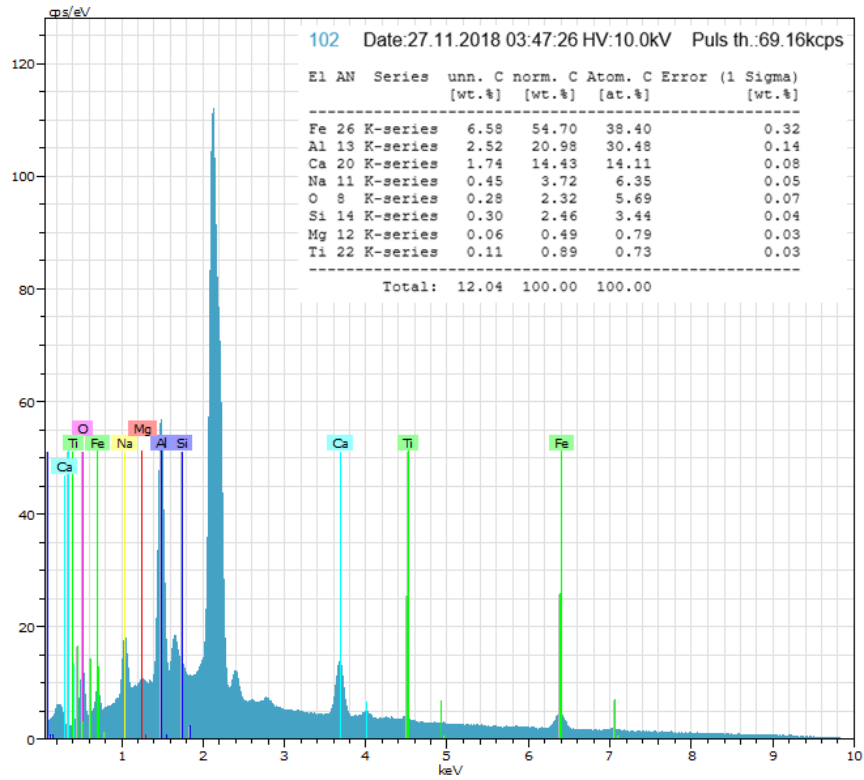

Appendix Figure 33: Point analysis for reduced pellets, 800°C 25% humidity, point 103.
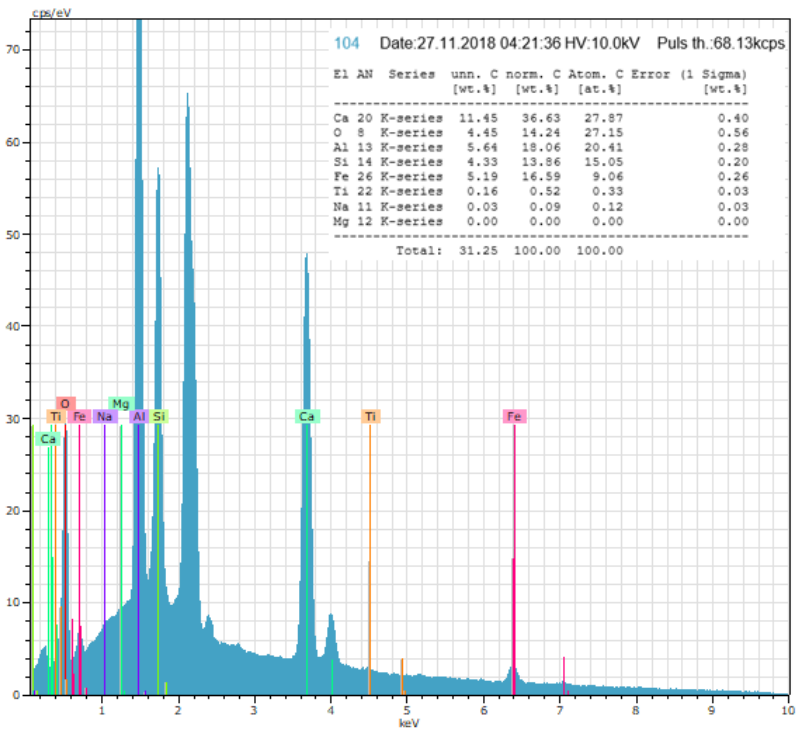
Appendix Figure 34: Point analysis for reduced pellets, 800°C 25% humidity, point 104.
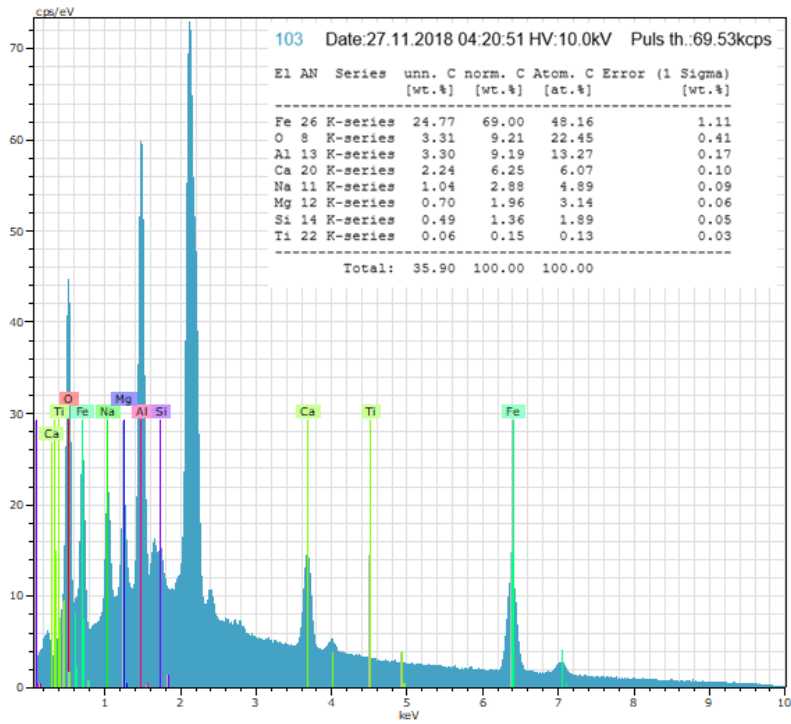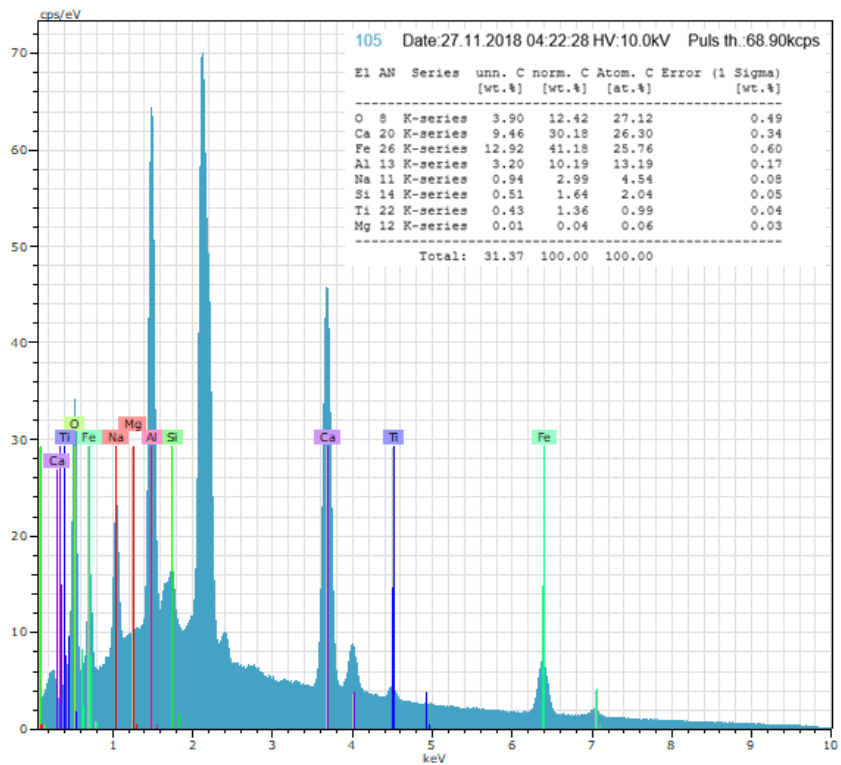
Appendix Figure 35: Point analysis for reduced pellets, 800°C 25% humidity, point 105.
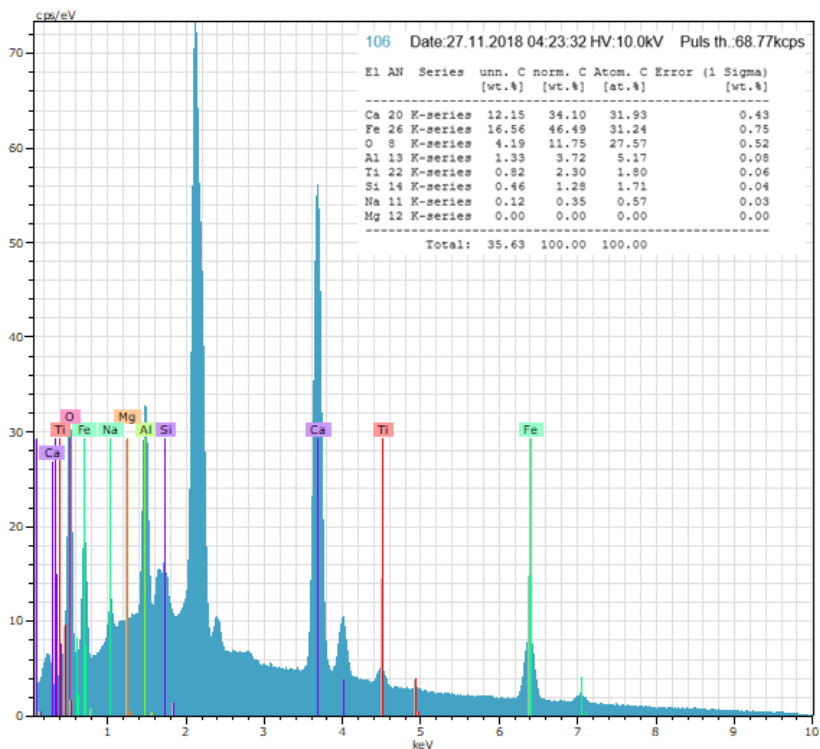
Appendix Figure 36: Point analysis for reduced pellets, 800°C 25% humidity, point 106.

V - XRD Results, raw data

The following section shows all the raw data obtained from XRD analysis.

A – sintered
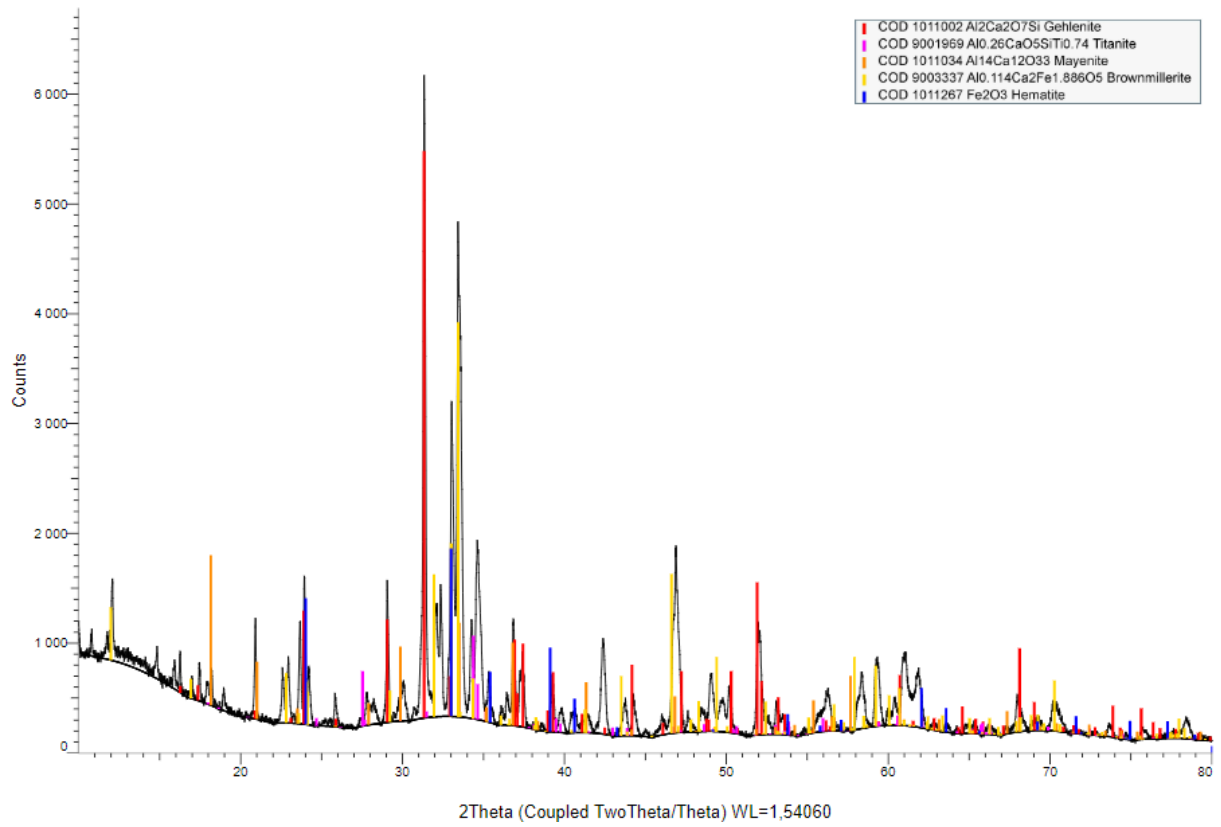
Appendix Figure 37: XRD analysis, raw data for sintered pellets.

B – 0% H₂O 600°C

Appendix Figure 38: XRD results, raw data for reduced pellets, 600°C with 0% humidity.

C – 5% H_2O 600°C

Appendix Figure 39: XRD results, raw data for reduced pellets, 600°C with 5% humidity.

D – 15% H₂O 600°C

Appendix Figure 40: XRD results, raw data for reduced pellets, 600°C with 15% humidity.

E – 25% H₂O 600°C

Appendix Figure 41: XRD results, raw data for reduced pellets, 600°C with 25% humidity.

F – 0% H₂O 800°C

2023-04-24-BR-R-100H2-800C (Coupled TwoTheta/Theta)

Legend:
PDF 04-014-0164 Fe Iron
PDF 04-014-6635 Ca2Fe1.337Al0.663O5 Srebrodolskite, Al+3-bearing, syn
PDF 04-006-1869 Ca2Al2SiO7 Calcium Aluminum Silicate Oxide
PDF 04-006-9266 CaTiO3 Perovskite, syn
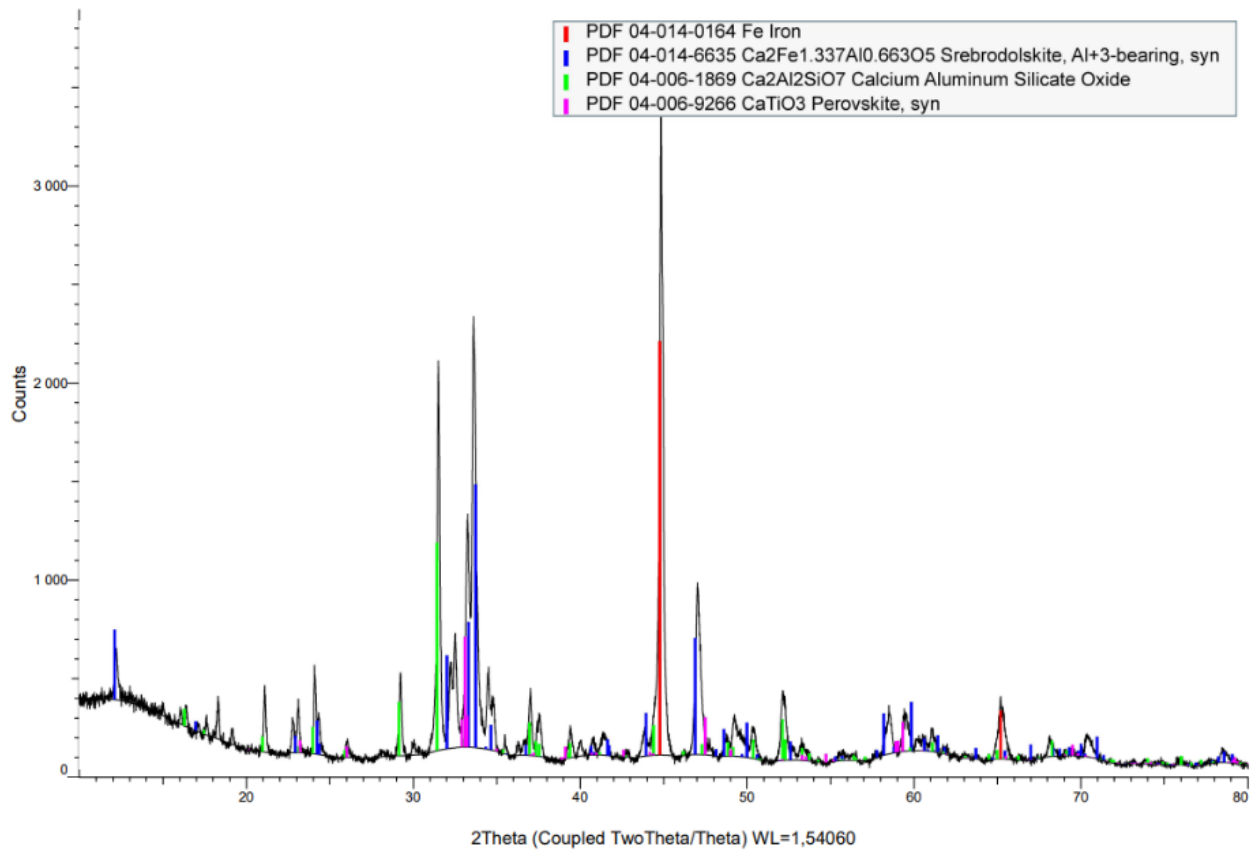
Appendix Figure 42: XRD results, raw data for reduced pellets, 800°C with 0% humidity.
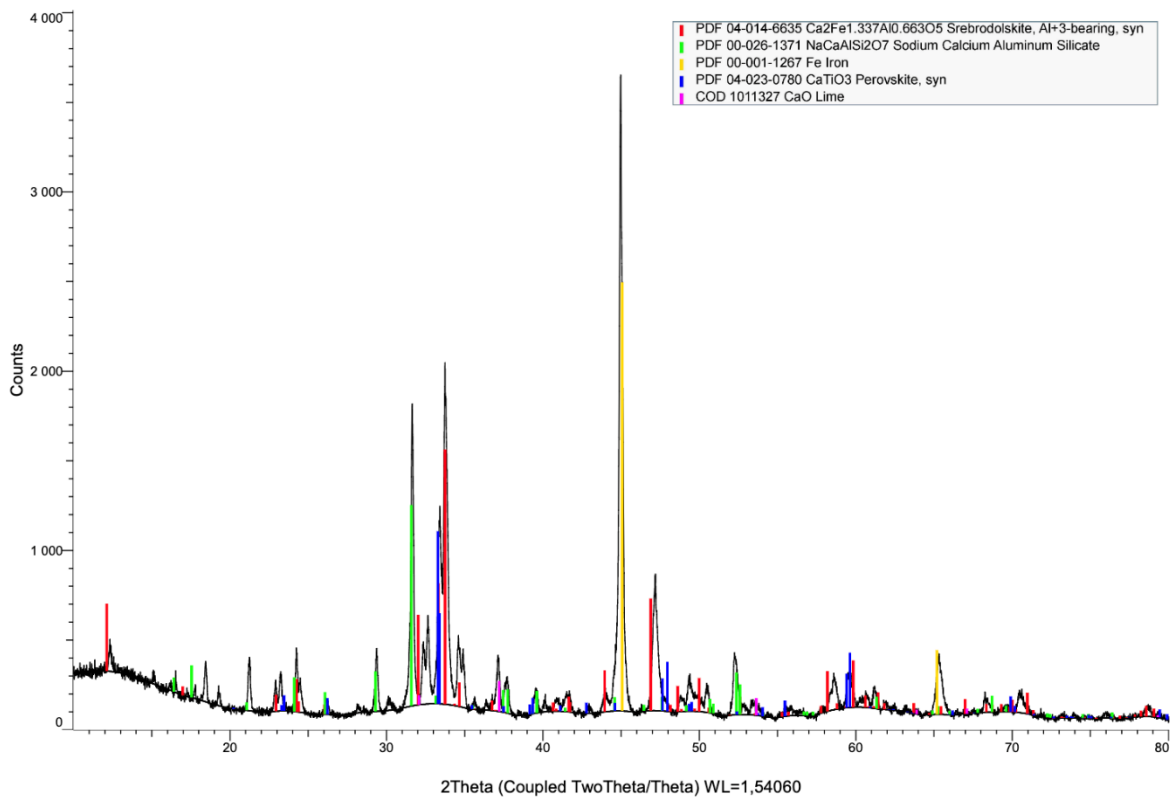
G – 5% H₂O 800°C

Appendix Figure 43: XRD results, raw data for reduced pellets, 800°C with 5% humidity.

H – 15% H₂O 800°C

Appendix Figure 44: XRD results, raw data for reduced pellets, 800°C with 15% humidity.

I – 25% H₂O 800°C

Appendix Figure 45: XRD results, raw data for reduced pellets, 800°C with 25% humidity.

VI - BET and BJH, raw data

The following section shows all the raw data obtained from BET and BJH analysis.

A – Sintered

Sample: BR Sintered
Operator:
Submitter: Sivert & Elias
File: C:\data\Sivert & Elias\BR Sintered.smp

Started: 3/22/2023 10:33:19 AM
Completed: 3/22/2023 1:20:48 PM
Report time: 3/23/2023 10:09:05 AM
Sample mass: 1,4357 g
Analysis free space: 57,0015 cm³
Low pressure dose: None
Automatic degas: Yes

Analysis adsorptive: N2
Analysis bath temp.: -195,935 °C
Thermal correction: Yes
Ambient free space: 16,0508 cm³ Measured
Equilibration interval: 5 s
Sample density: 1,000 g/cm³

Sample prep: Stage	Temperature (°C)	Ramp Rate (°C/min)	Time (min)
1	30	10	10

Summary Report

Surface Area

Single point surface area at $p/p° = 0,300162774$: 0,1309 m²/g

BET Surface Area: 0,1352 m²/g

Pore Size

Adsorption average pore diameter (4V/A by BET): 21,036 Å

Appendix Figure 46: BET and BJH, raw data for sintered pellets.

B – 0% H₂O 600°C

Sample: BET & BJH
Operator:
Submitter:
File: C:\data\Sivert & Elias\BR-R-100H2-600C.SMP

Started: 4/26/2023 9:49:26 AM
Completed: 4/26/2023 4:32:21 PM
Report time: 4/27/2023 1:04:21 PM
Sample mass: 2,7023 g
Analysis free space: 55,8596 cm³
Low pressure dose: None
Automatic degas: Yes

Analysis adsorptive: N2
Analysis bath temp.: -195,837 °C
Thermal correction: Yes
Ambient free space: 16,1367 cm³ Measured
Equilibration interval: 5 s
Sample density: 1,000 g/cm³

Sample prep: Stage	Temperature (°C)	Ramp Rate (°C/min)	Time (min)
1	30	10	10
2	90	10	60
3	250	10	780
4	25	10	60

Summary Report

Surface Area
Single point surface area at p/p° = 0,299741436: 1,2743 m²/g

BET Surface Area: 1,2931 m²/g

Pore Volume
Single point desorption total pore volume of pores
less than 1 768,992 Å diameter at p/p° = 0,989049463: 0,007934 cm³/g

Pore Size
Adsorption average pore diameter (4V/A by BET): 245,420 Å

Desorption average pore diameter (4V/A by BET): 245,420 Å

Appendix Figure 47: BET and BJH, raw data for reduced pellets, 600°C with 0% humidity.

C – 5% H₂O 600°C

Sample: BET & BJH
Operator:
Submitter:
File: C:\data\Sivert & Elias\BR-R-5H2O-600C.SMP

Started: 4/13/2023 1:38:15 PM
Completed: 4/13/2023 8:07:27 PM
Report time: 4/14/2023 11:39:54 AM
Sample mass: 2,6167 g
Analysis free space: 55,0705 cm³
Low pressure dose: None
Automatic degas: Yes

Analysis adsorptive: N2
Analysis bath temp.: -195,774 °C
Thermal correction: Yes
Ambient free space: 15,6079 cm³ Measured
Equilibration interval: 5 s
Sample density: 1,000 g/cm³

Sample prep: Stage	Temperature (°C)	Ramp Rate (°C/min)	Time (min)
1	30	10	10
2	90	10	60
3	250	10	780
4	25	10	60

Summary Report

Surface Area

Single point surface area at p/p° = 0,299348507: 0,4767 m²/g

BET Surface Area: 0,4856 m²/g

Pore Volume

Single point desorption total pore volume of pores
less than 1 934,646 Å diameter at p/p° = 0,990000000: 0,002865 cm³/g

Pore Size

Adsorption average pore diameter (4V/A by BET): 211,207 Å

Desorption average pore diameter (4V/A by BET): 236,006 Å

Appendix Figure 48: BET and BJH, raw data for reduced pellets, 600°C with 5% humidity.

D – 15% H₂O 600°C

Sample: BET & BJH
Operator:
Submitter:
File: C:\data\Sivert & Elias\BR-R-15H2O-600C-BRUK.SMP

Started: 4/25/2023 12:53:35 PM
Completed: 4/25/2023 7:08:48 PM
Report time: 4/26/2023 9:21:44 AM
Sample mass: 3,0018 g
Analysis free space: 55,2471 cm³
Low pressure dose: None
Automatic degas: Yes

Analysis adsorptive: N2
Analysis bath temp.: -195,826 °C
Thermal correction: Yes
Ambient free space: 15,6214 cm³ Measured
Equilibration interval: 5 s
Sample density: 1,000 g/cm³

Sample prep: Stage	Temperature (°C)	Ramp Rate (°C/min)	Time (min)
1	30	10	10

Summary Report

Surface Area
Single point surface area at p/p° = 0,299791562: 0,2577 m²/g

BET Surface Area: 0,2699 m²/g

Pore Volume
Single point desorption total pore volume of pores
less than 1 934,646 Å diameter at p/p° = 0,990000000: 0,001145 cm³/g

Pore Size
Adsorption average pore diameter (4V/A by BET): 163,506 Å

Desorption average pore diameter (4V/A by BET): 169,746 Å

Appendix Figure 49: BET and BJH, raw data for reduced pellets, 600°C with 15% humidity.

E – 25% H₂O 600°C

Sample: BET & BJH
Operator:
Submitter:
File: C:\data\Sivert & Elias\BR-R-25H2O-600C.SMP

Started: 4/13/2023 1:38:15 PM
Completed: 4/13/2023 8:07:27 PM
Report time: 4/14/2023 11:41:32 AM
Sample mass: 2,4494 g
Analysis free space: 55,7676 cm³
Low pressure dose: None
Automatic degas: Yes

Analysis adsorptive: N2
Analysis bath temp.: -195,774 °C
Thermal correction: Yes
Ambient free space: 15,7818 cm³ Measured
Equilibration interval: 5 s
Sample density: 1,000 g/cm³

Sample prep: Stage	Temperature (°C)	Ramp Rate (°C/min)	Time (min)
1	30	10	10
2	90	10	60
3	250	10	780
4	25	10	60

Summary Report

Surface Area
Single point surface area at p/p° = 0,299889715: 0,3052 m²/g

BET Surface Area: 0,3127 m²/g

Pore Volume
Single point desorption total pore volume of pores
less than 1 934,646 Å diameter at p/p° = 0,990000000: 0,001206 cm³/g

Pore Size
Adsorption average pore diameter (4V/A by BET): 145,866 Å

Desorption average pore diameter (4V/A by BET): 154,256 Å

Appendix Figure 50: BET and BJH, raw data for reduced pellets, 600°C with 25% humidity.

F – 0% H₂O 800°C

Sample: BET & BJH
Operator:
Submitter:
File: C:\data\Sivert & Elias\BR-R-100H2-800C-PORT1.SMP

Started: 5/3/2023 9:40:54 AM
Completed: 5/3/2023 2:45:11 PM
Report time: 5/4/2023 9:02:59 AM
Sample mass: 2,8305 g
Analysis free space: 55,3375 cm³
Low pressure dose: None
Automatic degas: Yes

Analysis adsorptive: N2
Analysis bath temp.: -195,603 °C
Thermal correction: Yes
Ambient free space: 15,7006 cm³ Measured
Equilibration interval: 5 s
Sample density: 1,000 g/cm³

Sample prep: Stage	Temperature (°C)	Ramp Rate (°C/min)	Time (min)
1	30	10	10
2	90	10	60
3	250	10	780
4	25	10	60

Summary Report

Surface Area
Single point surface area at p/p° = 0,300724009: 0,5287 m²/g

BET Surface Area: 0,5362 m²/g

Pore Volume
Single point desorption total pore volume of pores
less than 1 934,646 Å diameter at p/p° = 0,990000000: 0,001294 cm³/g

Pore Size
Adsorption average pore diameter (4V/A by BET): 96,180 Å

Desorption average pore diameter (4V/A by BET): 96,553 Å

Appendix Figure 51: BET and BJH, raw data for reduced pellets, 800°C with 0% humidity.

G – 5% H$_2$O 800°C

Sample: BET & BJH
Operator:
Submitter:
File: C:\data\Sivert & Elias\BR-R-5H2O-800C.SMP

Started: 4/25/2023 12:53:35 PM
Completed: 4/25/2023 7:08:48 PM
Report time: 4/26/2023 9:19:57 AM
Sample mass: 2,6450 g
Analysis free space: 56,1057 cm³
Low pressure dose: None
Automatic degas: Yes

Analysis adsorptive: N2
Analysis bath temp.: -195,826 °C
Thermal correction: Yes
Ambient free space: 15,8248 cm³ Measured
Equilibration interval: 5 s
Sample density: 1,000 g/cm³

Sample prep: Stage	Temperature (°C)	Ramp Rate (°C/min)	Time (min)
1	30	10	10

Summary Report

Surface Area

Single point surface area at p/p° = 0,300072415: 0,6575 m²/g

BET Surface Area: 0,6666 m²/g

Pore Volume

Single point desorption total pore volume of pores
less than 1 934,646 Å diameter at p/p° = 0,990000000: 0,001794 cm³/g

Pore Size

Adsorption average pore diameter (4V/A by BET): 103,878 Å

Desorption average pore diameter (4V/A by BET): 107,639 Å

Appendix Figure 52: BET and BJH, raw data for reduced pellets, 800°C with 5% humidity.

H – 15% H$_2$O 800°C

Sample: BET & BJH
Operator:
Submitter:
File: C:\data\Sivert & Elias\BR-R-15H2O-800C.SMP

Started: 4/25/2023 12:53:35 PM
Completed: 4/25/2023 7:08:48 PM
Report time: 4/26/2023 9:21:04 AM
Sample mass: 3,0318 g
Analysis free space: 55,4961 cm³
Low pressure dose: None
Automatic degas: Yes

Analysis adsorptive: N2
Analysis bath temp.: -195,826 °C
Thermal correction: Yes
Ambient free space: 16,0022 cm³ Measured
Equilibration interval: 5 s
Sample density: 1,000 g/cm³

Sample prep: Stage	Temperature (°C)	Ramp Rate (°C/min)	Time (min)
1	30	10	10

Summary Report

Surface Area
Single point surface area at p/p° = 0,299594741: 0,5157 m²/g

BET Surface Area: 0,5232 m²/g

Pore Volume
Single point desorption total pore volume of pores
less than 1 877,413 Å diameter at p/p° = 0,989690804: 0,001152 cm³/g

Pore Size
Adsorption average pore diameter (4V/A by BET): 88,065 Å

Desorption average pore diameter (4V/A by BET): 88,065 Å

Appendix Figure 53: BET and BJH, raw data for reduced pellets, 800°C with 15% humidity.

I – 25% H₂O 800°C

Sample: BET & BJH
Operator:
Submitter:
File: C:\data\Sivert & Elias\BR-R-25H2O-800C.SMP

Started: 4/26/2023 9:49:26 AM
Completed: 4/26/2023 4:32:21 PM
Report time: 4/27/2023 1:02:59 PM
Sample mass: 2,8332 g
Analysis free space: 55,1166 cm³
Low pressure dose: None
Automatic degas: Yes

Analysis adsorptive: N2
Analysis bath temp.: -195,836 °C
Thermal correction: Yes
Ambient free space: 15,6409 cm³ Measured
Equilibration interval: 5 s
Sample density: 1,000 g/cm³

Sample prep: Stage	Temperature (°C)	Ramp Rate (°C/min)	Time (min)
1	30	10	10

Summary Report

Surface Area

Single point surface area at p/p° = 0,299863868: 0,2277 m²/g

BET Surface Area: 0,2343 m²/g

Pore Volume

Single point desorption total pore volume of pores
less than 1 934,646 Å diameter at p/p° = 0,990000000: 0,000551 cm³/g

Pore Size

Adsorption average pore diameter (4V/A by BET): 93,363 Å

Desorption average pore diameter (4V/A by BET): 94,023 Å

Appendix Figure 54: BET and BJH, raw data for reduced pellets, 800°C with 25% humidity.

VII - Old SEM photos – sintered sample

In the start of the experimental work, an alternative SEM machine prior to the one used later was utilised. However, these results were deemed undesirable, as the machine struggled to get good photos at higher magnifications. This section shows all the photos and raw data for the sintered sample obtained from this SEM machine. Only the sintered sample was analysed using this machine.

A – Sintered pellets at SEI: 20x and BSE: 20x, 200x, 500x
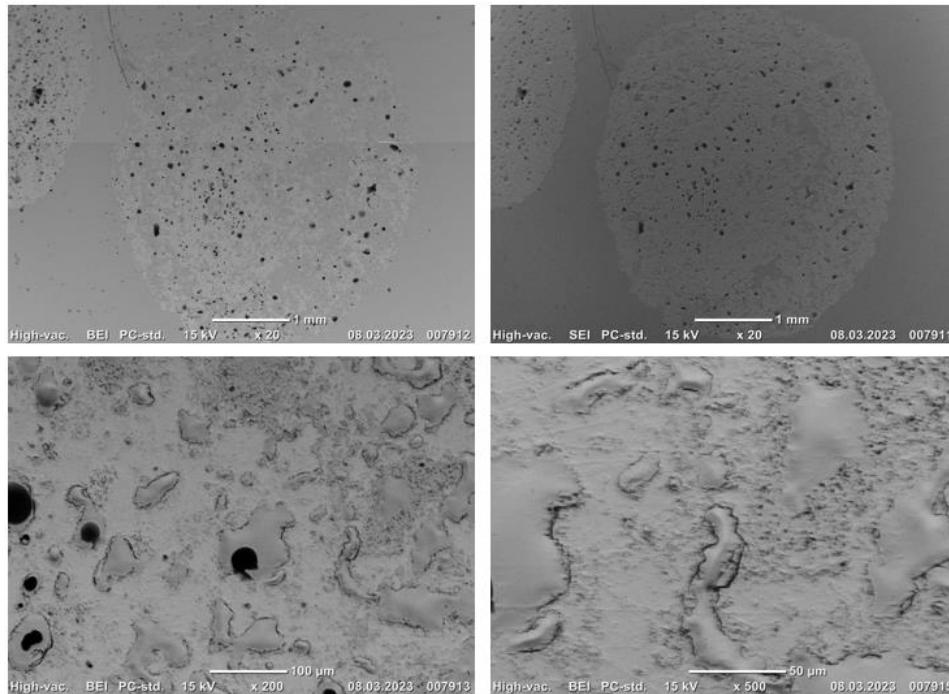
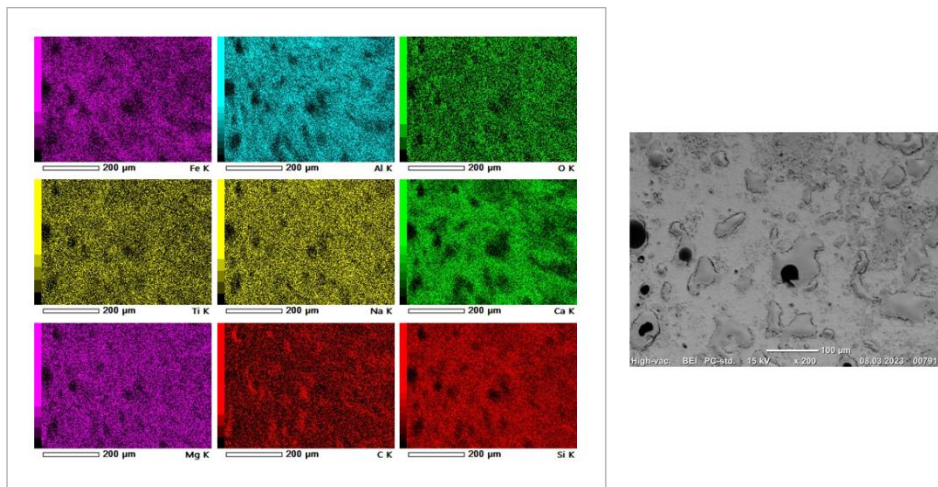**Appendix Figure 55:** SEM images of sintered pellets at 20x with SEI and 20x, 200x and 500x with BSE.

B – Point analysis for sintered pellet at 200x
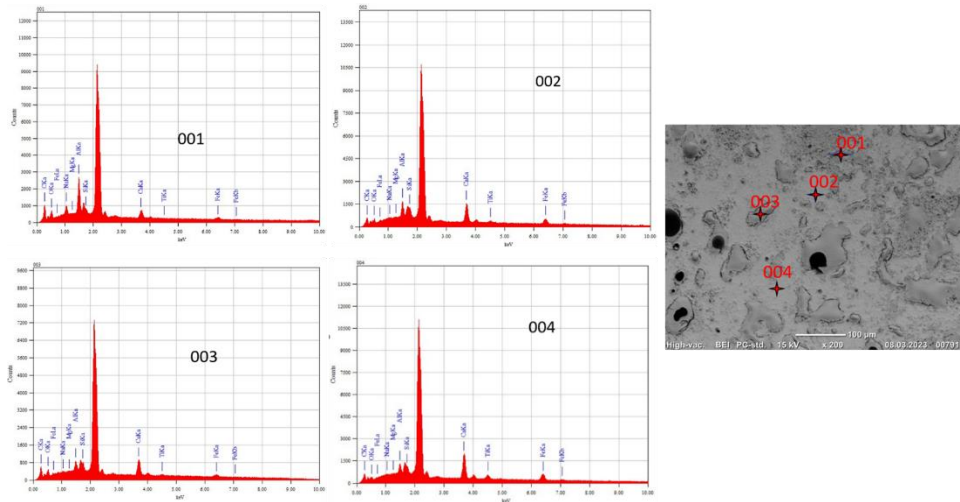
Appendix Figure 56: Point analysis for sintered pellets at 200x.

C – X-Ray mapping for sintered pellet at 200x

Appendix Figure 57: X-Ray mapping for sintered pellets at 200x.

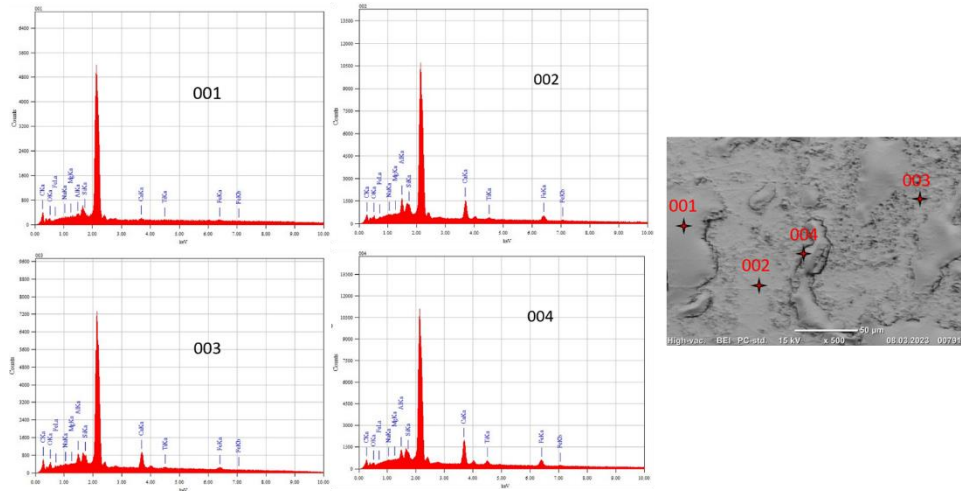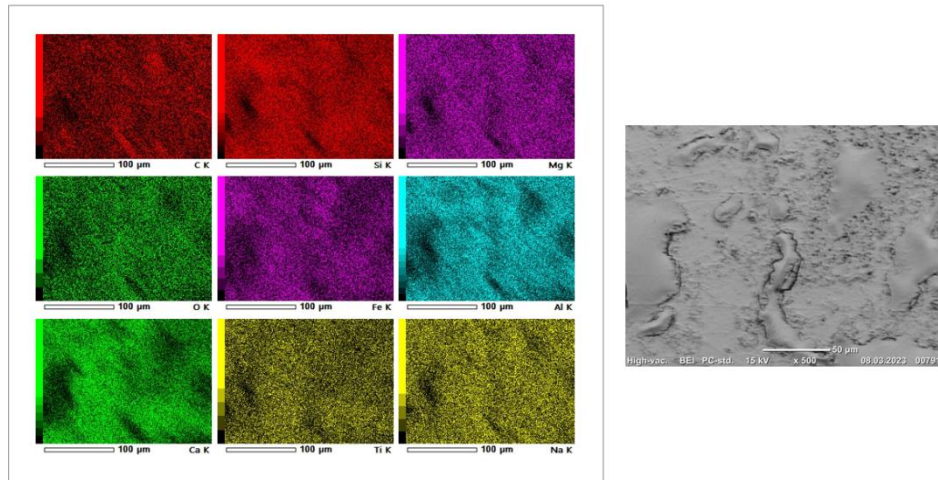## D – Point analysis for sintered pellet at 500x

Appendix Figure 58: Point analysis for sintered pellets at 500x.

E – X-Ray mapping for sintered pellet at 500x

Appendix Figure 59: X-Ray mapping of sintered pellets at 500x.

VIII - HSE data

A – H/P for EPOFIX Resin

	Warning
Contains:	Reaction product: bisphenol-A-(epichlorhydrin), epoxy resin (number average molecular weight <= 700) Oxirane, mono[(C12-14-alkyloxy)methyl] derivs.
H315	Causes skin irritation.
H317	May cause an allergic skin reaction.
H319	Causes serious eye irritation.
H411	Toxic to aquatic life with long lasting effects.
P273	Avoid release to the environment.
P280	Wear protective clothing, gloves, eye and face protection.
P302 + P352	IF ON SKIN: Wash with plenty of soap and water.
P305 + P351 + P338	IF IN EYES: Rinse cautiously with water for several minutes. Remove contact lenses, if present and easy to do. Continue rinsing.
P333 + P313	If skin irritation or rash occurs: Get medical advice/attention.
P337 + P313	If eye irritation persists: Get medical advice/attention.
Other hazards	
PBT/vPvB:	Not Classified as PBT/vPvB by current EU criteria.

Appendix Figure 60: H/P for EPOFIX Resin.

B – H/P for EPOFIX Hardener

	Danger
H302 + H312	Harmful if swallowed or in contact with skin.
H314	Causes severe skin burns and eye damage.
H317	May cause an allergic skin reaction.
P280	Wear protective gloves/protective clothing/eye protection/face protection
P301 + P330 + P331	IF SWALLOWED: Rinse mouth. Do NOT induce vomiting.
P303 + P361 + P353	IF ON SKIN (or hair): Take off immediately all contaminated clothing. Rinse skin with water [or shower].
P305 + P351 + P338	IF IN EYES: Rinse cautiously with water for several minutes. Remove contact lenses, if present and easy to do. Continue rinsing.
P310	Immediately call a POISON CENTER/doctor.
P501	Dispose of contents/container in accordance with local regulations.
P103	Read label before use.
P260	Do not breathe dust/fume/gas/mist/vapours/spray.
P270	Do not eat, drink or smoke when using this product.
P273	Avoid release to the environment.
P304 + P340	IF INHALED: Remove person to fresh air and keep comfortable for breathing.
P405	Store locked up.

Other hazards

Vapors are corrosive. After 24-36 hours, injured persons may develop serious shortness of breath and lung edema.

PBT/vPvB: No information available.

Appendix Figure 61: H/P for EPOFIX Hardener.

C – H/P for Hydrogen gas, H$_2$

Hazard pictograms (GHS-US) :

GHS02   GHS04

Signal word (GHS-US) : DANGER

Hazard statements (GHS-US) : H220 - EXTREMELY FLAMMABLE GAS
H280 - CONTAINS GAS UNDER PRESSURE; MAY EXPLODE IF HEATED
OSHA-H01 - MAY DISPLACE OXYGEN AND CAUSE RAPID SUFFOCATION.
CGA-HG04 - MAY FORM EXPLOSIVE MIXTURES WITH AIR
CGA-HG08 - BURNS WITH INVISIBLE FLAME.

Precautionary statements (GHS-US) : P202 - Do not handle until all safety precautions have been read and understood
P210 - Keep away from Heat, Open flames, Sparks, Hot surfaces. - No smoking
P271+P403 - Use and store only outdoors or in a well-ventilated place.
P377 - Leaking gas fire: Do not extinguish, unless leak can be stopped safely
P381 - Eliminate all ignition sources if safe to do so
CGA-PG05 - Use a back flow preventive device in the piping.
CGA-PG10 - Use only with equipment rated for cylinder pressure.
CGA-PG12 - Do not open valve until connected to equipment prepared for use.
CGA-PG06 - Close valve after each use and when empty.
CGA-PG02 - Protect from sunlight when ambient temperature exceeds 52°C (125°F).

Appendix Figure 62: H/P for Hydrogen gas, H$_2$.